CHARACTERIZATION OF MECHANICAL PROPERTIES OF CARBON NANOTUBE TURFS

By

ALI AHMAD ZBIB

A thesis submitted in the partial fulfillment of
the requirements for the degree of

MASTER OF SCIENCE IN MECHANICAL ENGINEERING

WASHINGTON STATE UNIVERSITY
Department of Mechanical and Materials Engineering

DECEMBER 2007

To the faculty of Washington State University:

The members of the Committee appointed to examine the thesis of ALI AHMAD ZBIB find it satisfactory and recommend that it be accepted.

_____

Chair

_____

_____

ACKNOWLEDGMENTS

I would like to acknowledge the help I received from several faculty members and colleagues in the school of mechanical and materials engineering at Washington State University. In particular, I would like to thank my committee members for their time and feedback Dr. Robert Richards, Dr. David Field and Dr. Sinisa Mesarovic. I would also like to acknowledge the NIRT group faculty members Dr. Cecilia Richards and Dr. Mohammad Osman for their suggestions during group meetings. I thank Devon McClain and Dr. Jun Jiao for the time they spent in growing my Carbon nanotube samples. I also appreciate all the help and support from my officemates and several other students in the school of mechanical and materials engineering. I also appreciate the help we received from Dr. Erica Lilleodden in Germany, who conducted a flat punch compression test on one of our turf using their Triboscope indenter.

I would also like to take this opportunity to particularly thank Dr. Sinisa Mesarovic, for all his time, consultation, suggestions and inputs in the process of this work, but also for his valuable teaching in several classes I took with him as an undergraduate and graduate student.

Finally, I would like to appreciate all of my advisor's work, dedication, support and constructive advice at my graduate and undergraduate level. He has welcomed me into his research laboratories since my freshman year, allowed me to develop my research skills, gave me the opportunity to write my first paper during my junior year, and encouraged me to present my research work as an undergraduate at the TMS conference. He has been more than an advisor to me, and has positively influenced me as a scientist and as an engineer. I thank him for everything he did for me.

CHARACTERIZATION OF MECHANICAL PROPERTIES OF CARBON NANOTUBE TURFS

ABSTRACT

by Ali Ahmad Zbib, M.S.
Washington State University
December 2007

Chair: David F. Bahr

CNT turfs, whether vertically arrayed or randomly grown, have different properties than those of a single tube. Since their discovery in 1991, several researchers have attempted to measure the mechanical properties and behavior of a single carbon nanotube, it being a multi-walled carbon nanotube or a single-walled carbon nanotube. However, with the exception of a few special geometries, little has been done to characterize the mechanical properties of an assemblage of CNTs, and their mechanical behavior under applied loading. Their characteristic properties arise from their complex nano-geometry, and the van der Waals driven interactions between individual CNT segments. This work is therefore dedicated to measuring the mechanical properties, and understanding the mechanical behavior of these intriguing nano-structures under applied loading and also to predicting the buckling mode and critical stress of the turf under compressive loading.

The general mechanical behavior of vertically aligned carbon nanotubes grown by chemical vapor deposition (CVD) was studied using nanoindentation techniques. Load-depth curves extracted from nanoindentation were used to calculate the elastic properties

of the turfs. Turfs exhibited non-linear elastic loading, with energy dissipation evident even with no permanent deformation. An average elastic modulus of CNT turfs was measured to be 14.9 MPa ± 5.8 MPa, and the hardness was on the order of 5.5 MPa. Permanent deformation occurred at an applied compressive stress of 2.53 MPa for these turfs, and was explained in terms of mechanical tube locking within the turfs, and was dependent on the CNT morphologies and density. Adhesive forces present between CNTs and the diamond tip affected the turf behavior under nanoindentation and increased the initial slope of the unloading segments, thus resulting in slightly higher elastic property measurements.

Carbon nanotubes turfs proved to exhibit coordinated and oriented buckling under applied compressive loading. A micromechanical model was developed describing the coordinated buckling phenomena of CNT turfs. Buckling stresses were found to be highly dependent upon the turf's shear modulus and height. To verify the results predicted by the model, several turfs with heights varying between 25 and 204 μm were buckled under applied compressive loading, and critical compressive values ranging between 4.3 and 0.2 MPa were measured respectively.

The intriguing results developed within this thesis are expected to affect the design of several applications that would use CNT turfs, such as thermal switches and composite materials.

TABLE OF CONTENTS

LIST OF TABLES

LIST OF FIGURES

DEDICATION

To my closest aunt and Uncle, Marcia and Hussein Zbib,
To my dear siblings Dima, Hamzeh and Leila,

To those who dedicated their lives to provide me with a life and an education,
My mom and dad, Fadia and Ahmad Zbib,

I dedicate this work.

CHAPTER ONE

1 INTRODUCTION: CARBON NANOTUBES EXTRAORDINARY PROPERTIES AND INTERESTING POTENTIAL APPLICATIONS

Since their discovery by Ijiima in 1991[1], and the unfolding of their extraordinary mechanical[2], thermal[3] and electrical[4] properties, carbon nanotubes (CNT) have inspired numerous potential applications in the fields of space, micro electrical and mechanical systems (MEMS), sensors, hydrogen storage and composite reinforcements. Their remarkable stiffness and mechanical strength, exceeding those of steel by an order of magnitude, has made carbon nanotubes one of the strongest structures ever tested. Coupling their exceptional strength along with their light weight, entitles them to have future applications in composite structures and materials[5].

As a result of CNTs' exceptional thermal properties, such as the high thermal conductivity (measured to be 6600 W/m K from end to end for a single tube)[6], there is interest in using a bundle of CNTs as a thermal switch in MEMS applications. CNT bundles or turfs are a group intertwined, entangled and pre-bent/pre-buckled carbon nanotubes, grown by chemical vapor deposition (CVD). They have shown promising results for use as a thermal switch, although a lower thermal conductivity has been measured for a CNT turf when compared to a single tube. However, despite their thermal properties and promising applications, they have mechanical implications resulting from the fact that CNT turfs have permanently buckled under applied compressive loads similar to those used in MEMS applications. Also. the strong adhesive properties of

CNTs to carbon based materials may also reduce the life of a thermal switch in application.

The exceptional strength of CNTs have inspired numerous extraordinary applications including one of the earliest proposed applications of CNTs, long ropes that are strong enough to hold an elevator extending from earth to space[7]. Their adhesive properties have also inspired researchers to create strong adhesives similar to those of gecko foot-hairs[8]. Both of these applications would require CNTS to exist in a bundle or turf structure.

All the previous observations, characteristics, properties and limitations built the foundation that triggered the interest in investigating the mechanical properties of a CNT turf as opposed to a single CNT. Several groups have attempted to measure the mechanical properties of single multi-walled carbon nanotubes (MWCNT) or single-walled carbon nanotubes (SWCNT). CNT turfs, and particularly those formed of entangled CNTs, have shown to behave differently than a single tube on both the mechanical and thermal level. However, except for a few special geometries, little theoretical and experimental work has been done to unfold their mechanical properties due to the expensive computational cost of modeling a CNT turf, and the high number of variables that need to be controlled in experimental work.

This thesis will assess the mechanical properties of a CNT turf consisting of entangled, pre-bent/pre-buckled tubes and grown by CVD. It will particularly focus on the elastic and plastic properties of these turfs, their behavior under applied compressive loading and their self oriented and coordinated buckling phenomena as well as their adhesive properties.

An overview of the work that has already been conducted to measure the mechanical properties of single MWCNT and SWCNT as well as CNT turfs will be discussed first. Detailed explanation of the methods and equipments used to conduct the required experiments within this thesis will be presented along with interesting observations and necessary calculations. The mechanical behavior of CNT turfs under nanoindentation, their adhesive properties and the effect of van der Waals bonding between neighboring tubes on the general mechanical behavior of the turf will then be discussed. Results of buckling CNT turfs, detailing their self oriented and coordinated buckling will be explained, along with the discussion of a new model developed to predict the critical buckling stress of these turfs knowing their geometry and elastic properties. Finally, the effect of this work on the progress of CNT applications will be discussed along with recommendations for future work.

References

[1] Iijima, S. Helical microtubules of graphitic carbon. *Nature* **354,** 56-58 (1991).
[2] Treacy, M. M. J., Ebbesen, T. W. & Gibson, J. M. Exceptionally high Young.s modulus observed for individual carbon nanotubes. *Nature* **381,** 678-680 (1996).
[3] Berber, S., Kwon, Y. amd Tomanek D. Unuasually high thermal conductivity of carbon nanotubes. *Phys. Rev. Lett.* **84 No.20**, 4613-4616 (2000).
[4] Baughman, R. H., Cui, Ch., Zakhidov, A., Iqbal, Z., Barisci, J., Spinks, G., Wallace, G., Mazzoldi, A., De Rossi, D., Rinzler, A., Jaschinski, O., Roth, S. & Kertesz, M. Carbon nanotube actuators. *Science* **284,** 1340-1344 (1999).
[5] Suhr, J., Koratkar, N., Keblinski, P. & Ajayan, P. Viscoelasticity in carbon nanotube composites. *Nature* **4,** 134-137 (2005).
[6] Berber, S., Kwon, Y. K. & Tomanek D. Unusually high thermal conductivity of carbon nanotubes. *Phys. Rev. Lett*. **84 (20),** 4613-4616 (2000).
[7] Dresselhaus, M. S. Nanotubes a step in synthesis. Nature 3, 665-666 (2004).
[8] Yurdumakan, B., Raravikar, N., Ajayan, P. & Dhinojwala, A. Synthetic gecko foot-hairs from multiwalled carbon nanotubes.

CHAPTER TWO

2 LITERATURE REVIEW

2.1 Carbon Nanotubes: a unique nanostructure

Carbon nanotubes (CNTs) are unique nanostructures, consisting of carbon atoms bonded in sp2, to form graphitic sheets that are rolled in a tubular shape, thus forming a carbon nanotube wall. sp2 bonding consists of three σ bonds that bond to neighboring carbon atoms to form graphite in plane sheets with a π out of plane bond. However for graphite sheets to exist as rolled structures, the three σ bonds are organized such that carbon atoms bond to form a curved wall. A defect free carbon nanotube is defined as a tube for which carbon atoms are bonded in hexagonal networks across the wall. A defected CNT would have a pentagonal or heptagonal network across the wall. The hybrid bonding described above is what gives CNTs unique mechanical, electrical and thermal properties[1].

Multi-walled carbon nanotubes (MWCNT) were first observed by Ijiima at NEC corporation laboratory, Japan in 1991[2]. He produced MWCNTs using an arc-discharge evaporation method, with diameters ranging from a few nanometers, to a few tens of nanometers. A few years later, in 1993, single-walled carbon nanotubes were discovered simultaneously by Ijiima et al. in Japan[3] and Bethune et al at the IBM research division in CA, USA[4].

Several types of carbon nanotubes may exist depending on the chirality of the tubes, defined by a vector **C**, a function of the graphitic lattice vectors $\mathbf{a_1}$ and $\mathbf{a_2}$ shown on figure 2.1 as follows:

$$\mathbf{C}=n_1\mathbf{a_1}+n_2\mathbf{a_2} \qquad (1)$$

where n_1 and n_2 are integers, and $n_1 > n_2$.

Two particular chiralities are shown and labeled on figure 2.1: zigzag (with coefficients $(n_1,0)$) and armchair (with coefficients (n_1,n_1)).

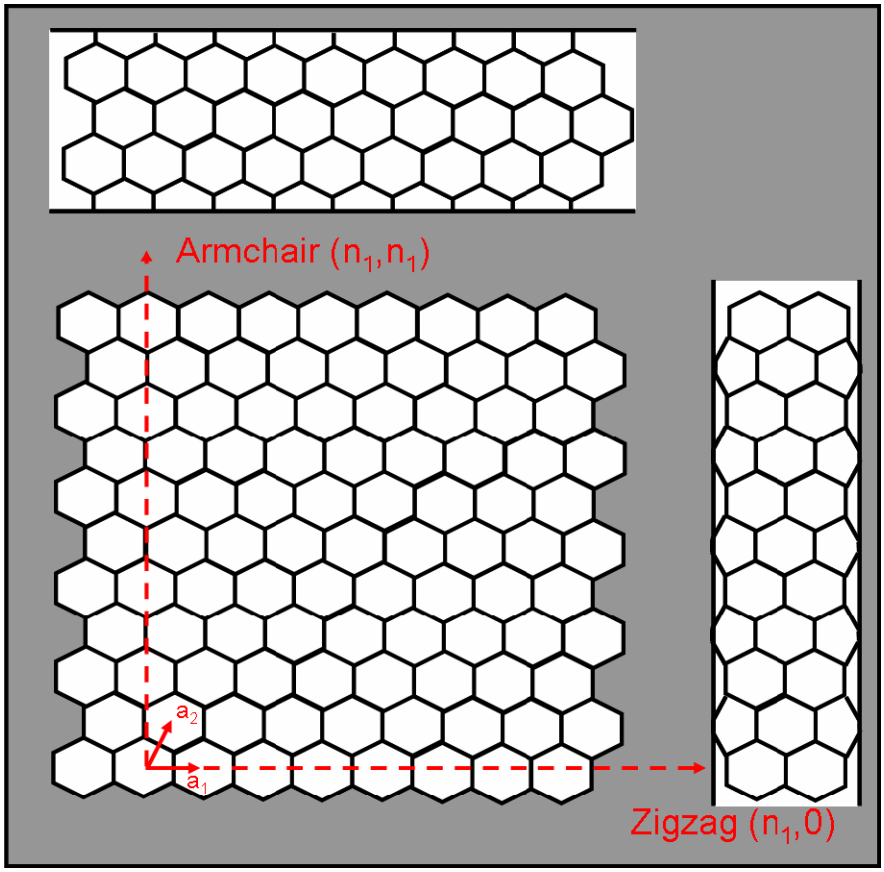

Figure 2.1 CNT chiralities

CNT properties, such as its heat transfer capacity and resistance to tensile loads have proven to be highly dependent upon chirality. However chirality have shown to have little effect on Young's modulus[5].

Carbon nanotubes may exist as MWCNT with several concentric walls bonded by van der Waals weak, short range bonds with diameters ranging from a few nanometers to a few tens of nanometers, or as SWCNT having a diameter of 1 to 1.2 nm. Cocentric

walls in a MWCNT are separated by a distance of 0.34 nm, the same distance that separates graphite sheets in bulk.

A CNT turf is a bundle of intertwined, pre-bent vertically aligned carbon nanotubes grown by chemical vapor deposition (CVD)[6]. Carbon nanotubes in the forest like turf being pre bent have a bending strain energy that is balanced by the contact energy between the tubes[7]. Neighboring carbon nanotubes are bonded by weak van der Waals bonds as well.

2.2 Growth Methods of Carbon Nanotubes

Since the first synthesis of carbon nanotubes, performed by Iijima at the NEC laboratory in Japan in 1991, and the discovery of their exceptional properties, several researchers have focused on developing new growth techniques that would allow mass production of carbon nanotubes, and the control over the growth variables and properties such as chirality, number of concentric walls within a single tube, tube diameter, length and structural defects. One of the first techniques used for CNT growth was the Arc-Discharge and Ablation method. It was used by Ijiima to grow the first tubes in 1991, and a breakthrough in the growth technique which led to mass production of CNTs (measured in grams) was made by Ebbesen and Ajayan in 1992[8]. In a growth vessel, filled with helium gas, a high voltage is passed through a carbon anode and cathode spaced a distance of 1 mm at all times, which evaporates carbon atoms and allows the formation of tubular shaped carbon structures, or carbon nanotubes. This technique can lead to the formation of both MWCNT and SWCNT, with few structural defects (pentagon and heptagon network formation)[9].

However, CNT turfs or forest like bundles, such as those tested within this thesis, were grown using chemical vapor deposition, a method that did undergo several enhancement in the past few years. Following the production of the first vertically aligned carbon nanotubes by Terrones et al. in 1997, a new technique which would allow mass production of VACNT was necessary. CVD was one of the techniques that was enhanced by several researchers[10-12].

CNT turfs grown for the purpose of the experiments conducted in this research were grown using the method described by Dong et al[13]. The silicon dies with the sol-gel pattern, were put in a furnace, which was evacuated down to 0.03 Torr. The catalyst embedded in the sol-gel solution was then calcinated at a temperature at 450ºC for 2 hours, and then activated at 500ºC in a hydrogen gas H_2 environment at 75 Torr. Carbon nanotube growth was then initiated at 700ºC by flowing a hydrocarbon gas mixture (in this case C_2H_2) mixed with H_2 into the chamber. Under high temperature, the hydrocarbon gas dissociated and carbon atoms were attracted by the iron particle catalysts, and bonded to each other with sp2 bonds in a tubular shape, thus producing carbon nanotubes. The furnace chamber was finally evacuated again down to 0.03 Torr, and allowed to slowly cool, before removing the resulting patterned vertically aligned carbon nanotube turfs. More details on the CVD technique are provided in chapter 3.

2.3 Testing Methods of Carbon Nanotubes

Several experimental procedures were developed to test the mechanical properties of single MWCNT and SWCNT as well as vertically aligned CNT turfs. Concurrently, several theoretical models were developed to predict the mechanical behavior of single tubes as well as a multitude of them in a bundle.

One of the traditional tests conducted to extract mechanical properties of materials is the standard tensile test. Yu et al. developed an apparatus to test MWCNTs in tension[14]. The apparatus consisted of two AFM (atomic force microscope) tips installed inside a scanning electron microscope (SEM). A MWCNT was attached onto the AFM tips which pulled it in tension, while monitoring the load and the respective displacement. Stress-strain curves were recorded, which allowed the measurement of Young's modulus of each tested MWCNT. The modulus of elasticity ranged from 270 to 950 GPa for 19 MWCNTs. The tension tests conducted on the tubes were recorded under the SEM, and it was observed that the outer wall of a MWCNT seemed to be the first one to fracture and that was due to the way the tubes were attached to the AFM tip. One intriguing observation was the fact that once the tube fractured, the total length of the two fractured sections of the tube was larger than that of the tube right before fracture occurred. This was explained in terms of a "sword-in-sheath " fracture mechanism, by which the outer wall breaks first, which causes the interlayer to slide along the outer layer prior to complete fracture, which results in two long segments as shown by the authors. Tensile stresses smaller than those measured ideally for SWCNT[15, 16] ranging between 11 to 63 GPa were measured. These values are bigger than the values measured for carbon fibers which have shown similar failure modes[17]. Recent simulations based on a continuum shell model have shown that the atomic structure of CNTs i.e. chirality of the tubes, highly affected its response to tensile loading. The armchair tubes reached a large stress-strain under applied tensile forces, than zigzag tubes, with a similar elastic modulus[18]. The fact that fracture begins at the outer layers, and then is followed by the fracture of the interlayers/walls of a single CNT under applied tensile loads, has been demonstrated

using molecular dynamics simulations[19]. Tensile strengths as high as 1.684 10^5 MPa were measured for a three walled CNT.

Another test used to understand the mechanical behavior of a CNT was the bending test. Kuzumaki et al. conducted bending experiments, and observed the behavior of a single tube in situ using a scanning electron microscope[20]. They showed that the tubes buckled sharply (peak bending angles of 85º and 135º were observed). They argued that bending of CNTs was the results of a state of bonding change from sp2 to sp3, which allowed such sharp bending angles. Their argument was further supported with an MD model, which energetically favored the bonding state change over the elastic deformation of the tube. Recent applications have required bending and shape change of CNTs, and thus a new technique using a focused beam of gallium ions was recently developed to control bending of single CNTs[21].

Treacy et al. developed one of the first techniques to measure the elastic modulus of a CNT by measuring their thermal vibrations. Using a TEM, the slope of the mean square vibration amplitude of a CNT was measured for several temperatures, and the value of its Young's modulus was measured to be 1.8 TPa on average as described by Treacy et al.

2.4 Elastic Properties of Carbon Nanotubes

The discovery of CNTs, was followed by the discovery of their intriguing mechanical properties, one of the most important being their high elastic modulus, which triggered several CNT applications. As noted before, Treacy et al. were the first to measure the elastic modulus of carbon nanotubes experimentally by measuring thermal vibration of several nanotubes and extracting their Young's modulus. They measured an

average value of 1.8 TPa. Several experimental techniques as well as theoretical models followed to estimate the elastic modulus of both SWCNT and MWCNT. Lourie et al. used Raman spectroscopy on SWCNT and measured a range of 2.8-3.6 TPa for elastic modulus. The elastic modulus of MWCNT was measured to be between 1.7 and 2.4 TPa, a range smaller than that of SWCNT as would be expected. Wong et al. used a cantilevered beam model and measured an elastic modulus of 1.28±0.59 TPa for MWCNT[22]. Salvetat et al. used a simply supported beam model to measure a Young's modulus close to 100 TPa for both MWCNT and SWCNT[23]. They applied a load using an AFM tip on a CNT that was simply supported and measured the respective deflection. On the lower end of measured elastic properties were Yu et al. who measured a range of 270-950 GPa for MWCNT and a range of 320-1470 GPa with a mean of 1002 GPa for SWCNT.

Several groups have attempted to estimate CNT's elastic modulus using molecular dynamic techniques as well as finite element modeling. Yakobson et al. used MD simulation and estimated the elastic modulus of SWCNT to be 5.5 TPa[24]. Also, similar techniques were used by Lu, who estimated a value of 1 TPa[25]. Yao et al. used a potential model a calculated a value of 1 TPa as well for SWCNT[26]. The electronic band theory was used by Zhou et al. who calculated a value of 5.1 TPa[27]. Table 2.1 summarizes several measurements of the elastic modulus of CNTs conducted by several research groups over the past 16 years, using several experimental and theoretical techniques[15-27].

Table 2.1 CNT Elastic Modulus Measurements

	CNT Type	Experiment Type	Research Group	Measured Elastic Modulus (GPa)
Experimental Measurements				
1	SWCNT	Thermal Vibration	Treacy, M. M. J., et al. Nature 1996	1800 GPa
2	SWCNT	Compressive response/Raman Spectroscopy	Lourie and Wagner. J. Mater. Res. (1998)	2800-3600 GPa
3	MWCNT	Compressive response/Raman Spectroscopy	Lourie and Wagner. J. Mater. Res. (1998)	1700-2400 GPa
4	MWCNT	Cantilivered Beam Model	Wong, E. W., et al. Sience (1997)	1280± 590 GPa
5	MWCNT	Simply Supported Beam Model	Salvetat, J. P., et al. Adv. Mater. (1999)	1000 Gpa
6	SWCNT	Simply Supported Beam Model	Salvetat, J. P., et al. Phys. Rev. Lett. (1999)	1000 GPa
7	MWCNT	Tensile test	Yu, M. et al. Science (2000)	270-950 GPa
8	SWCNT	Tensile test	Yu, M. et al. Science (2000)	320-1470 GPa (Mean 1002 Gpa)
Theoretical Predictions				
1	SWCNT	Empirical Keating Hamiltonian	Overney et al. Z. Phys. D. (1993)	1500-5000 GPa
2	SWCNT	Molecular Dynamics	Yakobson, B. I. et al. Phys. Rev. Lett. (1996)	5500 GPa
3	SWCNT	Molecular Dynamics	Lu, J. P., et al. Phys. Rev. Lett. (1997)	1000 GPa
4	SWCNT	Potential Model	Yao, N. et al. J. Appl. Phys. (1998)	1000 GPa
5	SWCNT	Potential energy derivation	Gao, G. H. et al. Nanotechnology (1998)	640.3-673.49 GPa
6	SWCNT	Electronic band Theory	Zhou, B., et al. Phys. Rev. B (2000)	5100 GPa

2.5 Plastic Properties of Carbon Nanotubes

Plastic properties of single SWCNT and MWCNT have shown to be highly dependent upon the chirality of the tubes. Under tensile loads, MD simulations have shown that a CNT may have brittle or ductile behavior. Nardelli *et al.* simulations' argued that CNT under low temperature and undergoing high tensile strain (1300 K and 15% strain) behave in a brittle fashion. However the high temperature case coupled with low strain (3000 K and 3% strain), proved to be chirality dependent: armchair CNTs deformed in a ductile fashion while zigzag CNTs behaved in a brittle fashion for large

tubes[30]. Hunag et al. showed that at high temperatures reaching 2000ºC, A SWCNT showed superplastic behavior: under tensile loading a 24 nm long SWCNT elongated by 280% prior to fracture, and its diameter reduced from 12 nm to 0.8 nm[31]. The plastic behavior of CNTs has been studied experimentally by Daraio et al. They dropped a ball on a turf of vertically aligned CNTs, and observed that they fragmented into uniform pieces of 100-150 nm. They proposed three possible reasons for fragmentation: buckling of the tubes under dynamic loads as a result of dropping the ball, sequential fragmentation, or fracturing of tubes at tube-tube contact points[32].

2.6 Buckling and Instabilities of Carbon Nanotubes

Before the buckling experiments of a CNT turf, which is extensively discussed in chapter 5, understanding buckling and the instability of a single tube under applied compressive loading is necessary. Yakobson et al. MD simulations, revealed that a CNT undergoes four singularity points in its strain energy vs. strain plots, characteristic of four different shapes a CNT undergoes while buckling under applied compressive loads. Yeak et al. used both MD simulations and multiscale techniques to show that a SWCNT undergoes several shape changes while buckling sideways[33]. Liew et al. showed that a SWCNT buckled at a critical load $0.8X10^{-7}$ N, corresponding to a critical strain of 0.28. One of the major differences between the mechanical behavior of a SWCNT and the MWCNT is the presence of van der Waals bonds between co-centric tubes of a given MWCNT. Thus it is necessary to understand whether the presence of these forces affect the critical buckling stress or strain for a single MWCNT, especially that these forces play a major role in the buckling of a CNT turf as will be discussed later. Ru developed a continuum mechanics model, in which he studied buckling of MWCNT in the presence

of van der Waals bonds. His results showed that van der Waals bonding between co-centric tubes did not increase the critical buckling strain of the whole MWCNT[34], but did increase the critical buckling load of a MWCNT[35]. On the other hand, Yakobson et al. showed that the presence of these weak bonds should not affect the critical buckling load. Experimental results obtained by Waters et al.[36,37] seemed to agree with Yakobson's conclusion rather than Ru's. Another kind of buckling has been studied by Jeng et al.[38] They conducted MD simulations of an indentation on a side of (10,10) SWCNT using an carbon AFM tip. Their work provides snap shot illustration of the deformation process as well as a load-displacement simulation of the indent. The simulation showed that the SWCNT deformed linearly prior to buckling and then the load dropped following the buckling of the tube. It was also noted that defects were introduced following buckling as four hexagonal networks merged into two pairs of pentagons and heptagons. The tube also adhered to the carbon based tip during pull-off.

2.7 Thermal and Electrical Properties of Carbon Nanotubes

Carbon nanotubes have shown to have intriguing thermal and electrical properties that triggered several potential applications in the fields of MEMS and micro-electronics. CNTs thermal conductivity has been measured experimentally and theoretically by several research groups, who agreed on the fact that CNT showed high thermal conductivity. Berber *et al.* used molecular dynamics techniques and estimated the thermal conductivity λ of a single nanotube to be 6600 W/mK[39]. Kim et al. measured a conductive thermal conductivity of 3000 K for a MWCNT[40]. Hone et al. showed that the thermal conductivity of SWCNT is temperature dependent. By measuring the thermal

conductivity of a bundle of SWCNT they proved that λ (conductive thermal conductivity) decreased smoothly with temperature decreasing from 350 K to 8 K[41].

2.8 Difference between a Single Tube and a Carbon Nanotube Turf: Effect of van der Waals bonding

Although the mechanical, thermal and electrical properties of a single CNT whether it's a MWCNT or a SWCNT have been studied extensively as discussed in the previous sections, little has been done to study these properties in case of CNT turfs or bundles. However the work conducted on CNT turfs have shown that these structures behaved differently than a single tube on the mechanical thermal and electrical levels. For example the thermal conductivity has been shown to drop to 200 W/mK due to tube-tube interactions and tube bending and physical contacts[42]. CNT turfs are complex structures of intertwined, nominally vertical tubes[6,43]. Their complexity arises mainly from the tube-tube interactions, and on the mechanical properties level due to the presence of van der Waals bonding. Van der Waals bonding, being short range and weak bonds, allow neighboring CNTs to slide with respect to each other, thus reducing the elastic modulus of a CNT turf when compared to single tube[44]. Kis et al. showed that the bending modulus of a CNT bundle was inversely proportional to the bundle diameter, which would be counter intuitive in any other case, but may be explained by the fact that that as the number of tube increase the sliding of tubes under mechanical load increased, which therefore reduced the strength of the bundle. They also showed that the shear modulus of a CNT is close to that of graphite due to tube sliding as well[45]. One solution to prevent the weakening effect of van der Waals bonding was to add strong covalent bonding using-electron beam irradiation between neighboring tubes within a bundle, which was

achieved by Kis et al. This avoided neighboring tubes from sliding along each other, a mechanism responsible for reducing the shear modulus of the turf.

However, the CNT turfs studied within this thesis are more complex than the bundles discussed previously: rather than being fully vertically aligned, they are intertwined, pre-bent and pre-buckled which explains why little work has been done on investigating their mechanical properties. Most of the work was conducted using nanoindentation techniques, and little work has been done theoretically[46] due to the expensive computational requirements.

2.9 Nanoindentation of Carbon Nanotube Turfs

Qi et al. conducted indentation tests on MWCNT samples grown by plasma enhanced chemical vapor deposition[47]. However these samples consisted of thick, well spaced and perfectly vertical MWCNT. These geometrical features highly affected the type of testing being conducted under nanoindentation since as the tip approached the sample, it deformed individual tubes independent of its neighboring tubes: as the triangular shaped tip penetrated the sample it caused MWCNTs to bend, and thus the load resistance was the result of individual tube bending. This meant that these tests actually tested the properties of single tubes rather the whole bundle as no tube slid or mechanically connected to its neighboring tubes. Qi et al. measured an effective axial modulus of a tube to be 0.9-1.23 TPa and an effective bending modulus to be 0.91-1.24 TPa.

McCarter et al. conducted nanoindentation experiments on CNT turfs grown by CVD with highly intertwined, pre-bent and pre-buckled CNTs. They showed that these

complicated nanostructures exhibited non-linear elasticity starting with a high initial tangent modulus and followed by significant drop in that modulus. They used Oliver and Pharr's[48] technique to calculate the tangent modulus of the turf at the peak of loading as well as its hardness using the initial unloading slope of the load-displacement curve and the contact area (this technique will be further discussed in chapter 3). Since nanoindents were conducted using a diamond Berkovich tip, the unloading portion of the indents revealed a negative load, characteristic of the adhesion between individual tubes and the tip.

2.10 Buckling of CNT turfs

As was mentioned earlier, little has been done to investigate the mechanical behavior of a CNT turf under applied compressive loading. The experimental and theoretical work that has been conducted, is limited by special geometries and boundary conditions. This avoids the computationally expensive techniques on one hand and allows a better control over the several variables that come into play while conducting an experiment. No scientific work has been conducted to examine the mechanical behavior of a CNT turf composed of intertwined, tangled and pre-bent/buckled CNT, which are the result of CVD growth, in contact with a sol-gel layer with iron particle catalysts.

Cao et al. studied the behavior of CNT films made of perfectly straight and vertically aligned CNT under several compression cycles that were released from a substrate[49]. Their results showed that these films had a much higher compressibility and much higher strength than any foam material. In most foam material one property would negatively affect the other (more compressibility is the result of an increase in voids within the foam, and thus decreases the compressive strength, and visa versa). The fact

that these two properties in CNT films were not inter-dependent is what makes them attractive for commercial applications. The researchers also showed that the stress-strain curve of the CNT film showed similar trends as foam materials: three stages with the first being a linear stress-strain relation with a high modulus (50 MPa), followed by a plateau characterizing the formation of the zig-zag reversible buckles (at 22 % strain) and a reduction in modulus to 12 MPa, followed by a densification stage. These films deformed in azigzag shape down to 15% of their original height and then unbuckled back close to their original heights. Finally and most importantly, the authors showed that if the buckling stress of the film is divided by the density of CNT within the film (13%), the resulting stress is similar to that that would predicted for the buckling of single tube using the Eulerian beam theory (a single tube buckled at a stress of 92 MPa, while the Eulerian beam theory predicted a buckling stress of 110 MPa).

Waters et al.[36, 37] grew perfectly uniform and equally spaced CNT turfs by depositing cobalt catalysts in uniformly space pores in an alumina matrix. This allowed for perfectly straight CNT growth, and allowed the authors to etch the alumina matrix to expose the desired length of MWCNT for testing. Instead of testing a single MWCNT which would require careful and expensive experimental setups, the author used a circular flat punch 2 μm in diameter to test approximately 363 nanotubes under uniform applied compressive stress using an MTS nanoindenter. Their results agreed with those predicted using elastic shell theory and calculated a critical buckling load of 2.26 and 2.54 for the 100 nm and 50 nm long tubes. These results seemed to agree with the results obtained by Yakobson et al. as mentioned earlier and thus agree with their result that van der Waals bonding between co-centric tubes did not seem to affect the critical buckling

load. Although conducted on a series of MWCNT equally spaced, these experiments studied the behavior of a single tube rather than that of a bundle under compressive loading.

2.11 CNT Applications as a single tube and as a turf

Due to the fact that CNT have shown high strength and elastic modulus exceeding those of steel by 1 order of magnitude, one of the most controversial future use of CNTs is to build the strongest known ropes, which will be used to build an elevator to space[50]. Their strong adhesive properties have also entitled them to be used as strong adhesive structures similar to gecko foot hairs[51]. Their packing and absorption properties are likely to open the doors for their use as hydrogen storage structures for future fuel cell powered vehicles[52]. Since they have narrow width, they were used as nanoprobes for scanning surfaces at a nanometer scale. Their flexibility and chemical properties allowed them to resist a tip-surface crash and withstand several scanning environments (vacuum, ambient air and liquids)[53]. They will be used in future electronics to produce highly connecting and slender electrical wiring. Their high strength to weight ratio, makes them a strong candidate for usage in future composites[54] for space missions. One of the most recent applications of CNT turfs is their as a thermal switch in MEMS applications, owing to their high thermal conductivity. An array of CNT turfs connected to cold source would approach the membrane of a hot MEMS device, allowing the heat to transfer from the hot MEMS to the cold source. The flexibility of the turfs and their resistance to fatigue cycling will allow for a design of a durable high frequency thermal switch.

2.12 References

[1] Meyyappan, M. *Carbon Nanotubes. Science and Applications*. CRC Press. 1-24 (2005).
[2] Iijima, S. Helical microtubules of graphitic carbon. *Nature* **354,** 56-58 (1991).
[3] Iijima, S., & Ichihashi, T. Single-shell carbon nanotubes of 1nm diameter. *Nature* **363,** 603-605 (1993).
[4] Bethune, D. S., Klang, C. H., De Vries, M. S., Gorman, G., Savoy, R., Vasquez, J. & Beyers, R. Cobalt-catalysed growth of carbon nanotubes with single-atomic-layer walls. *Nature* **363,** 605-607 (1993).
[5] Lu, J. P. Elastic properties of carbon nanotubes and nanopores. *Phys. Rev. Lett.* **79 (7),** 1297-1300 (1997).
[6] Terrones, M., Grobert, N., Olivares, J., Zhang J. P., Terrones, H., Kordatos, K., Hsu, W. K., Hare, J. P., Townsend, P. D., Prassides, K., Cheetham, A. K., Kroto, H. W. & Walton, D. R. M. Controlled production of aligned-nanotube bundles. *Nature* **388,** 52-55 (1997).
[7] Mesarovic, S. Dj., McCarter, C. M., Bahr, D. F., Radhakrishnan, H., Richards, R. F., Richards, C. D., McClain, D. & Jiao, J. Mechanical behavior of a carbon nanotube turf *Scripta Materialia* **56,** 157-160 (2007).
[8] Ebbesen, T. W. & Ajayan, P. M. Large-scale synthesis of carbon nanotubes. *Nature* **358,** 220-222 (1992).
[9] Dresselhaus, M. S., Dresselhaus, G. & Avouris Ph. Carbon Naotubes: Synthesis, Structure, Properties and Applications. *Springer*, 29-53 (2000).
[10] Jung, M., Eun, K.Y., Lee, J.K., Baik, Y.J., Lee, K.R. & Park, J.W. Growth of carbon nanotubes by chemical vapor deposition. *Diamond and Related Materials* **10,** 1235-124 (2001).
[11] Wei, Y. Y., Eres, G., Merkulov, V. I., & Lowndes, D. H. Effect of catalyst film thickness on carbon nanotube growth by selective area chemical vapor deposition. *App. Phys. Lett.* **78 (10),** 1394-1396 (2001).
[12] Merkulov, V. I., Melechko, A. V., Guillorn, M. A., Lowndes, D. H. & Simpson, M. L. Alignment mechanism of carbon nanofibers produced by plasma-enchanced chemical vapor deposition. *App. Phys. Lett.* **79 (18),** 2970-2972 (2001).
[13] Dong, L., Jiao, J., Pan, C. & Tuggle, D. W. Effects of catalysts on the internal structures of carbon nanotubes and corresponding electron field emission properties. *Appl. Phys. A* **78,** 9-14 (2004)
[14] Yu, M. F., Lourie, Dyer, M. J., Moloni, K., Kelly, T. F. & Ruoff, R. S. Strength and breaking mechanism of multiwalled carbon nanotubes under tensile loads. *Science* **287,** 637-640 (2000).
[15] Treacy, M. M. J., Ebbesen, T. W. & Gibson, J. M. Exceptionaly high Young's modulus observed for individual carbon nanotubes. *Nature* **381,** 678-680 (1996).
[16] Lourie, O. & Wagner, H. D. Evaluation of Young's modulus of carbon nanotubes by micro-raman spectroscopy. *J. Mater. Res.* **13 (9),** 2418-2422 (1998).
[17] Tibbetts, G. G. & Beetz Jr, C. P. Mechanical properties of vapour-grown carbon fibers. *J. Phys. D: Appl. Phys.* **20,** 292-297 (1987).

[18] Natsuki, T. & Endo, M. Stress simulation of carbon nanotubes in tension and compression. *Carbon* **42,** 2147-2151 (2004).
[19] Liew, K. M., He, X. Q. & Wong, C. H. On the study of elastic and plastic properties of multi-walled carbon nanotubes under axial tension using molecular dynamics. *Acta Mater.* **52,** 2521-2527 (2004).
[20] Kuzumaki, T., Hayashi, T., Ichinose, H., Miyazawa, K., Ito, I., & Ishida, Y. In-situ observed deformation of carbon nanotubes. *Phil. Mag. A.* **77 (6),** 1461-1469 (1998).
[21] Park, B. C., Jung, K. Y., Song, W. Y., Beom-Hoan, O, Ahn, S. J. Bending of a carbon nanotube in vacuum using a focused ion beam. *Adv. Mater.* **18,** 95-98 (2006).
[22] Wong, W., Sheehan, P. E. & Lieber, Ch. M. Nanobeam mechanics: elasticity, strength and toughness of nanorods and nanotubes. *Science* **277,** 1971-1975 (1997).
[23] Salvetat, J. P. Briggs, G., Andrew D., Bonard, J. M, Bacsa, R. R., Kulik, A, J. Stockli, T. & Burnham, N. A. Elastic and shear moduli of single- walled carbon nanotubes. *Phys. Rev. Lett.* **82 (5),** 944-947 (1999).
[24] Yakobson, B. I., Brabec, C. J. & Bernholc, J. Nanomechanics of carbon nanotubes: instabilities beyond linear response. *Phys. Rev. Lett.* **76 (14),** 2511-2514 (1996).
[25] Lu, J. P. Elastic properties of carbon nanotubes and nanoropes. *Phys. Rev. Lett.* **79 (7),** 1297-1300 (1997).
[26] Yao, N. & Lordi, V. Young's modulus of single-walled carbon nanotubes. *J. App. Phys.* **84 (4),** 1939-1943 (1998).
[27] Zhou, X., Zhou, J. J. & Ou-Yang, Z. C. Strain energy and single-wall carbon nanotubes calculated from electronic energy-band theory. *Phys. Rev. B* **62 (20),** 13692-13696 (2000).
[28] Overney, G., Zhong, W. & Tomanek, D. Structural rigidity and low-frequency vibrational-modes of long carbon tubules. *Z. Phys. D.* **27 (1),** 93-96 (1993).
[29] Gao, G. H., Cagin, T. & Goddard, W. A. Energetics, structure, mechanical and vibrational properties of single-walled carbon nanotubes.. *Nanotech.* **9 (3),** 184-191 (1998).
[30] Nardelli, M. B., Yakobson, B. I. & Bernholc, J. Brittle and ductile behavior in carbon nanotubes. *Phys. Rev. Lett.* **81 (21),** 4656-4659 (1998).
[31] Huang, J. Y. Chen, S., Wang, Z.Q., Kempa, K., Wang, Y.M., Jo, S.H., Chen, G., Dresselhaus, M.S. & Ren, Z.F. Superplastic carbon nanotubes. *Nature* **439,** 281 (2006).
[32] Daraio, Ch., Nesterenko, V. F., Aubuchon, J. F. & Jin, S. Dynamic nanofragmentation of carbon nanotubes. *Nano Lett.* **4 (10),** 1915-1918 (2004).
[33] Yeak, S. H., Ng, T. Y. & Liew, K. M. Multiscale modeling of carbon nanotubes under axial tension and compression. *Phys. Rev. B* **72,** 165401-1-8 (2005).
[34] Ru, C. Q. Effect of van der Waals forces on axial buckling of a double-walled carbon nanotube. *J. App. Phys*. **87 (10)**, 7227-7231 (2000).
[35] Ru, C. Q. Degraded axial buckling strain of multi-walled carbon nanotubes due to interlayer slips. *J. Appl. Phys.* **89,** 3426-3433 (2001).
[36] Waters, J. F., Riester, L. Jouzi, M. Guduru, P. R. & Xu, J. M. Buckling instabilities in muliwalled carbon nanotubes under uniaxial compression. *Appl. Phys. lett.* **85 (10),** 1787-1789 (2004).

[37] Waters, J. F., Riester, L. Jouzi, M. Guduru, P. R. & Xu, J. M. Mechanics of multi-walled carbon nanotubes under uniaxial compression. *ASME Proc.* **IMECE2004-62060,** 493-498 (2004).
[38] Jeng, Y. R., Tsai, P. C. & Fang, T. H. Molecular-dynamics studies of bending mechanical properties of empty and C60-filled carbon nanotubes under nanoindentation. *J. of Chem. Phys.* **122,** 224713-1-8 (2005).
[39] Berber, S., Kwon, Y. K. & Tomanek D. Unusually high thermal conductivity of carbon nanotubes. *Phys. Rev. Lett*. **84 (20),** 4613-4616 (2000).
[40] Kim, P., Shi, L., Majumdar, A. & McEuen, P. L. *Phys. Rev. Lett.* **87 (21),** 215502-1-4 (2001).
[41] Hone, J., Whitney, M., Piskoti, C. and Zettl, A. Thermal conductivity of single-walled carbon nanotubes. *Phys. Rev.* **B 59 (4),** 2514-2516 (1999).
[42] Yang, D. J., Wang, S. G., Zhang, Q., Sellin, P. J. & Chen, G. Thermal and electrical transport in multi-walled carbon nanotubes. *Phys. Lett. A.* **329,** 207-213 (2004).
[43] Fan, Sh., Chapline, M. G., Franklin, N. R., Tombler, T. W., Cassell, A. M. & Dai, H. Self-oriented regular arrays of carbon nanotubes and their field emission properties *Science* **283**, 512-514 (1999);
[44] Ajayan, P. M. & Banhart, F. Nanotubes strong bundles. *Nature* **3,** 135-136 (2006).
[45] Kis, A., Csanyi, G., Salvetat, J.-P., Lee, T-N., Couteau, E., Kulik, A.J., Benoit, W., Brugger, J. & Forro, L. Reinforcement of single-walled carbon nanotube bundles by intertube bridging. *Nature* **3,** 153-157 (2004).
[46] Liu, J. Z., Zheng, Q. -S., Wang, L. –F. & Jiang. Mechanical properties of single-walled carbon nanotube bundles as bulk materials. *J. Mech. Phys. Solids* **53,** 123-142 (2005).
[47] Qi, H. J., Teo, K.B.K., Lau, K.K.S., Boyce, M.C., Milne, W.I., Robertson, J. & Gleason, K.K. Determination of mechanical properties of carbon nanotubes and vertically aligned carbon nanotube forests using nanoindentation. *J. of Mech. & Phys. of Sol.* **51,** 2213-2237 (2003).
[48] Oliver, W. C. & Pharr G. M. An Improved technique for determining hardness and elastic modulus using load and displacement sensing indentation experiments. *J. Mater. Res.* **7,** 1564-1583 (1992).
[49] Cao, A. Dickrell, P. L., Sawyer, W. G., Ghasemi-Nejhad, M. N. & Ajayan, P. M. Super-compressible foamlike carbon nanotube films. *Science* **310,** 1307-1310 (2005).
[50] Dresselhaus, M. S. Nanotubes a step in synthesis. Nature 3, 665-666 (2004).
[51] Yurdumakan, B., Raravikar, N. R., Ajayan P. M. & Dhinojwala, A. Synthetic gecko foot-hairs from multiwalled carbon nanotubes. *Royal. Soc. Chem.*, 3799-3801 (2005).
[52] Gu, Ch., Gao, G. –H., Yu, Y. –X. & Mao Z. –Q. Simulation study of hydrogen storage in single walled carbon nanotubes. *Int. J. of Hyd. Ener.* **26,** 691-696 (2001).
[53] Dai, H. Nanotubes as nanoprobes in scanning probe microscopy. *Nature* **384,** 147-150 (1996).
[54] Suhr, J., Koratkar, N., Keblinski, P. & Ajayan, P. Viscoelasticity in carbon nanotube composites. *Nature* **4,** 134-137 (2005).

CHAPTER THREE

3 PREPARATION, GROWTH AND EXPERIMENTAL SETUP FOR TESTING CARBON NANOTUBE TURFS

3.1 Sol-Gel Solution Preparation and Spinning

In order to grow vertically aligned carbon nanotubes using chemical vapor deposition technique, a sol gel solution containing a catalyst capable of disolving carbon atoms had to be spun on the one sided polished silicon wafer. The catalyst used in the growth may affect the growth properties of carbon nanotubes. Iron particles were used as the catalyst for the growth of all the turfs used in the experimental work.

The sol-gel solution preparation is a time dependent process. In a beaker, 10ml of ethyl alcohol (ethanol) were mixed with 10ml of tetraethyl orthosilicate (TEOS). The mixture was stirred for 15 minutes. 4.36g of Iron Nitrate ($Fe(NO_3)_3.9H_2O$), was then stirred and diluted in 15ml of distilled water. The solution was then added to the Ethanol-TEOS solution, and the mixture was then stirred for 20 minutes. Finally 2 to 3 drops of Nitric Acid $H(NO_3)_3$ were added to the mixture and the final solution was stirred for an extra 15 minutes. Upon completion, the solution was aged for a period of time ranging from 12 to 24 hours at room temperature prior to use. 24 hours later the brown-orange solution was ready to be spun on a clean polished silicon wafer. Figure 3.1 shows a timeline that summarizes the steps required for sol-gel production.

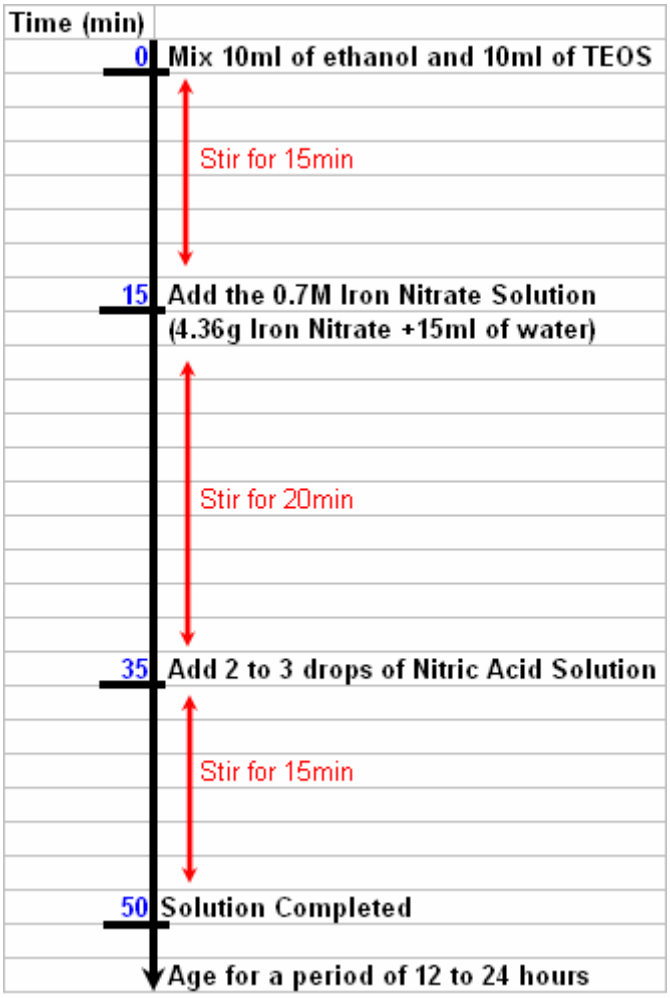

Figure 3.1 Sol-Gel Mixture timeline

Patterning Sol-Gel onto a one sided polished wafer is a process performed in a clean room and it is done using a photolithography technique that results in a transfer of a pattern from a photomask to the surface of the wafer. Being interested in getting features as small as 5µm onto the wafer AZP4620 was used as the photoresist. Since AZP4620 is a positive resist, meaning that the portion of this photoresist that is exposed to the ultraviolet light becomes soluble once developed, a positive chrome mask having the pattern to be transferred in chrome deposited onto glass was used.

A one sided polished silicon wafer was first cleaned as follows: acetone was applied onto the wafer to remove any organics, the acetone residue was then cleaned using isopropanol alcohol (IPA), which was then washed with DI water. The wafer was then washed with acetone and IPA for a second round and dried using a Nitrogen flow. It was then dropped in a BOE bath for 1 minute which removed any naturally formed oxide, and prepared the surface to allow sol-gel to stick. In order to avoid any Sol-Gel sticking issues due to the presence of distilled water on the wafer, the wafer was dehydrated on a heater at 160ºC for 5 minutes.

Once cleaned, the wafer was placed on a spinner, which was set to spin at 3000rpm for 30 seconds. Insoluble particles of iron nitrate within the Sol-Gel solution may cause the formation of comets on the wafer surface which may leave areas with no Sol-Gel stuck on. To avoid this issue, 3ml of Sol-Gel were placed in a syringe, and filtered through a 0.2 μm filter, then deposited onto the wafer. The wafer was immediately spun at 3000rpm for 30 seconds, which left a layer of sol-gel on the wafer. The sol-gel layer formed was then baked on a heater at approximately 80ºC for 24 hours.

Following the sol-gel baking, the wafer was replaced on a spinner set to spin at 3500rpm for 19 seconds, and using a pipette, the AZP4620 photoresist was dropped on the wafer which was immediately spun at the rpm and time specified above forming a photoresist layer with less than 5 μm in thickness. The pohtoresist was then soft-baked at 70º for 5 minutes. Using a positive mask the wafer was exposed to ultraviolet light for 60 seconds and immediately dropped in a beaker containing 4 to 1 mixture of water and AZ400K developer for 55 seconds, which removed the exposed portion of the photoresist. Once cleaned with water the wafer was post-baked at 110°C for 10 minutes.

Since BOE etchant reacts to the Sol-Gel, while leaving the developed photoresist layer intact, the wafer was dropped in BOE for 12 seconds which resulted in the removal of the unprotected Sol-Gel layer. The developed photoresist remaining intact protected the sol-gel dots beneath from BOE. Finally the developed photoresist was removed using acetone, leaving a sol-gel pattern with the required resolution. The figure below shows a simplified schematic of the sol-gel patterning procedure.

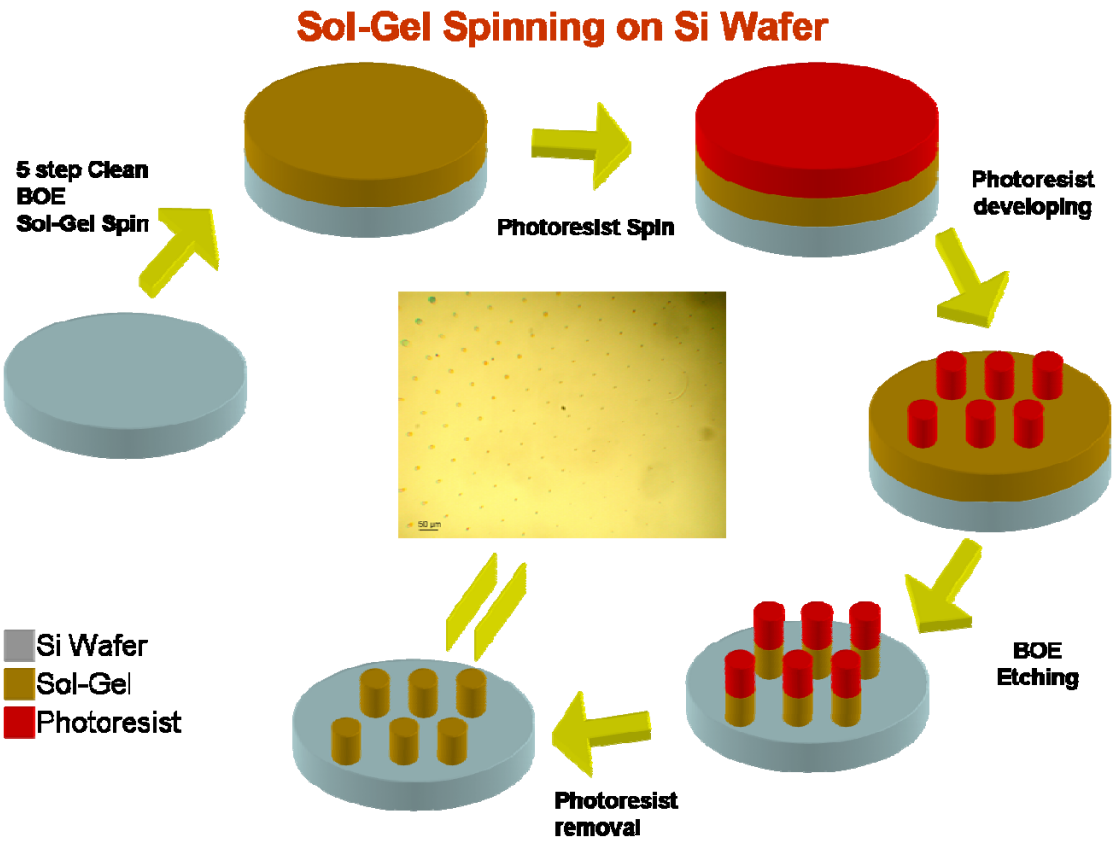

Figure 3.2 Summary of sol-gel patterning procedure

The use of a more careful procedure and a different photoresist than the standard procedure available in literature was justified by the fact that sol-gel dots with resolutions as small as 5 μm in diameters were required which would have been hard to produce using standard procedures.

Turfs for the purpose of mechanical testing such as buckling and nanoindentation, were 300 μm in diameter and produced by patterning the wafer using the mask shown below.

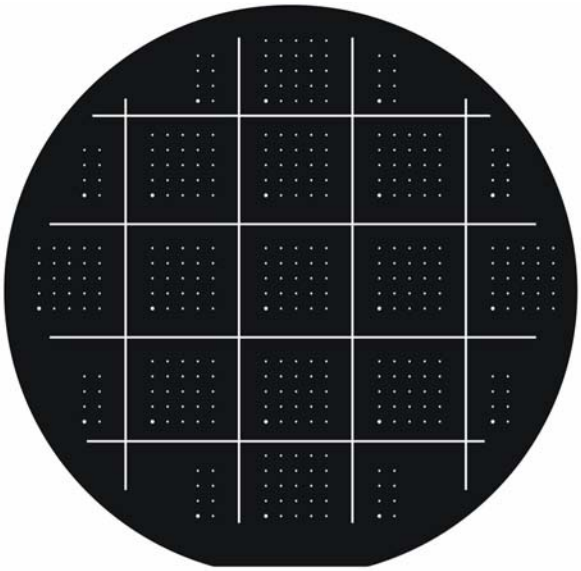

Figure 3.3 Mask used in the photolithography technique to produce dies with 300 μm diameter sol-gel dots. CNT turfs were grown on these dots for the purpose of mechanical testing such as turf buckling and nanoindentation experiments.

3.2 Carbon nanotubes growth technique

Several growth techniques have been successfully implemented since the first observation of Carbon Nanotubes by Ijima in 1991[1]. One of the first successful techniques was Arc-discharge and Ablation technique, which required a high growth temperature that resulted in evaporation of Carbon, but resulted in Multiwalled Carbon Nanotubes with a low defect density[2]. However a more efficient growth technique has been implemented in the past few years, a technique that uses lower growth temperature.

The technique is known as Chemical Vapor Deposition or CVD, and it was used as the growth technique for the CNT turfs that were tested and studied within this thesis.

Chemical vapor deposition (CVD) which usually refers to "thermal chemical vapor deposition", as opposed to "plasma enhanced chemical vapor deposition (PECVD)", has been highly used for production of patterned carbon nanotube over a substrate surfaced by a catalytic solution. The result was CNT turfs with vertically aligned MWCNTs. It is necessary to note that the resulting vertical alignment of MWCNT is the result of the support provided by neighboring nanotubes to each others via weak and short range van der Waals bonding[3]. The first so called vertically aligned CNTs were grown by Terrones in 1997[4] using a laser ablation technique. Since then, and due to the promising potential applications of CNT turfs, a technique that produced these turfs at an acceptable rate and wall defect had to be developed. Chemical vapor deposition had been used to grow nanotube fibers and materials for over 20 years. It was thus implemented for high production of patterned vertically aligned CNT turfs, and had to undergo several enhancements and modifications to control the characteristics and properties of the turfs that were produced.

The procedure used to grow the turfs tested and studied within this dissertation was accomplished using the method originally described by Dong et al[5]. The silicon dies with the sol-gel pattern produced as described earlier were put in a furnace, which was evacuated down to 0.03 Torr. The catalyst embedded in the sol-gel solution was then calcinated at a temperature of 450ºC for 2 hours, and then activated at 500ºC in an H_2 environment at 75 Torr. Carbon nanotube growth was then initiated at 700ºC by flowing a hydrocarbon gas mixture (in this case C_2H_2) mixed with H_2 into the chamber. At this

temperature, the hydrocarbon gas dissociated and carbon atoms are dissolved into the iron particle catalysts, and when precipitated are bonded to each other with sp2 bonds in a tubular shape, thus producing carbon nanotubes. The furnace chamber was finally evacuated again down to 0.03 Torr, and allowed to slowly cool, before removing the resulting patterned vertically aligned carbon nanotube turfs.

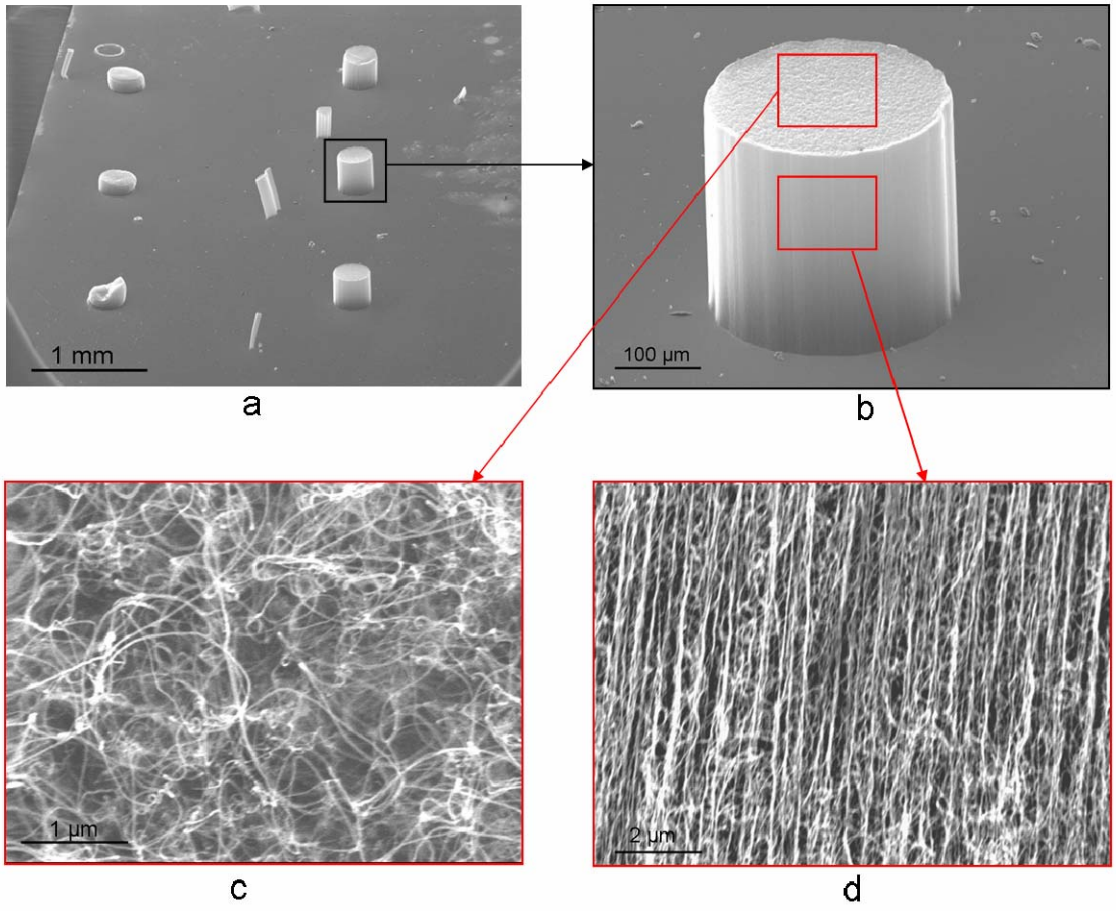

Figure 3.4 SEM photos of CNT turfs grown by chemical vapor deposition. Figure 1a shows a patterned array of CNT turfs, while figure 1b shows a CNT turf with a 300 µm diameter used for mechanical testing. Figure 1c and 1d are close ups to the turfs top and side respectively. Figure 1d reveals the vertically aligned carbon nanotube supporting each other through van der Waals bonds.

3.3 CNT Growth modes

As hydrocarbon gases flowing into the CVD chamber dissociate, vaporized carbon atoms are dissolved on the saturated iron particle embedded in the sol-gel solution, and when precipitated bond in sp2 thus forming a tubular shape. However, depending on several growth conditions, and the catalyst used two CNT growth modes have been observed, as described in the schematic shown on figure 3.5. As carbon atoms dissolved and bonded in a tubular shape, the iron catalyst particle can remain bonded and embedded in the sol-gel solution, while the resulting carbon nanotube grows out of the particle as more carbon atoms dissolved onto the particle. This is characterized as the first growth mode, and was observed when iron or cobalt particles were used as catalysts. In case of the second mode, carbon atoms dissolved and formed a tube that lifted the catalyst particle up. CNT growth in this case was stopped due to the formation of a "poisonous" layer of carbon which covered the catalyst particle, and thus isolated it from attracting vaporized carbon atoms.

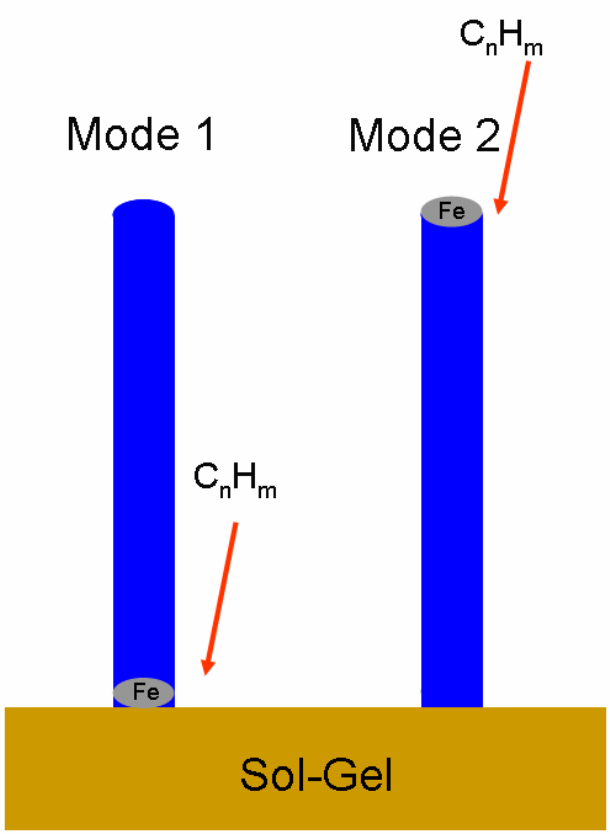

Figure 3.5 Illustration of CNT Growth modes.

SEM images of some of CNT tips of the turfs that were grown for the purpose of mechanical testing were captured. Figure 3.6 shows 4 SEM images of 4 CNT tips in this study. Figure 3.6a, b and c showed a uniform tip formation which was also brighter that the rest of the tube. Iron particle being denser than CNTs, would result in a higher secondary electron emission, and thus would look brighter on an SEM image. This suggests that growth mode 2 may be occurring, as opposed to mode 1, and that growth may have been stopped because of the "poisonous" CNT layer that covered the particle. However figure 3.6d showed a CNT tip with a non uniform cap formation, which may be the result of the iron particle breaking away and thus stopping the tube growth. These random observations seemed to convey that the second growth mode was favored using

iron particles as catalyst and under the growth conditions and parameters described in the previous section.

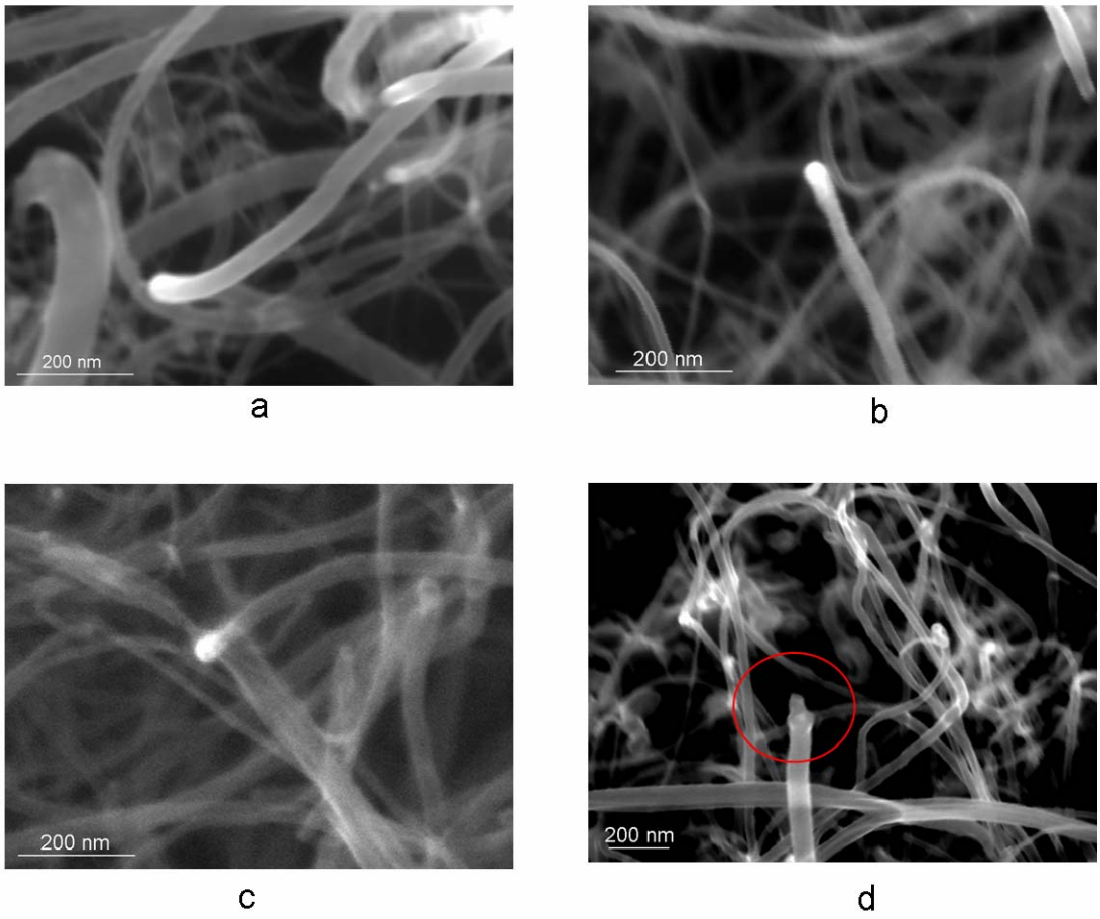

Figure 3.6 SEM images of CNT tips. Figure 6a, b & c show uniform and relatively brighter tip formation, suggesting a mode 2 growth, where the catalyst particle resided at the tip of the tube as opposed to remaining embedded in the sol-gel solution. Figure 6d shows a non uniform tip formation suggesting that the iron particle may have broke away and thus stopping the CNT growth.

3.4 Nanoindentation Experimental Setup for Carbon Nanotube Testing

3.4.1 Overview of nanoindentation

Indentation techniques have long been used to measure elastic properties of materials. One particular property that has been measured using indentation was hardness or mean pressure, defined as the maximum applied load over the contact area between the tip and the sample surface. This property was first measured qualitatively for one material with respect to another, but was then quantified using macroscopic indentations[6].

Over the past two decades, instrumented nanoindentation techniques have been developed, which allowed for load-depth monitoring and measuring properties of materials at the nanoscale level. These techniques have revolutionized materials research as several properties and characteristics of materials, including but not limited to, elastic properties such as the reduced modulus and hardness, dislocation motion and plastic properties such as the onset of plastic deformation[7], became easily deduced from load-depth curves of subsequent indents.

A Hysitron Triboscope in conjunction with a Park Scientific Autoprobe CP scanning probe microscope was used to conduct nanoindentation experiments. It consisted of a Hysitron head onto which a Berkovich tip was loaded. As shown in figure 3.7, the head consisted of three parallel plates forming a triple plate capacitor, with small holes in the 2nd and 3rd plate to accommodate the tip mounting. The indenter tip is held by springs located within a triple plate capacitor. To produce an indent a voltage is applied between the plates which causes the springs to deflect downward as illustrated in figure 3.7, thus registering a compressive load. An upward deflection beyond the original position would be registered as a tensile load. Measuring the change in capacitance

allows for displacement monitoring. The Hysitron portion of the system monitors the applied load and the resulting displacement simultaneously, to generate load-depth curves for the sample being tested.

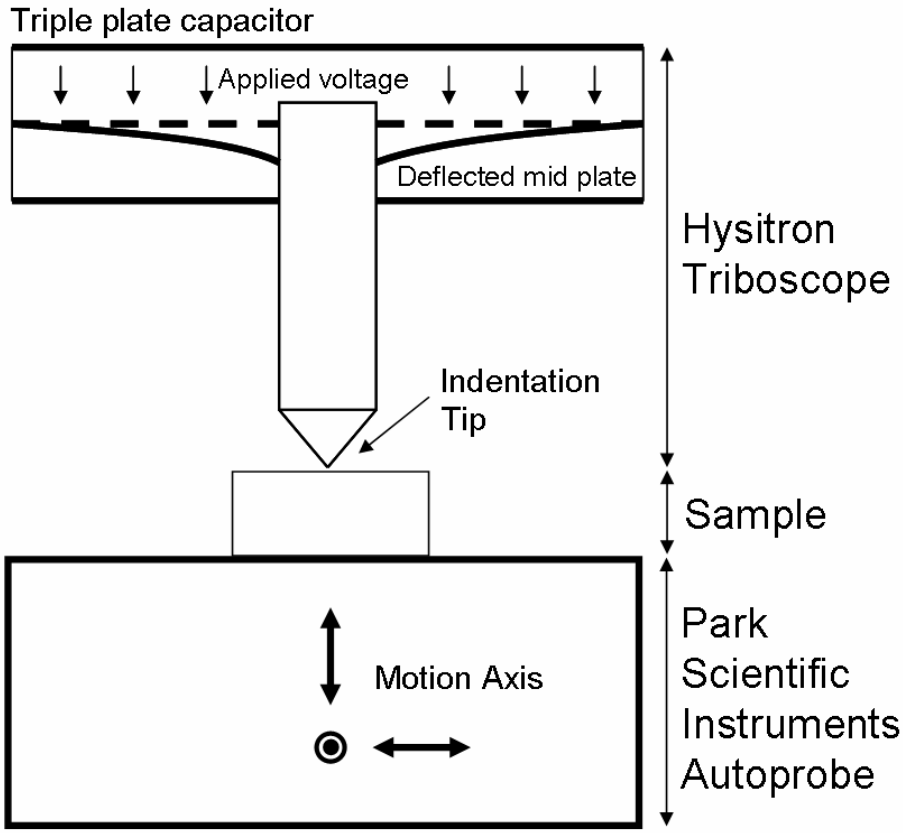

Figure 3.7 An illustration of the Indenter system used to conduct nanoindentation experiments. The system is a hybrid between a Hysitron Triboscope and a Park Scientific Autoprobe CP scanning probe microscope

The sample being tested was mounted on the Park Scientific Autoprobe section of the system. The Autoprobe consisted of a tri-axial motion system which may be controlled manually and automatically. While nanoindentation tests were conducted, the Autoprobe applied a constant voltage, which held the sample at a constant height.

3.4.2 Performing Indents and Extracting the Elastic Properties

Several techniques have been developed over the years to extract the elastic properties out of the indentation load-depth curves for a given material in the most accurate way[8- 12]. However, the most accurate technique developed thus far is that of Oliver and Pharr's, which is used to analyze indents conducted within this dissertation. The methods introduced by Oliver and Pharr, immediately extracts the hardness and the reduced modulus of the sample using the following equations:

$$H = \frac{P_{max}}{A}, \qquad (1)$$

And

$$E_r = \frac{\sqrt{\pi}}{2}\frac{1/C_s}{\sqrt{A}} \qquad (2)$$

where S is the initial unloading slope of the load depth curve, and A is the contact area between the indenter tip and the sample. A power law is used to curve fit the unloading segment of the indentation load-depth curve as follows:

$$P = A(h - h_f)^m \qquad (3)$$

where A, h_f or the permanent depth following an indent and m are constant determined using a least square fit techniques. Knowing the initial unloading slope S from the power law curve fit of the upper portion of the unloading segment, and knowing the frame compliance C_f, the sample compliance C_s can be calculated as follows:

$$\frac{1}{S} = C = C_f + C_s \qquad (4)$$

The contact area value is calculated knowing the geometry of the tip in use and the contact depth h_c. For a Berkovich tip, the area function is calculated as follows:

$$A = 24.5h_c^2 + \sum_1^n C_m h_c^{1/n} \qquad (5)$$

Where m is an integer and Cm are determined experimentally as described in Oliver and Pharr's 2nd appendix. Finally the elastic modulus E of the material being tested may be determined having calculated the reduced modulus and knowing the elastic modulus and Poisson's ratio of the diamond tip (E_d=1249 GPa, and ν_d=0.07 respectively) and the materials' Poisson's ratio ν, using equation 6:

$$\frac{1}{E_r} = \frac{1-\nu_d^2}{E_d} + \frac{1-\nu^2}{E} \qquad (6)$$

Figure 3.8 shows typical load-depth curves generated from indents performed on typical materials silicon Si and Tungsten W. These typical load-depth curves consisted of loading segment, followed by a hold segment, then an 80% unloading segment followed by a short hold from which the drift rate is calculated, and then a final unloading segment. Other than calculating the elastic properties from the unloading segment, dislocation dependent deformation showed an excursion or a jump in the loading segment, as is shown on figure 3.8b in case of W, thus characterizing the onset of plastic deformation.

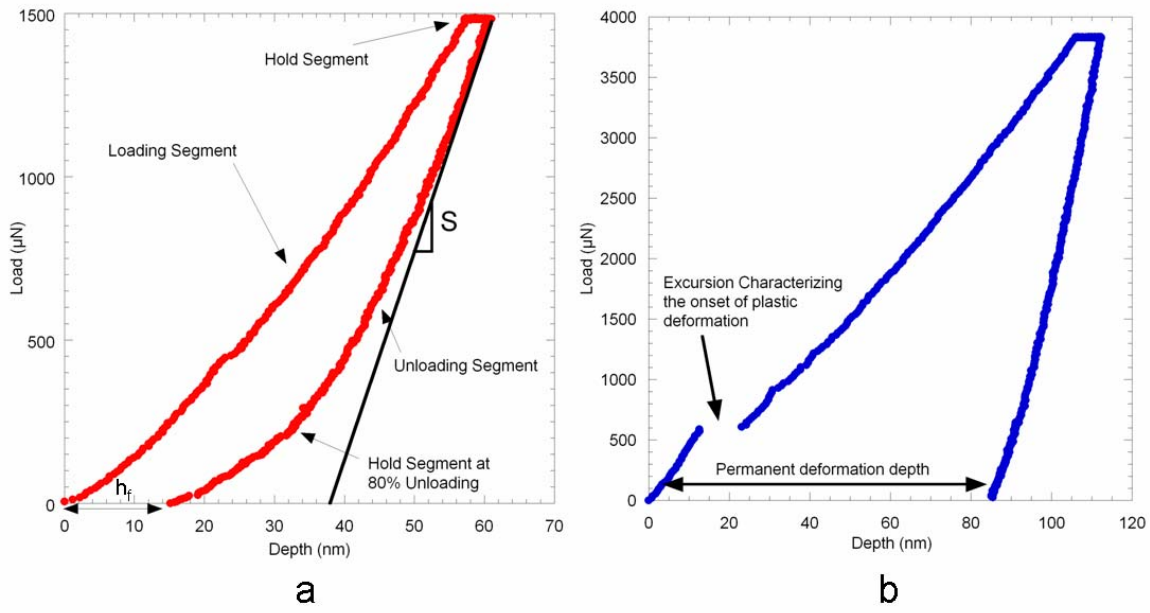

Figure 3.8 Typical load depth curves resulting from indenting Si and W.

Indenting CNT turfs have proven to be much more challenging, and a careful experimental methodology was necessary to accurately extract the general elastic properties of these turfs, and that was due to several CNT properties that were not encountered in nanoindentation before, and which will be discussed in further detail in chapter 4.

3.4.3 Calculating the Berkovich tip Properties

As mentioned earlier, a Berkovich tip was used to conduct most of the indents on CNT turfs, thus calculating its properties was necessary to better assess and understand any generated load-depth curve and extracted properties.

A Berkovich tip is a three sided pyramidal diamond tip with well defined slopes and angles as is illustrated by Fisher-Cripps[13]. However, the Berkovich tip undergoes continuous wear, and thus has always been approximated as a conical tip with a spherical cap and a corresponding equivalent cone angle of 70.32º. Two properties in particular had

to be calculated to assess the results of CNT nanoindentation. The first one being the tip radius R, and the second one being the critical tip height h*, at which the tip shape transitions from being a spherical shape to a conical shape. This property will be particularly important when studying the adhesive properties of CNT turfs to diamond tips and employing the JKR model which only predicts the adhesive forces for spherical elastic contacts.

To calculate the tip radius, low load indents were performed on bulk single crystal W in order to generate purely elastic indents, i.e. indents that showed no excursion, sign of the onset of plastic deformation, nor any residual depth. Figure 3.9 shows a purely elastic indent performed in single crystal tungsten. Although the loading and unloading segments of the indents, overlapped, only the loading segment of the indent is shown. The segment was curve fitted using the general Hertzian elastic relationship, and the unknown tip radius R was determined using a least square fit method:

$$P = \frac{4}{3} E^* \sqrt{R \times \delta^3} \qquad (7)$$

Where δ is the tip's displacement into W. Performing this analysis on 10 different elastic indents resulted in a tip radius of 1078 nm.

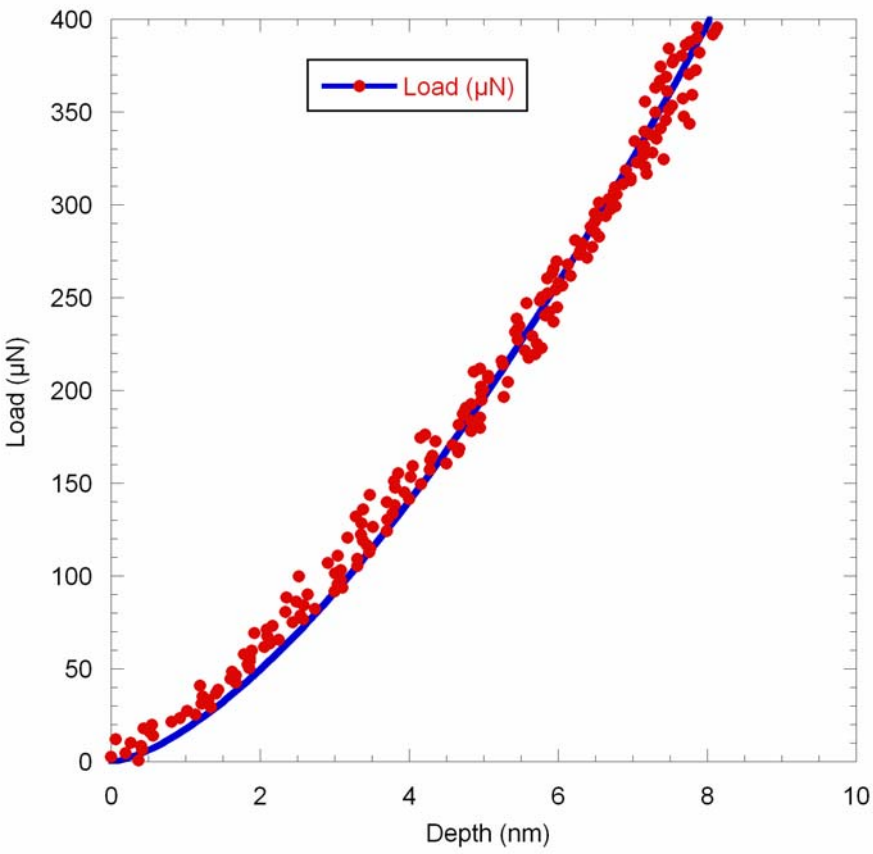

Figure 3.9 Typical purely elastic indent performed in single crystal tungsten W, along with the Hertzian elastic curve fit.

Thus, knowing the tip radius of the Berkovich tip, and its semi apical angle or equivalent cone angle θ=70.32º, the critical height at which the tip transitions from having a spherical shape to a conical shape was calculated to be 79 nm, using the following equation:

$$\frac{h^*}{R} = 1 - \sin\theta \quad [14] \qquad (8)$$

3.4.4 CNT Turfs Indentation

As was mentioned section 3.4.2 indentation of CNT turfs turned out to be much more challenging than the typical indentation of metals, thin films and polymers. While elastic and plastic properties of W and Si were easily extracted from their respective indents, the shape of the resulting load-depth curves made it much more challenging to extract these properties for CNT turfs. All these complications were the result of two unusual properties that occurred in CNT turfs and not in other materials that were indented: the fact that CNT turfs were highly compliant, and the fact that they adhered to the diamond tip in contact which highly affected the subsequent indents. Figure 3.10 shows a typical load-depth curve resulting from an indent performed on CNT turfs.

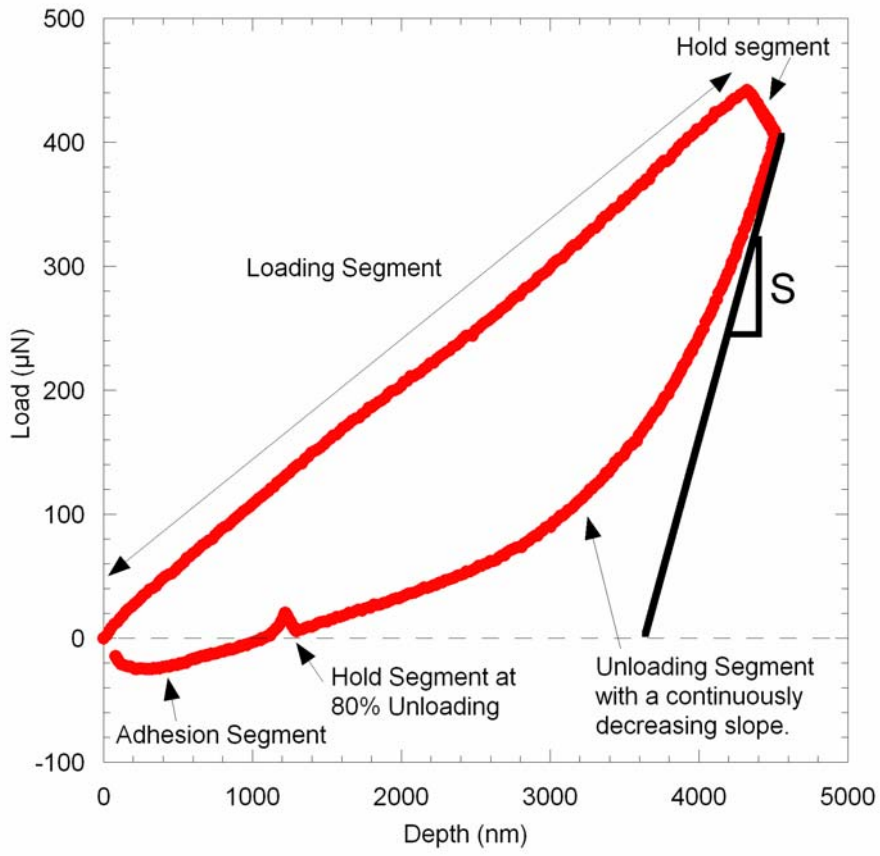

Figure 3.10 Typical Indent in CNT Turfs. A loading segment was followed by a hold segment, then an 80% unloading segment, followed by a short hold from which the drift rate is calculated and finally a complete unloading. The indent revealed the presence of a negative load, suggesting that the tubes adhered to the diamond tip.

One of the major differences observed in CNT turfs indentations, was the presence of a negative load segment during the unloading portion of the indents, which was the result of carbon nanotube strongly adhering to the diamond Berkovich tip. The indent will be analyzed in further detail in chapter 4.

Several indents were initially performed to capture the discrepancies between CNT indentations and typical indentations. One of the priorities was to make sure that the

resulting permanent adhesion of carbon nanotubes from one indent, will not affect the subsequent indents. For that purpose a set of 30 indents were performed consecutively with no tip cleaning, to determine the point at which the adhered carbon nanotubes would start affecting the property measurements. Figure 3.11 showed the result of this analysis: it was clear that following the 9^{th} indent, the calculated value of the reduced modulus E_r, dropped significantly and permanently for the indents to follow. This drop is the result of a drop in the initial unloading slope, due to the interaction between the adhered tubes and the turf, rather than the direct interaction between the diamond tip and the turf. The adhesive factor also reduced the contact area between the tip and the turf, which also affected the accuracy of the measurements.

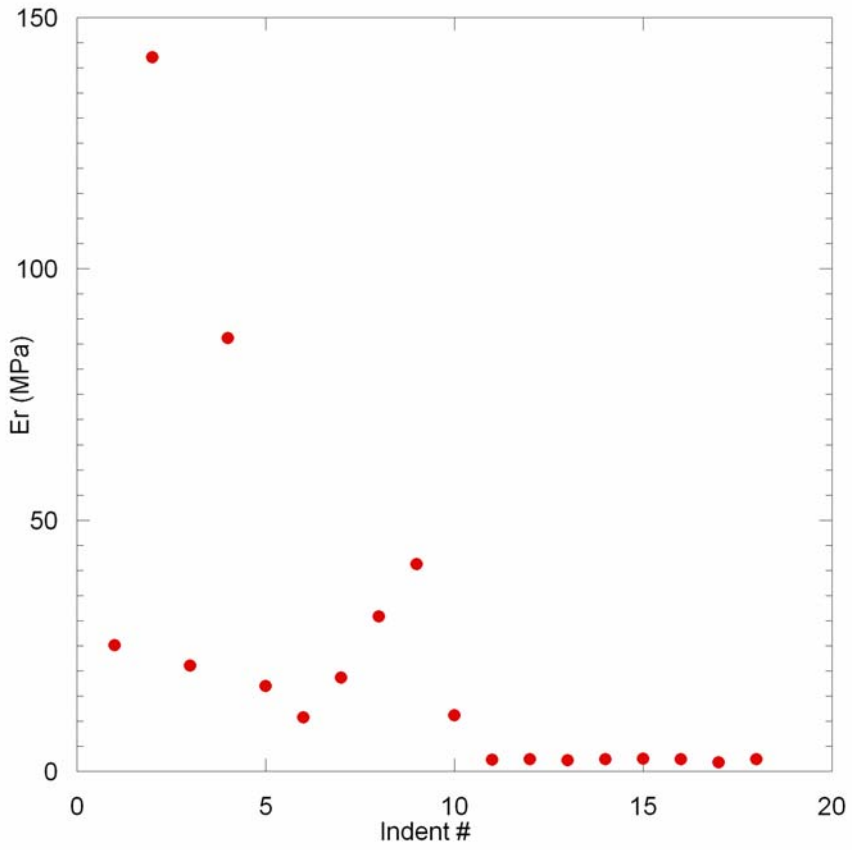

Figure 3.11 Variation in the reduced modulus measurements with consecutive indents. A permanent drop was observed following the 9th indents due to CNT-diamond tip adhesion.

To avoid these complications, the indenter tip was cleaned following every 4 indents. Tip cleaning was accomplished by indenting polystyrene thermal insulation (Styrofoam) several times, which collected the adhered CNTs due to its extensive plastic deformation.

Since the elastic properties were deduced from the unloading segments of the indents, reducing the effect of drift due to thermal and mechanical factors on the unloading portion of the indent was necessary to avoid any inaccuracies or discrepancies in the results. The effects of this factor were reduced by unloading at a high rate. The

minimum unloading rate beyond which the elastic properties measurements stabilized was determined by performing a set of indents with varying unloading rates. Figure 3.12 revealed that the elastic properties measurements (both E_r and H), stabilized beyond an unloading rate of 180 μN/sec, and therefore all consecutive indents were performed with an unloading rate higher than the critical rate.

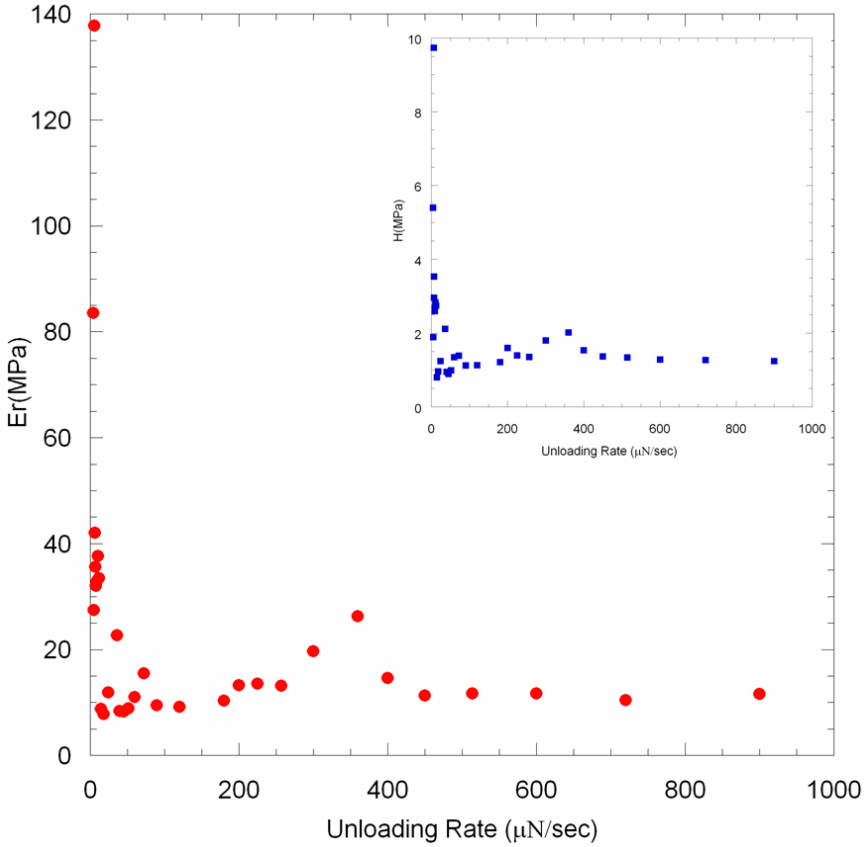

Figure 3.12 Variation of Elastic properties measurements, as a function of unloading rates. Due to drift rate both E_r and H measurements (shown in the inset) seemed to stabilize beyond an unloading rate of 180 μN/sec.

Elastic properties measurements have varied extensively between indents conducted over different turfs grown at different periods of times, which suggested that the general properties of the turfs including their densities and morphologies, elastic

modulus and hardness were highly dependent upon the growth parameters as well as the sol-gel spinning parameters. Figure 3.13 illustrates the variation in properties between indents conducted over two turfs ME07 and ME130. From looking at the load-depth curves, turf ME130 showed to be stiffer that ME07. This suggested that ME130 had a higher tube density than ME07, but since several parameters vary from one growth period to another, it would be very hard to tell what caused the growth of a denser turf: the fact that more tubes grew out of the iron particles scattered in sol-gel layer (i.e. since the two sol-gel theoretically have same particle density, would more particles engage in CNT growth under particular growth parameters), or whether the turf showed a higher tortuoasity. However, figure 3.13 also revealed that the indents performed on the same turf were consistent in shape and thus in elastic properties measurements. Also, different turfs grown at the same growth conditions and simultaneously showed consistency in the measured properties.

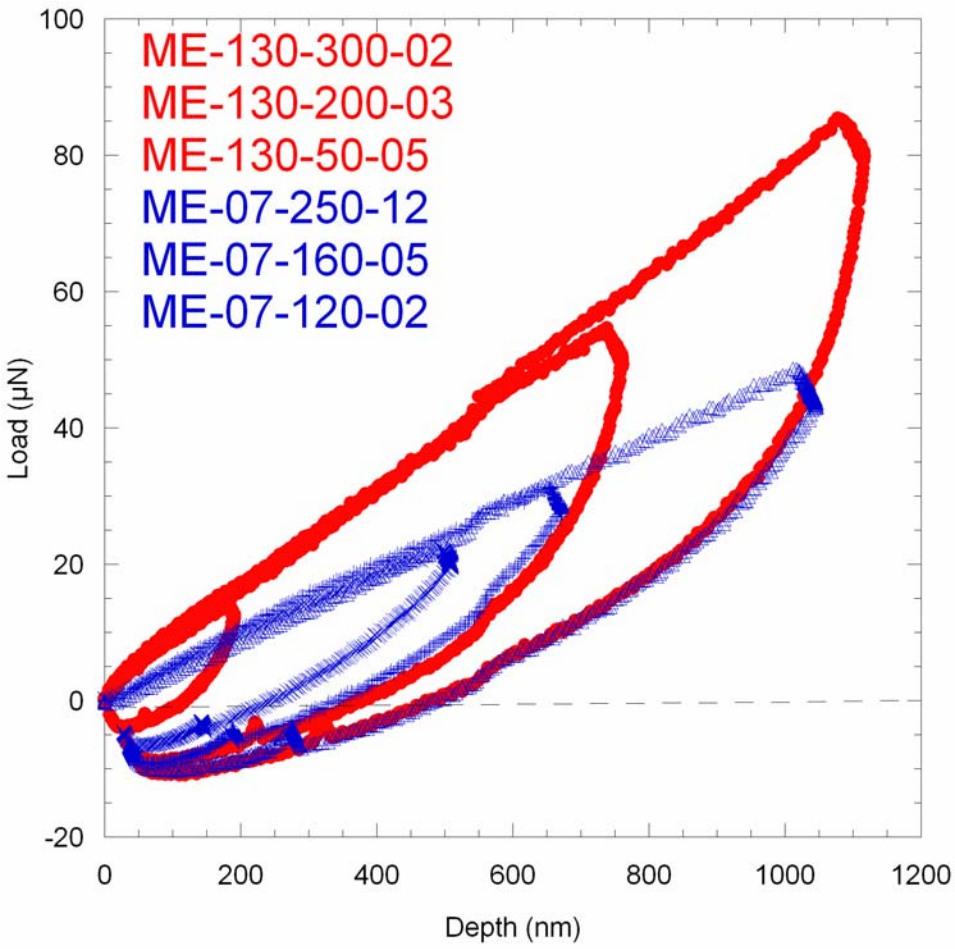

Figure 3.13 Variation in indentation results between turfs grown at different growth periods. ME130 proved to be stiffer than ME07, thus suggesting that it had a higher tube density, as a result of more tubes growing off the iron particles scattered within the sol-gel.

The importance to understand the adhesive properties between CNTs and the diamond tip as well as the effect of adhesion on the measurement of elastic properties, have launched several attempts and experimental procedure in order to reduce or eliminate adhesion of the tubes to the diamond tip. The first attempt was to coat the turf with a layer of material onto which CNTs won't adhere to. Several turfs were therefore

coated with a 300 nm thick gold layer and tested using nanoindentation as well. The results showed that unlike the case of non Au coated turfs, Au coated turfs had low adhesion measurements, and adhesion forces were independent of the maximum applied load. However, the Au coating seemed to highly affect the turf properties as well. It is known that coating a sample with a harder coating, stiffens the general behavior of the turf. However, gold coating a CNT turf showed a softening effect rather than a stiffening effect. This unexpected observation, a property of turf like materials, will be discussed in chapter 4 and related to the presence of van der Waals bonding between adjacent tubes, which played a role in stiffening the turf, although it allowed the adjacent tubes to slide over each other under applied compressive loading. Gold coating the turf and the fact that it coated individual tubes, seemed to eliminate the weak van der Waals bonding between the tubes, and thus had a softening behavior on the general behavior of the turf. This topic along with an explanation of van der Waals bonding effect on the general mechanical behavior of the turf will be further expanded in chapter 4. Also indents performed on several locations over the same gold coated turf were inconsistent in shape and elastic properties measurements which could be explained by the fact that gold sputtering results in an uneven layer of gold across the sample's surface. Figure 3.14 emphasized the discrepancies addressed above by comparing indents performed on gold turfs to each other as well as to indents performed on non Au coated turfs.

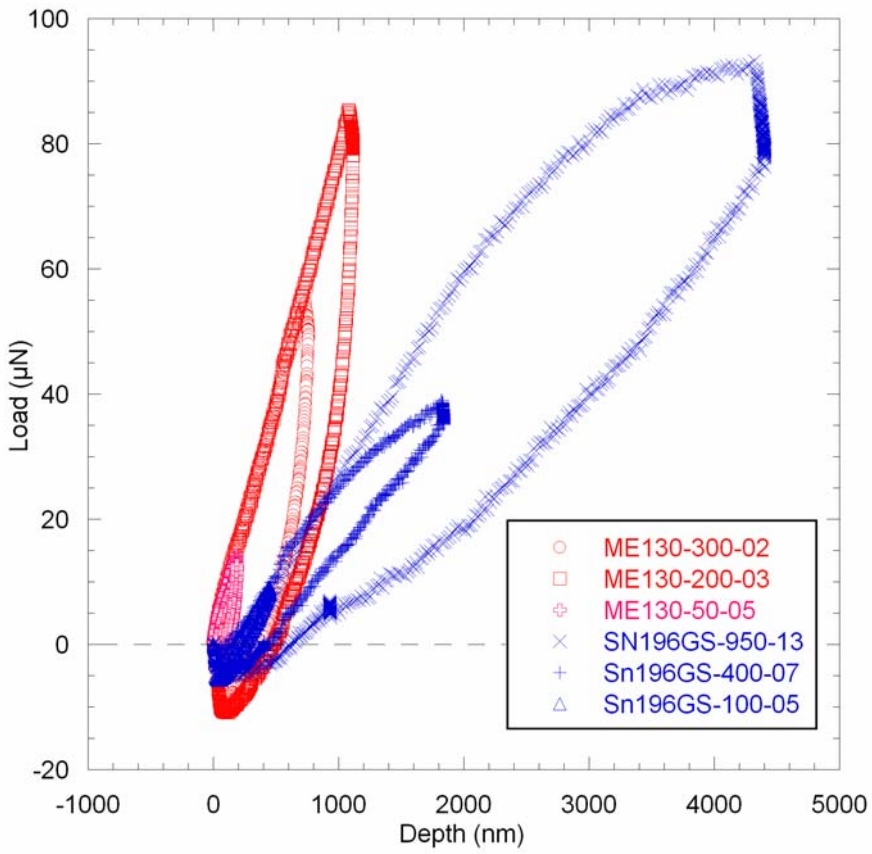

Figure 3.14 Indents in Au coated CNT turfs vs. indents in non Coated CNT turfs. Au coat reduced the resulting adhesive force as compared to non coated turfs adhesive forces, but also highly affected the indents' shape and properties, and resulted in inconsistent measurements across the turfs' surface.

The discrepancies and the complications introduced by gold coating CNT turfs, proved the necessity of gold coating the diamond tip in order to understand the effect of adhesion on measured elastic properties. But to avoid ruining the diamond Berkovich tip with an added gold layer, a record diamond needle tip was modified and mounted to be used as an indenter tip. The record needle is a diamond conical tip with a spherical tip radius of 15 µm, and was mounted on a Hysitron tip base and used to indent CNT turfs

prior to adding any coating. The record needle was then gold coated with a 30 nm layer, and several new indents with similar maximum applied loads to the indents performed earlier, were conducted on CNT turfs. Figure 3.15 shows two load-depth curves, one being a typical indent conducted prior to coating the tip, and the other one being a typical indent conducted following the tip coating. Similar to Figure 3.14, low adhesion forces were measured in presence of gold as an interlayer. However indents performed following tip coating were highly consistent at various applied loads, and had different loading and unloading shapes when compared to indents performed prior to coating the tip. This proved that adhesive forces did affect the measured elastic properties, particularly since measurements showed that the initial unloading slope decreased by 30% when comparing indents with the same maximum applied load, prior and following tip coating.

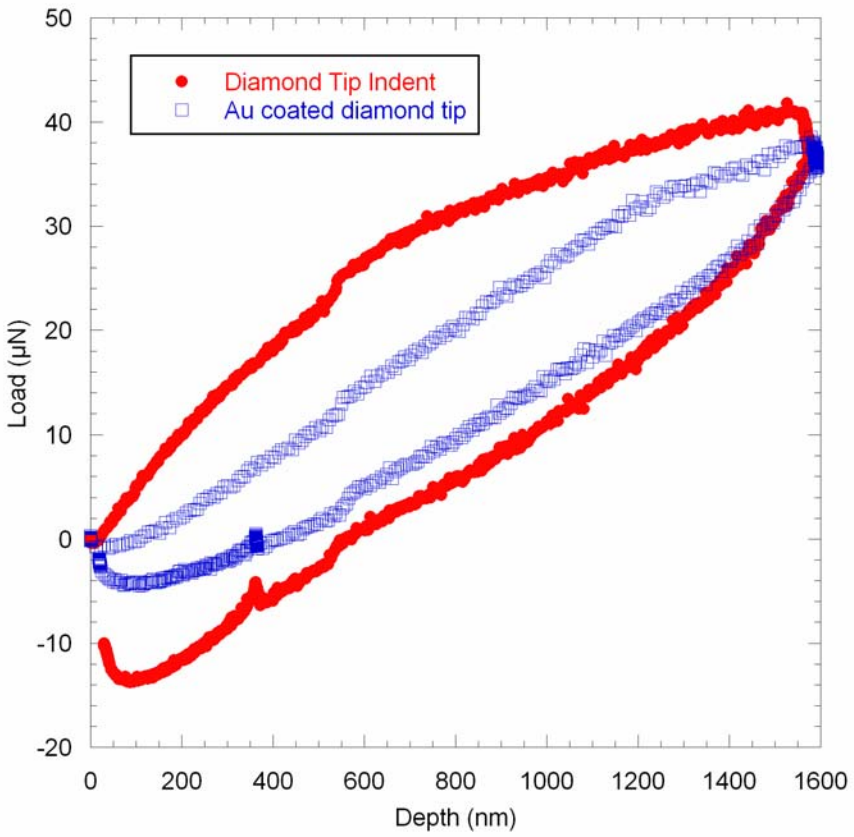

Figure 3.15 Indents prior and following record needle diamond tip coating with a 30 nm gold layer.

Finally as mentioned earlier, adhesive loads decreased to a minimum value following tip coating and were independent of the maximum applied load as is shown in figure 3.16.

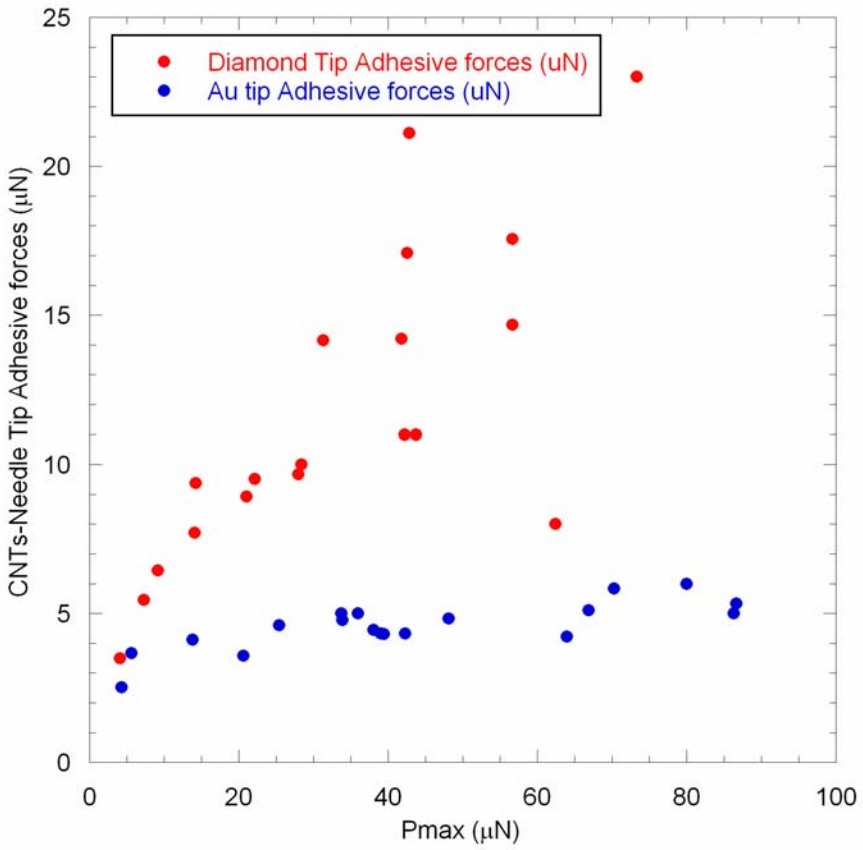

Figure 3.16 Adhesive forces vs. Maximum applied loads prior and following tip coating.

An average adhesive force, independent of maximum applied loads as well as maximum indentation depth, was measured to be 4.58 ±0.8 μN for Au coated tips

Details on general indentation results, their relation to the turfs' general mechanical behavior, van der Waals bonding between adjacent individual tubes, and the effect of adhesion forces on the accuracy of the elastic properties extracted from nanoindentation load-depth curves will be addressed in detail in chapter 4.

3.5 CNT Compressive Loading and Buckling tests

Substantial amount of experimental[15] and theoretical[16,17] work has been done on understanding deformation of a single multi-wall CNT (MWCNT) or a single single-wall CNT (SWCNT) under both tensile and compressive loads. However little has been done to understand the collective deformation of a CNT turf[18], and how carbon nanotubes deform with respect to each other. An attempt to buckle 300 μm diameter CNT turfs with various heights was made in order to understand the buckling or critical load dependence on height and turf aspect ratio. To buckle the turf a standard displacement controlled compression equipment was used, and a spherical tip was designed. Since no experimental setup guarantees a straight contact between the tip and the turf, a spherical tip with a diameter large enough (D =1.6 mm) to accommodate any alignment mismatch, but to also still conduct a flat punch experiment was designed.

Figure 3.17 shows the experimental apparatus. It consisted of a displacement controlled equipment that simultaneously recorded displacement with an LVDT and the load from a load cell onto which the spherical tip was attached.

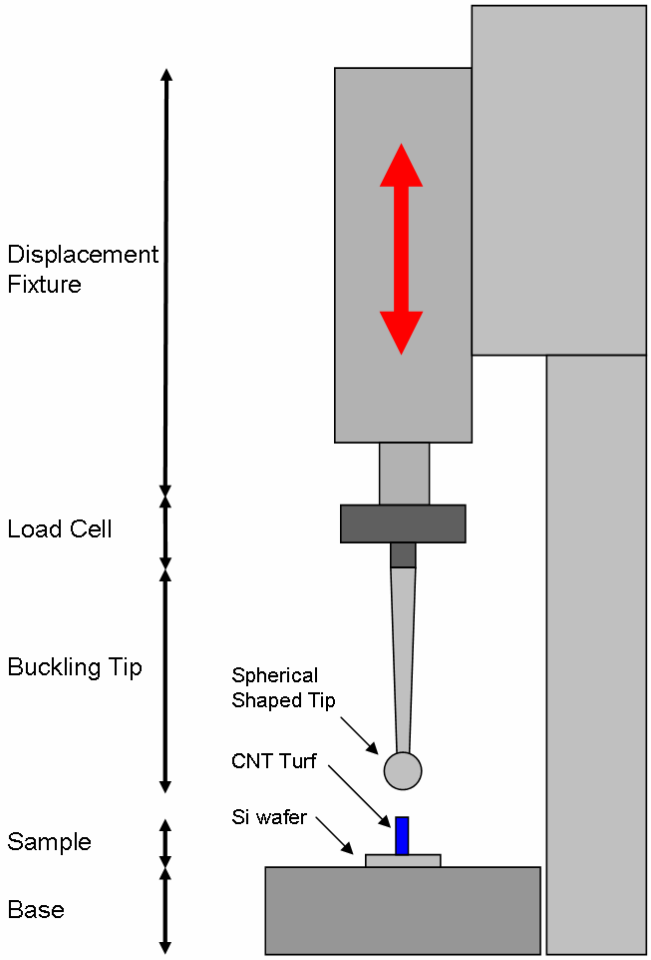

Figure 3.17 Buckling Apparatus

Testing was conducted at a low displacement rate of 0.01 μm/sec to ensure the accuracy in measuring the buckling or critical compressive load. Buckling of columns can be determined from analyzing the load-depth curve. It is defined as the critical load at which the load-depth curve reaches a plateau (constant or drop in loading for a given displacement range). The load depth curves were then transformed into stress-strain curves dividing the load by the contact area of the 300 μm turf and the by dividing the change in displacement by the original height of the turf.

$$\sigma = \frac{4P}{\pi D^2} \qquad (9)$$

And

$$\varepsilon = \frac{\delta L}{L_0} \qquad (10)$$

Where P is the applied load, D is the diameter of the turf, L_0 is the turf's initial height and δL is the instantaneous change in height. Figure 3.18 shows a typical load-depth curve and its resulting stress-strain curve generated using the described apparatus.

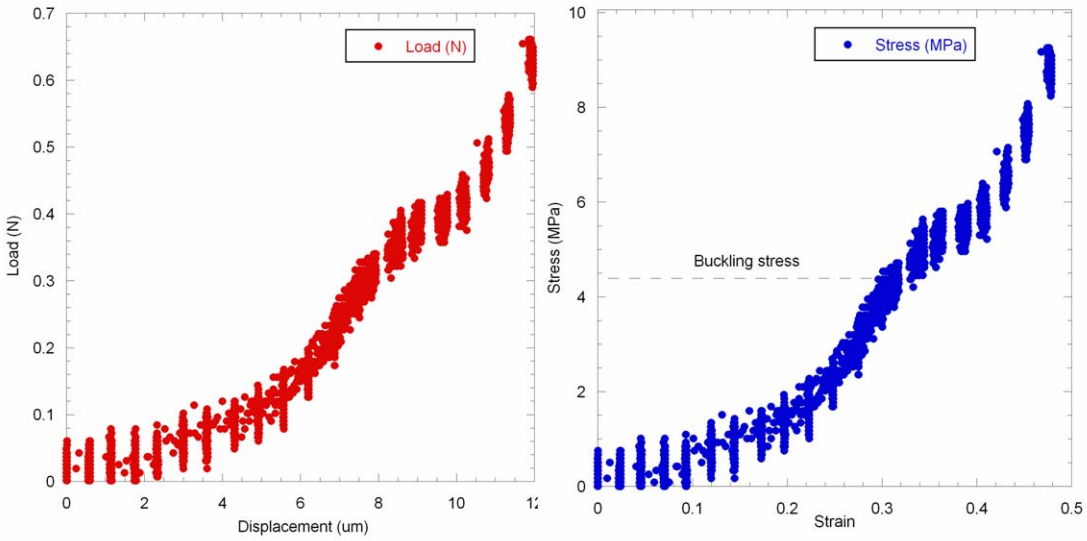

Figure 3.18 Load-depth curve and its corresponding stress-strain curve showing the buckling stress.

In cases where noise generated by the compression apparatus was large, a smoothing factor was added to the generated load depth curve prior to measuring the buckling load: each twenty generated data points were averaged, and only their average was displayed on the plot, which provided a more accurate reading of the buckling load as is shown in Figure 3.19.

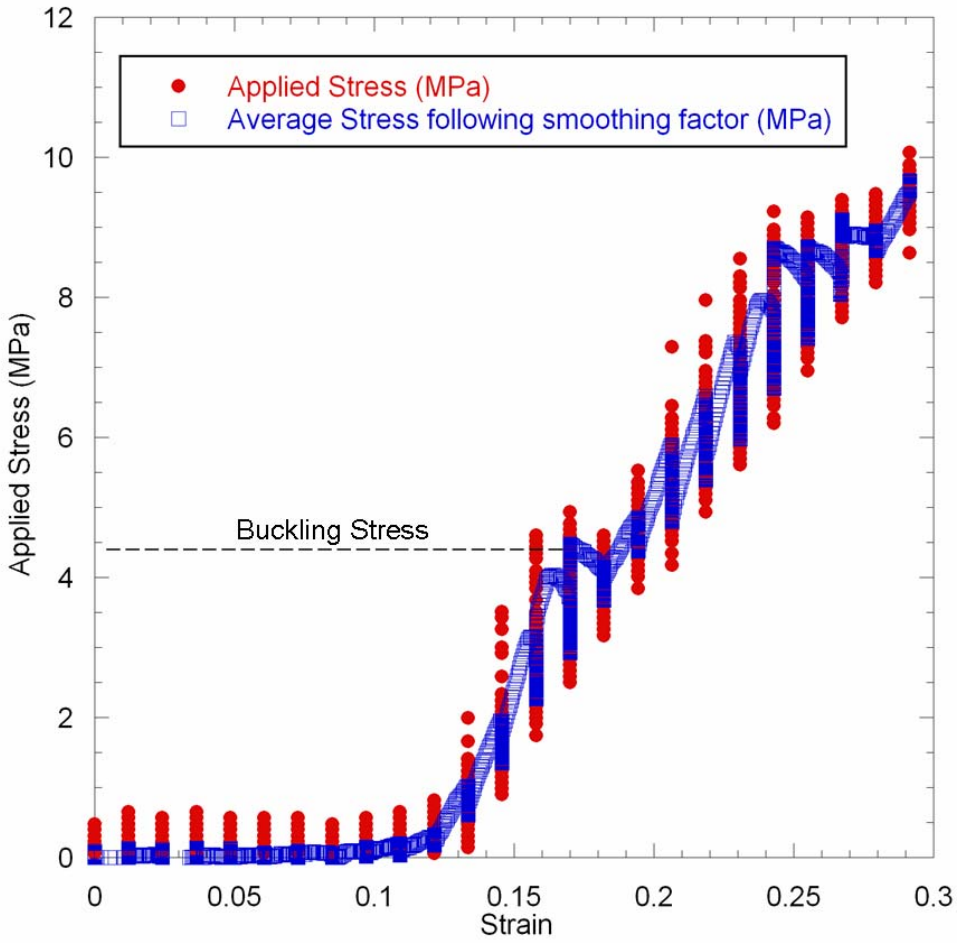

Figure 3.19 Stress-strain curve of a buckled turf, comparing the original plot to a smoothed plot.

3.6 References

[1] Iijima, S. Helical microtubules of graphitic carbon. *Nature* **354,** 56-58 (1991).
[2] Dresselhaus M. S., Dresselhaus G. & Avouris Ph. Carbon nanotubes synthesis, structure, properties and applications. *Springer.* 30-53 (2001)
[3] Meyyappan, M. *Carbon Nanotubes science and application*. *CRC Press*. 111 (2005)
[4] Terrones, M. et al. Controlled production of aligned-nanotube bundles. *Nature* **388,** 52-55 (1997).
[5] Dong, L., Jiao, J., Pan, C. & Tuggle, D. W. Effects of catalysts on the internal structures of carbon nanotubes and corresponding electron field emission properties. Appl. Phys. A 78, 9-14 (2004)

[6] Hertz, H. Miscellaneous papers by Heinrich Hertz, ed. D. E. Jones and G. A. Schott, *Macmillan, London.* 163-183 (1896)

[7] Zbib, A. A. & Bahr, D. F. Dislocation nucleation and source activation during nanoindentation yield point. *Met. Mat. Tran. A* **38A,** 2249-2255 (2007).

[8] Ternovskii, A. P., Alekhin, V. P., Shorshorov, M. Kh., Krushchov, M. M. & Skvortsov, V. N. Micromechanical testing of materials by depression. *Zavod. Lab.* **39, no. 10.** 1620-1624 (1973)

[9] Bulychev, S. I., Alekhin, V. P., Shorshorov, M. Kh., Ternovskii, A. P. & Shnyrev, G. D. Determining Young's modulus from the indenter penetration diagram. *Zavod. Lab.* **41, no. 9.** 1409-1412 (1975)

[10] Pethica, J. B., Hutchings, R. & Oliver W. C. Hardness measurement at penetration depths as small as 20 nm. *Philos. Mag. A* **48,** 593-606 (1983)

[11] Doerner, M. F. & Nix, W. D. J. Mater. Res. 1, 601 (1986).

[12] Oliver, W. C. & Pharr G. M. An Improved technique for determining hardness and elastic modulus using load and displacement sensing indentation experiments. *J. Mater. Res.* **7, no. 6,** 1564-1583 (1992).

[13] Fisher-Cripps, A. C. *Nanoindentation.* Springer-Verlag, New York. (2002)

[14] Vanlandingham, M. R., Juliano, T. F. & Hagon, M. J. Measuring tip shape for instrumented indentation using atomic force microscopy. *Meas. Sci. Technol.* **16,** 2173-2185 (2005)

[15] Waters, J. F., Riester, L. Jouzi, M. Guduru, P. R. & Xu, J. M. Buckling instabilities in muliwalled carbon nanotubes under uniaxial compression. *Appl. Phys. lett.* **85 (10),** 1787-1789 (2004).

[16] Yakobson, B. I., Brabec, C. J. & Bernholc, J. Nanomechanics of carbon nanotubes: instabilities beyond linear response. *Phys. Rev. Lett.* **76 (14),** 2511-2514 (1996).

[17] Yeak, S. H., Ng, T. Y. & Liew, K. M. Multiscale modeling of carbon nanotubes under axial tension and compression. *Phys. Rev. B* **72,** 165401-1-8 (2005).

[18] Cao, A. *et al.* Super-compressible foamlike carbon nanotube films. *Science* **310,** 1307-1310 (2005).

CHAPTER FOUR

4 ADHESION AND MECHANICAL DEFORMATION MECHANISMS DURING INDENTATION OF CARBON NANOTUBE ARRAYS

4.1 Abstract

CNT turfs, whether vertically arrayed or randomly grown, have been shown to have different properties than those of a single tube. Their mechanical properties were highly affected by the presence of weak, short range van der Waals bonding between the adjacent tubes. The general mechanical behavior of vertically aligned carbon nanotubes grown by chemical vapor deposition (CVD) was studied using nanoindentation techniques. Load-depth curves extracted from nanoindentation were used to calculate the elastic properties of the turfs. Turfs exhibited non-linear elastic loading, with energy dissipation evident even with no permanent deformation. The average elastic modulus of CNT turfs was 14.9 MPa ± 5.8 MPa, and the hardness was on the order of 5.5 MPa. Permanent deformation occurred at an applied compressive stress of 2.53 MPa for these turfs, and was explained in terms of mechanical tube locking within the turfs, and is suggested to be highly dependent on the CNT morphologies and density. Adhesive forces present between CNTs and the diamond tip affected the turf behavior under nanoindentation and showed to increase the initial slope of the unloading segments, thus resulted in slightly higher elastic property measurements.

4.2 Introduction

Since their discovery multi walled carbon nanotubes[1] (MWCNT) and single walled carbon nanotubes[2,3] (SWCNT) have demonstrated unique thermal[4], electrical[5] and mechanical[6] properties which enabled them to have several potential applications[7,8]. High thermal conductivities, reaching a value of 6600 W/mK, were measured by Berber et. al. On the mechanical side a high elastic modulus on average 1.8 TPa, were measured by Treacy et al., a property which coupled with their low density enables them to have applications in future composite materials. These facts have launched scientific research to unfold the relation between the growth methods[9], the morphologies and the variation in properties of carbon nanotubes. However, emerging applications of carbon nanotubes as a thermal switch[10] or as reinforcement in composite materials[11] have initiated the necessity of understanding not only the properties of single tubes, but also the properties of the collective behavior of carbon nanotubes within a carbon nanotube turf. Whether they are forest like turfs grown in vertical arrays, or randomly grown by CVD[12] on iron particles embedded in a Sol-Gel solution, CNT turfs have shown a different mechanical behavior and different properties than those of single tubes (SWCNT or MWCNT). For interconnected CNT turfs grown by chemical vapor deposition the elastic modulus was determined to be 20 MPa[13], however the elastic modulus of a turf comprising of 15 vertically aligned and well spaced CNT Turfs has been measured to be in the range of 0.91-1.23 TPa[14]. The major factor causing the change in mechanical behavior and properties in the case of interconnected CNT Turfs, is the tube-tube interaction resulting from the existence of weak, short range van der Waals bonding[15]. Thermal conductivity

of a turf dropped to as low 74 W/m K[16] possibly due to lateral heat transfer along the tube-tube interconnection within the turf.

This chapter focuses on the general mechanical properties of carbon nanotube turfs grown by chemical vapor deposition. The elastic response and hardness were measured directly from the unloading slopes of several nanoindents performed on the turfs, while the onset of plastic deformation was determined by analyzing several nanoindents at varying maximum applied loads. Adhesive forces between carbon nanotubes and the diamond tip were quantified under nanoindentation and compared to those occurring under nanoindentation of gold coated turfs. Adhesion forces resulting from elastic spherical indents agreed with the JKR pull-off load predictions.

4.3 Experimental Procedure

Carbon nanotubes were grown by chemical vapor deposition on substrates suitable for photolithographic pattering. This method uses iron particles which precipitate from a silicon oxide based sol-gel solution spun on a silicon wafer. The sol-gel solution was prepared with10 ml of ethanol, 10 ml of TEOS, 4.36 g of iron nitrate $Fe(NO_3)_3$, 15 ml of H2O, and 2 drops of nitric acid HNO_3. Ethanol and the TEOS solution were first mixed for 15 minutes at room temperature. A solution of 4.36 g of iron nitrate $Fe(NO_3)_3$ diluted in 15 ml of H_20 was then added to the ethanol-TEOS solution, and the solution was stirred considerably for 20 minutes. Finally, 2 drops of nitric acid HNO_3 were added to the solution, which was then stirred for an extra 15 minutes. The resulting sol-gel solution was then aged for 24 hours at room temperature prior to any use.

A 75 mm diameter polished silicon wafer was used as a substrate for carbon nanotube growth. After cleaning and removing the native oxide through a wet buffered oxide etch step, wafers were rinsed and dried prior to deposition of 3 ml of the previously aged sol-gel solution, which was filtered through a 0.2 μm syringe to remove any precipitates. The sol-gel was deposited by spin coating at 3000 rpm for 30 seconds, resulting in a sol-gel layer thickness of 500 nm[17]. The wafer was then dried for 24 hours at a temperature of 80ºC. Photolithography was carried out on the aged film, resulting in a pattern of 300 μm diameter dots onto which CNTs were grown by a chemical vapor deposition technique as described earlier. By varying the growth time and conditions, the resulting samples consisted of vertically aligned CNT turfs with a 300 μm diameter and heights ranging from approximately 2 to 200 μm.

Typical nanoindentation experiments, shown in Figure 4.1 (conducted on single crystal tungsten and silicon respectively) were performed on the CNT turfs using a Hysitron Triboscope in conjunction with a Park Scientific Autoprobe CP scanning probe microscope. Two types of tips were utilized for these experiments. The first was a diamond tip with a Berkovich geometry. This tip is relatively blunt, and has an effective tip radius of 1078 nm. The second tip was a 60º included angle conical diamond indenter tip, with a effective tip radius of approximately 15 μm. This tip was used both as a diamond tip, and subsequently coated with approximately 30 nm of gold. Most indentations followed a loading schedule that consists of a loading segment at a constant loading rate, followed by a hold segment, then an 80% unloading followed by a short hold segment and a complete unloading. The drift rate was calculated and corrected for at the beginning of each indent. The maximum applied load varied between 10 and 500 μN.

The CNT turfs were tested in the ambient laboratory environment (approximately 20ºC and 40% relative humidity). One set of samples was coated with 300 nm of gold using DC magnetron sputtering to reduce the tube-diamond tip adhesion effects. As observed under the scanning electron microscope, the 300 nm gold layer covered tubes individually rather than grouping a cluster of adjacent tubes together. Nanoindentations were also conducted on tungsten W and silicon Si samples for results comparison.

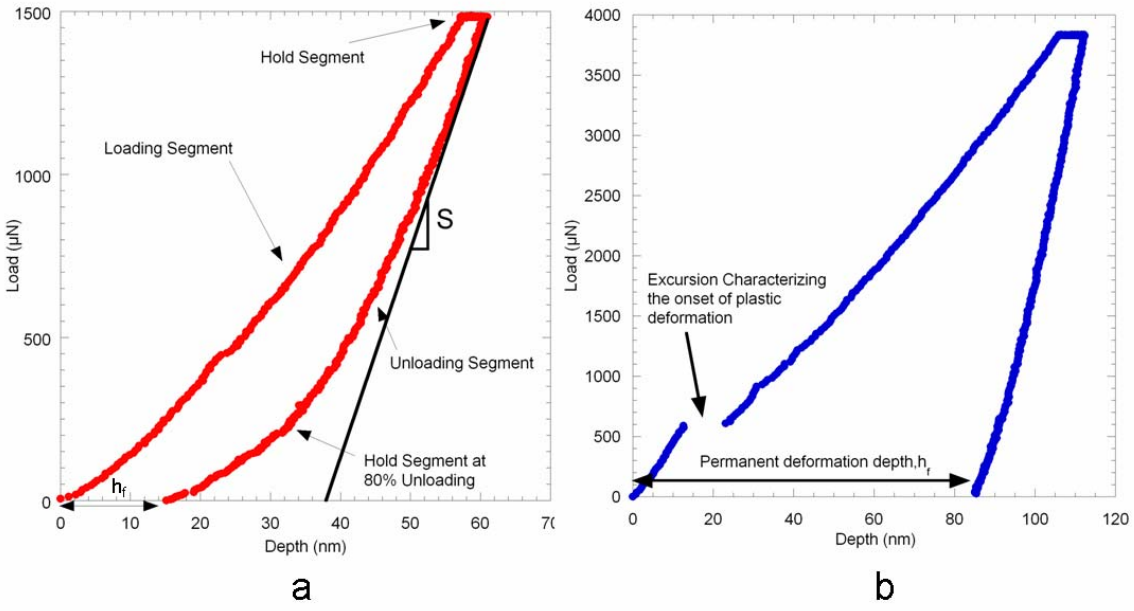

Figure 4.1 Typical indentation load-depth curves of W and Si. a. Typical Si indents, constituting of a load segment, followed by a hold at the peak load, then an unloading segment with a short hold period used to calculate the drift rate. Indent and material properties can be easily extracted particularly the unloading slope and the power fit of the upper portion of the unloading segment used to calculate E_r and H, and the final depth h_f. **b.** An indent in W, revealing an excursion characterizing the onset of plastic deformation.

4.4 Results

The onset of permanent deformation during nanoindentation with tips which have a contact that is initially spherical can be monitored either through distinct yield points (such as the case in low dislocation density single crystals [18- 22]) or through a more graduate deviation from elastic loading[23] . From monitoring the load and depth during the indentation (either from an unloading slope analysis[24] or an oscillatory loading sequence often referred to as the continuous stiffness method. However, in the case of CNT turfs, measuring the onset of permanent deformation is more complicated, due to the compliance of the turf, and the fact that the material deforms in a non-linear elastic mode[13,10].

Figure 4.2 shows a typical load-depth curve of an indentation conducted on a CNT turf. Although the same loading schedule was used as the one for the indentations shown in figure 4.1, several characteristics differentiate CNT indents from traditional indentations in metals or semiconductors. However, before attempting to explain the load-depth curve in detail, an illustration of the way the indenter operates would be useful. The indenter tip is held by springs located within a triple plate capacitor as shown in the inset of figure 4.2. To produce an indent a voltage is applied between the plates which causes the springs to deflect downward. Measuring the change in capacitance on the other set of capacitors allows for monitoring the displacement. Through calibrations of the spring constants, the load applied to the sample is determined by subtracting the force carried by the springs at a given displacement from the applied load. In our current system, we define a pre-load of approximately 1-3 μN, which means the tip is in contact with the turf at the start of the test.

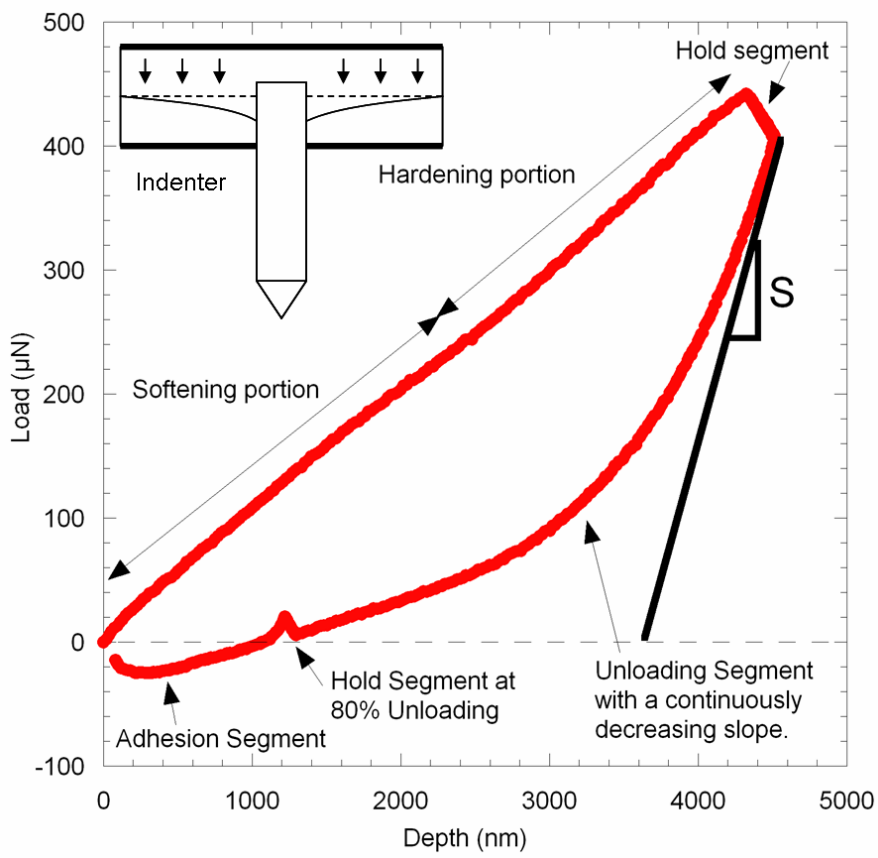

Figure 4.2 A typical load-depth curve of a carbon nanotube turf. The loading segment of the curve was characterized by an inflection point that changed the segment from having a slight negative curvature, to having a slight positive curvature. The loading segment was followed by a hold segment then an unloading segment from which the properties of the turf were calculated. The lower portion of the unloading segment crossed the depth axis and dropped to negative loads, as a result of CNT adhering to the tip. Inset: an illustration of the Hysitron tip deflected under applied voltage to produce an indent. The dotted line is the initial spring location prior to deflection.

As the indentation proceeds, two things impact the "mechanical fingerprint"[25] of the resulting indentation. The indenter shape changes from effectively spherical to

pyramidal (or conical). Knowing the tip radius of the Berkovich tip from elastic indentations in W, the critical distance h* at which the tip transitions from spherical to a self similar shape is approximately

$$\frac{h^*}{R} = 1 - \sin\theta \quad [26] \qquad (5)$$

where θ is the semi apical angle (for a Berkovich tip this is 70.3º), and so for figure 4.2 this critical height h* is 79 nm. The self similar shape of a pyramid leads to the familiar loading curves shown in figure 4.1, which are concave due to an increasing area of contact at increasing depths. As is clear in figure 4.2, indentations into CNT turfs do not exhibit this type of loading curve.

However, for any normal indentation the properties of interest will be defined by the interactions of CNTs with the tip and with each other. As loading increases between the tip and the sample, there are several possible mechanisms for deformation. First, tubes which are in contact with the tip can bow. Initially as the tip contacted the turf and the loading increased, it is likely that tubes in contact with one another were slid downward due to the weak van der Waals bonding between neighboring tubes, resulting in a softening effect, as was seen from the negative curvature of the lower portion of the loading segment. However, the curve reaches an inflection point beyond which the turf ceased softening, which could be a result of an increase in contact area. But in a turf like material this behavior could also be the result of an increase in the tube density engaging with the tip as the applied load is increased.

The loading segment was then followed by hold segment which shows a significant creep. The creep was the result of the constant applied voltage to the plate. As the sample creeps, the increased displacement results in a lower applied load to the turf

due to the load carried by the support springs**.** Another way to explain this, is that while the system applies a constant load, the tip is brought downward due to the fact that the tubes in contact are thermally activated and sliding along each other. This increases the spring force, and thus reduces the load applied on the turf (which is the difference between the constant applied load and the increasing spring force). Creep may be observed in all materials, but its effect is magnified in CNT turfs due to their compliance. The unloading segment was characterized by a sharp initial slope which quickly decayed. Strong adhesive forces between and the diamond tip caused a negative unloading portion. The indent output load is measured as the difference between the load applied on the turf and the load resulting from the spring deflection multiplied by it spring constant. As the load applied on the sample decreased, the tip remained deflected downward due to adhesive forces, thus holding a constant spring force. As soon as the decreasing applied load passed the value of the spring force, a negative load was recorded. Being strictly the result of CNT adhering to the tip, the minimum load reached within the negative portion of the unloading segment was taken to be the maximum adhesive force that occurred between CNT and the diamond tip.

Elastic properties, including the reduced modulus E_r and the hardness H defined as the maximum applied load over the projected contact area were determined knowing the initial unloading slope (determined from a power law curve fit of the upper portion of the unloading segment of each indent) as well as the area function of the pyramidal tip $A(h)$ (determined experimentally) and using the following equations:

$$H = \frac{P_{max}}{A}, \qquad (1)$$

And

$$E_r = \frac{\sqrt{\pi}}{2}\frac{1/C_s}{\sqrt{A}} \qquad (2)$$

Where Pmax is the maximum applied load, *A* is the contact area at the given load, and *S* is the initial unloading slope, which allows calculation of the sample compliance, C_s, by

$$\frac{1}{S} = C = C_f + C_s \qquad (3)$$

where C_f is the frame compliance, which is small in this experiment compared to C_s. Knowing the diamond's elastic modulus and Poisson's ratio to be E_d=1249 GPa, and ν_d=0.07 respectively, and assuming that CNT turfs behave as foamlike materials[27] thus possessing a Poisson's ratio ν=0, the turf's elastic modulus E was therefore deduced as follows:

$$\frac{1}{E_r} = \frac{1-\nu_d^{\,2}}{E_d} + \frac{1-\nu^2}{E} \qquad (4)$$

Using the load-depth curves of 20 indents the elastic modulus of the turf was measured to be 14.9 MPa, with a standard deviation of 5.7 MPa, and the hardness was measured to be 5.5 MPa.

The effect of the adhesive forces was reduced by conducting indents on CNT turfs with 300 nm gold, gold being a material that is relatively non adhesive to diamond. Figure 4.3 compares an indent conducted on a bare CNT turf to one conducted on an Au coated CNT turf. The indent on the bare turf, although having a lower maximum applied load caused almost an order of magnitude higher adhesive forces. Au sputtering greatly affected the general mechanical properties and behavior of CNT turfs, clearly noticeable when comparing the resulting load-depth curves in Au coated turfs. Indents softened, which could be attributed to the Au coating eliminating the van der Waals bonding that

existed between neighboring tubes, which, although easily breakable under applied pressure or temperature, played a significant role in hardening the turfs. The initial unloading slope of the indent was also reduced which reduced the values of the measured elastic modulus and hardness becoming 4.2 MPa with a standard deviation of 2.6 MPa and 2.01 MPa respectively. These measurements were the average of the results extracted from the load-depth curves of 20 indents.

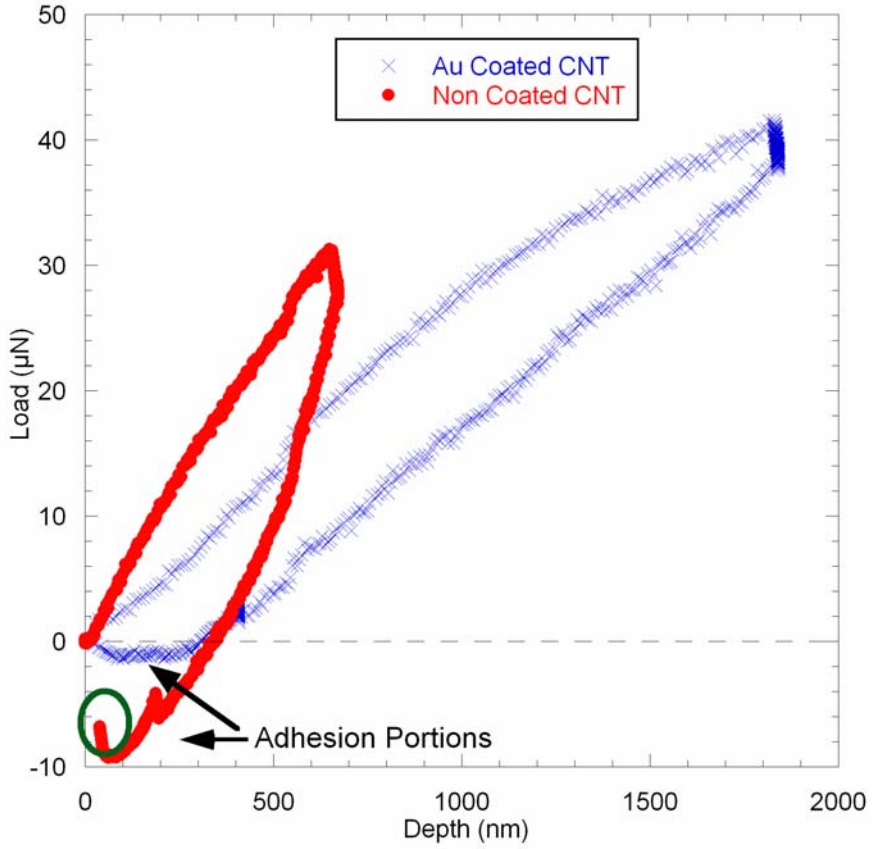

Figure 4.3 Effect of a 300 nm gold sputtered layer on CNT turfs. Resulting load-depth curve revealed that the turf softened relatively to the non coated turf. An indent on an Au coated turf, with a higher maximum applied load resulted in a smaller adhesive load when compared to an indent conducted on non coated turfs with a smaller maximum applied load.

The unloading segment reached a minimum (the maximum adhesive force), prior to a load increase at a constant slope as shown in figures 4.2 and 4.3. In order to determine the onset of plastic deformation of the turf under nanoindentation, the lower linear portion of the unloading segment circled in figure 4.3 was fit to a linear relationship, and the resulting intercept between the curve fit and the depth axis was determined. For an indent to be defined as completely reversible (elastic), the curve fit had to intercept the depth axis at its origin. This procedure was applied to several indents at increasing maximum applied loads, and the onset of plastic deformation was determined to be the maximum applied load of the indent that showed the first deviation from the depth axis origin. Figure 4.4 shows the variation of the x axis intercept of several indents with respect to the maximum applied loads, for both non-coated and Au coated CNT indents. The plot revealed that the onset of permanent deformation occurred at load of 45 μm in case of the non-coated CNT indents. However no onset of permanent deformation was measured in the case of Au coated CNT, which suggested full reversibility once the applied was released.

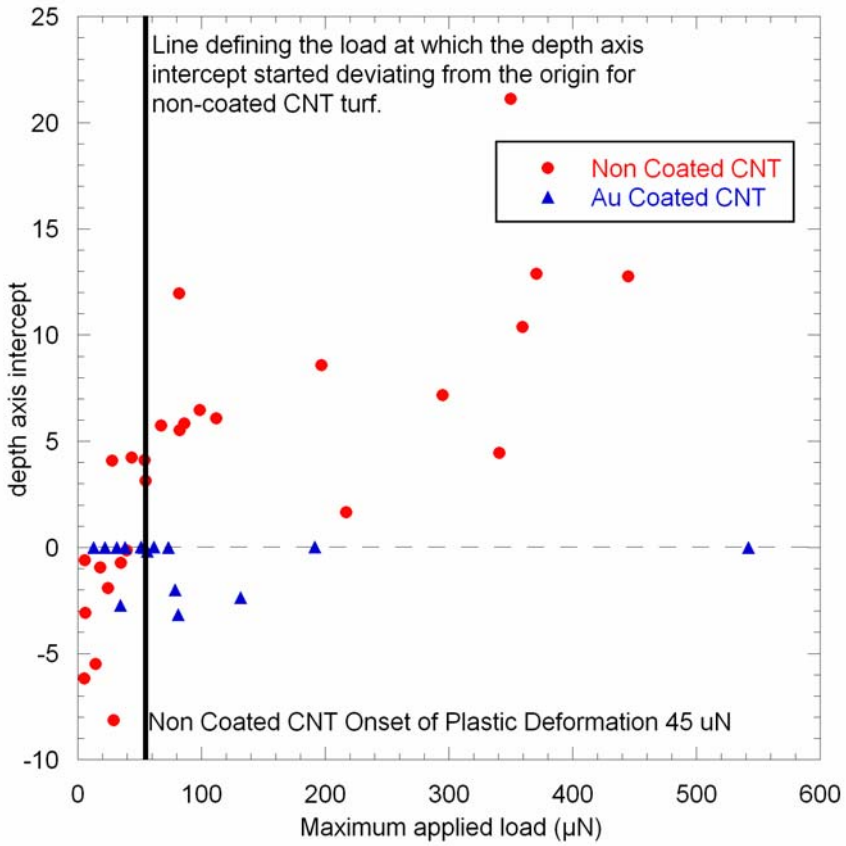

Figure 4.4 Onset of Permanent Deformation. Interception points between the linear curve fit of the lower power of the unloading segment and the depth were plotted as a function of their respective maximum applied load for both Au coated and non-coated indents. The onset of permanent deformation was taken as the load at which the interception points started deviating from the origin. The onset of permanent deformation was found to be 45 μN in case of the non-coated turfs. However the Au coated turf did not undergo permanent deformation.

Finally it was noted that indents conducted on CNT turfs proved to be highly reproducible with consisting loading segments and initial unloading slopes, while indents conducted on Au coated CNT showed more variability in their shapes, and slight

variation in their initial unloading slopes. Figure 4.5 shows three indents performed in CNT turfs at varying maximum applied loads.

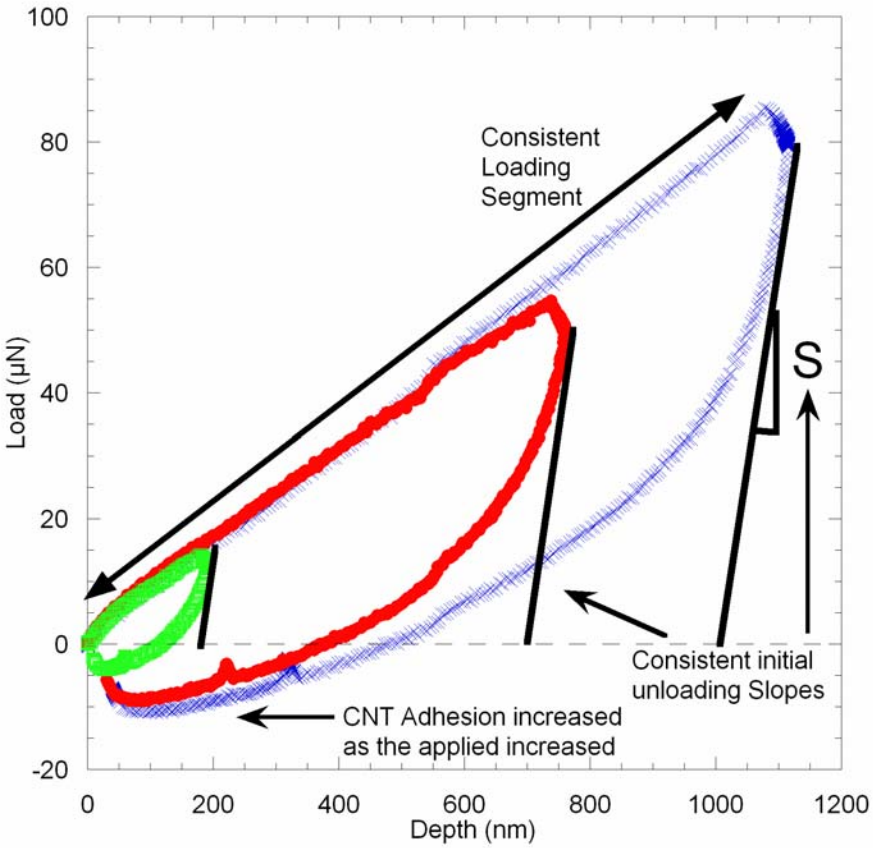

Figure 4.5 Consistency in nanoindentation results. Load-depth curves of three CNT indents were conducted with increasing loads. The overlapping loading segments demonstrated the consistency in nanoindentation results, and suggested a similar tube density and morphology on the surface of a turf. Slopes of the instantaneous unloading were consistent thus resulting in similar E_r and H measurements. Also the maximum adhesive portion increased as the maximum applied load increased.

Three indents performed in gold coated turfs are shown on figure 4.6.

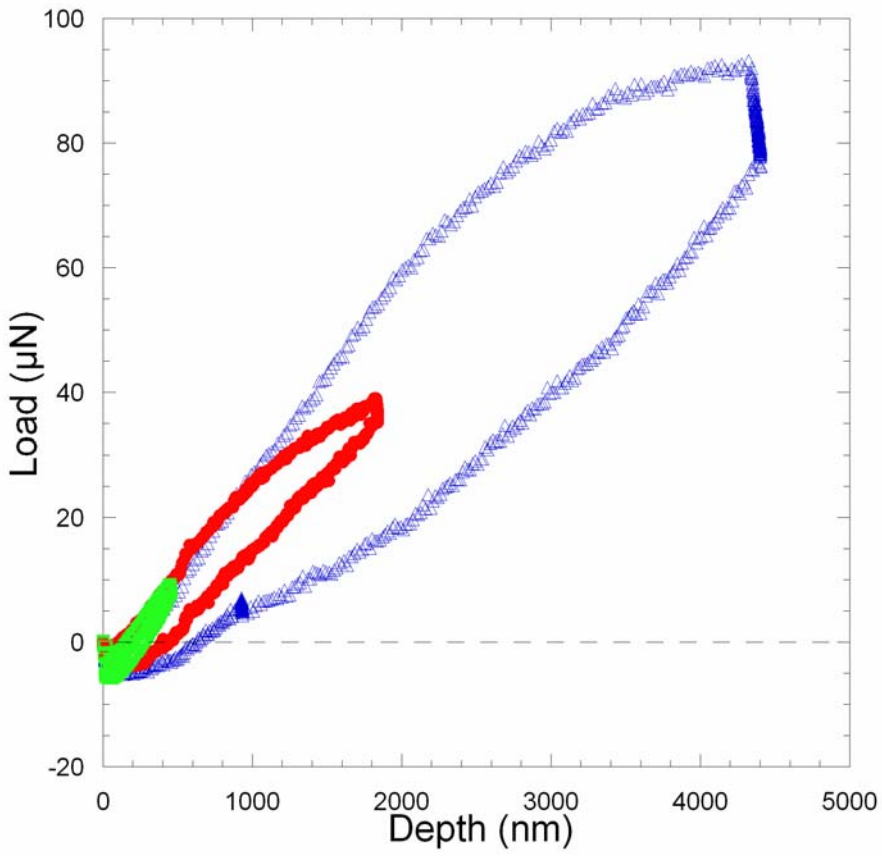

Figure 4.6 Indents in Au coated CNT turfs. Three load-depth curves of indents on Au coated turfs. Slight discrepancies between the curves might be the result of an uneven gold sputtering across the surface.

4.5 Discussion

Load-depth curves of purely elastic indents (crossing the depth axis at 0) have shown signs of energy dissipation, as the unloading segment did not overlap with the loading segment. The bending strain energy of CNTs under applied strain energy increases, however as the load is released, the tubes may spring back, which could account for the loss in energy.

The softening of indents conducted on Au coated CNT turfs was not intuitive as it was expected that depositing a harder material over a softer substrate would have a hardening effect on the general behavior. However, the Au-coated CNT showed the opposite behavior. Observing the Au coated CNT turfs under the SEM revealed that the gold layer, coated single tubes individually rather creating a 300 nm gold layer at the top. Figure 4.7 shows two SEM images that of a bare CNT turf compared to an Au-coated CNT turf.

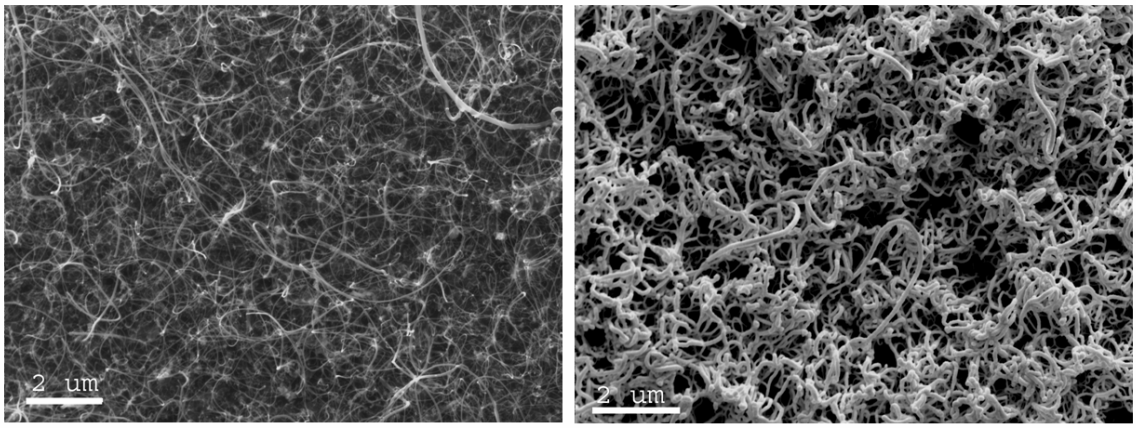

Figure 4.7 SEM images of bare CNT turf vs. Au-coated CNT turfs. a. Top view of a bare CNT turf. b. Top view of an Au-coated CNT turf

This coating still reduced the adhesive forces felt by the tip in contact, and also decreased the van der Waals bonding present between adjacent tubes. These weak bonds had a restraining effect on the turf causing adjacent tubes to slide along each other under an applied pressure, as opposed to free motion in 3D. Hence, once these bonds were reduced

as a result of the gold coating, the tubes were free to move in 3D space, which resulted in a softer turf.

The consistency in the loading segments of the non coated CNT indents proved to be a turf property, since indents conducted on other turfs grown at a different time and using a different sol-gel solution, showed consistent loading segments with a different slope than the indents shown in figure 4.5 as was discussed in Chapter 3. This suggested that the indentation loading slope is highly dependent on the growth characteristic of the turfs, including tube density within the turf, and their morphologies. However the slight inconsistencies seen in case of the Au coated CNT indents (figure 4.6) could be the result of an inconsistent gold sputtering across the surface which resulted in thickness variation across the surface but also in some non coated tubes still capable of chemically adhering to the tip and engaging in van der Waals bonding with neighboring non-coated tubes, which changed the turf properties dramatically. Also, since gold sputtering covered the first 300 nm of the turf, an increase applied load causing an increase in contact depth exceeding 300 nm would increase the number of uncoated tube segments that engaged with the tip thus affecting the load-depth curves and the general elastic results that were extracted.

Hardening within the loading segments occurred at loads that were two orders of magnitude higher than the onset of plastic deformation. If the onset of permanent deformation was to be explained in terms of a strictly mechanical locking mechanism that occurred due the increase in the number of tubes in contact with the tip and the increase of their tortuoasities relatively to their initial growth morphology, then hardening must

have been the result of densification of the turf under the tip as the applied load increased particularly in the localized locking region.

Based on the previous observations and results, a possible qualitative description of the mechanical behavior of CNT turfs under applied compressive loading will now be presented. Figure 4.8 is an illustration of the general mechanical behavior of the turf. The full lines (red lines) defined the tubes that were in contact with the tip, the dash-dotted lines (green lines) represented the tubes that were within the contact area of the tip and would engage in contact if the tip is further loaded, while the dashed lines (blue lines) represented tube that were adjacent to the engaging tubes, but would never get in direct contact with the loaded tip. Figure 4.8b is an SEM image of a close up view of the top of a 300 μm diameter turf, revealing the turf's initial surface morphology; while figure 4.8c is an SEM image of the side of the 300 μm diameter vertically aligned turf.

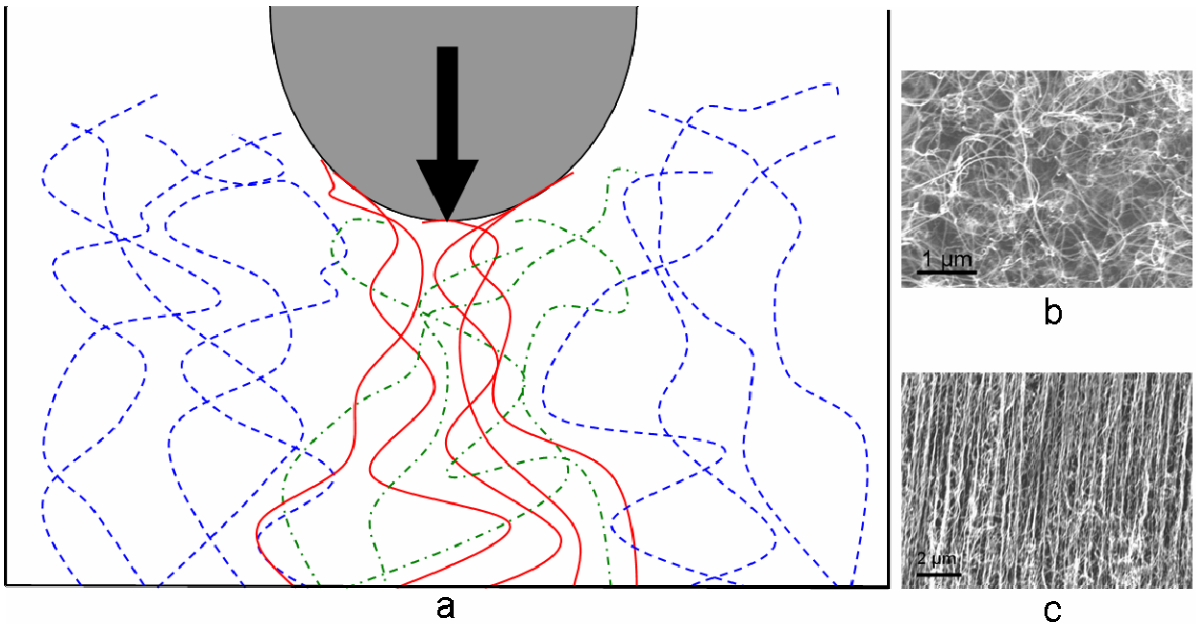

Figure 4.8 Turf behavior under nanoindentation. a. A schematic of turf under nanoindentation. The full (red) lines represent carbon nanotubes that are already in contact, dash-dotted (green) lines represent tube that may engage with the tip under increasingly applied load and depth, and the dashed (blue) lines represent tube that are away from the tip's contact region but are mechanically interconnected or chemically bonded (with weak Van Der Waals bonding), with tubes within the tip's contact region. As the applied load increased, the tubes in contact were pushed down, and their turtuoasity increased. Once a critical depth h_{max} was reached at a critical applied load P_{max}, the tubes in contact mechanically locked with adjacent tubes, and thus causing a permanent deformation in the turf. **b.** An SEM image of the turf's surface. **c.** An SEM image of the turf's side.

As the applied load increases, the tubes initially in contact were pushed further downward while sliding along adjacent CNT tubes, and their tortuoasities increased with respect to their initial morphologies. Also as the contact depth increased, more tubes

engaged with the tip thus densifying the contact area and complicating the change in morphology. Once the critical load and depth values were reached, the tubes with increasing tortuoasities mechanically locked with each other as well as with the adjacent CNTs, thus causing the onset of permanent deformation. As the applied load further increased, the engaged number of tubes was high enough to densify the localized locking region which also aligned the tubes laterally so that they bonded along a whole tube segment rather than a junction which caused the turf to harden under applied loading. Once the tip was removed several tubes were detached from their substrate and adhered to the tip, a behavior worthy of more investigation.

The onset of plastic deformation may also be explained in terms of the total energy of the portion of the turf under applied loading E defined as the difference between the strain energy resulting from CNT segment bending, U, and the contact energy resulting from tube-tube interaction, Γ. It is likely that the onset of plastic deformation occurs when the strain energy is exceeded by the contact energy due to an increase in the density of CNT segments contacting adjacent segments. The absolute minimum is defined when all the tubes contact their adjacent tubes along the total length of the turf, thus minimizing the turf's total energy.

To better understand the adhesive behavior of carbon nanotubes and the diamond tip, the maximum adhesive loads or pull-off loads were extracted from the load depth curves as discussed earlier and were plotted against their respective maximum applied load, for both non-coated CNT and Au coated CNT as shown in figure 4.9.

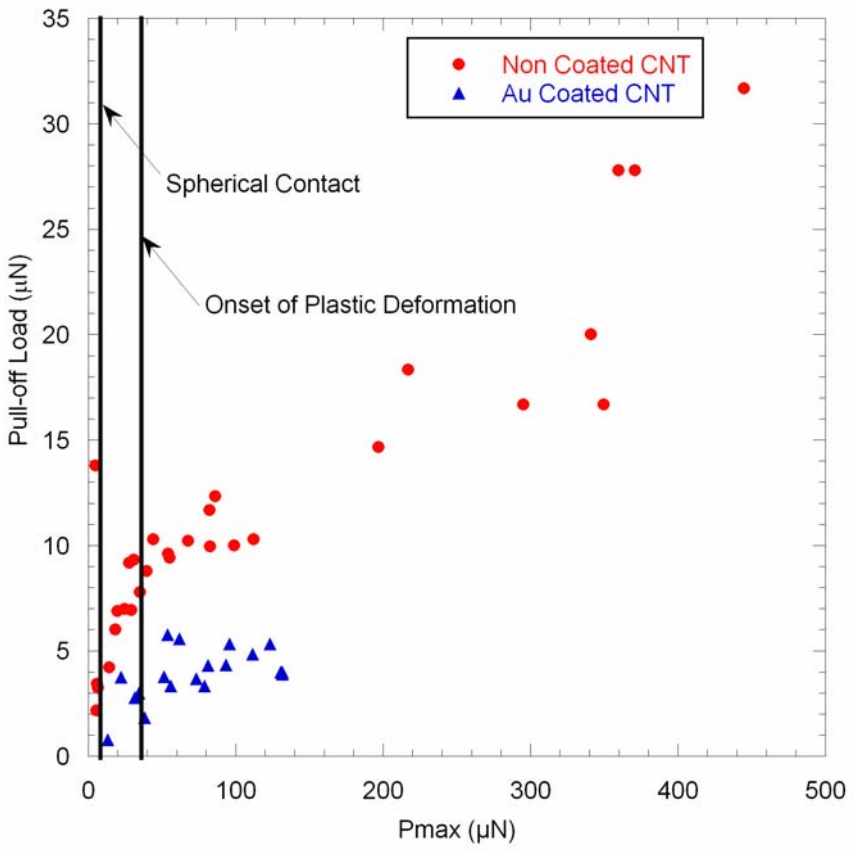

Figure 4.9 CNT Adhesion to indenter tip. Pull-off load or maximum adhesive force extracted from nanoindentation load-depth curves were plotted against the respective maximum applied loads of each indent, for both non-coated and Au coated CNT turfs. A line defining the transition from a spherical contact to a conical contact and another line defining the onset of plastic deformation were drawn at their respective loads.

The general trend revealed that non-coated CNT showed higher adhesive loads when compared to those resulting from indents in Au coated CNT. The adhesive loads in case of Au coated CNT seemed to stabilize at a value of 5 μN. Since Au is a non adhesive material, it was expected that no adhesive forces would be measured. One possible way to explain the presence of low adhesive force measurements is by accounting for the fact

that gold coating the turf is not perfect and thus some CNT segments were left uncoated. The number of these bare segments increased as the indentation depth increased as only a 300 nm layer was applied. This conclusion was supported by the fact that adhesive forces close to 0 were measured at low loads and contact depth of around 500 nm (lower than 20 μN, as shown on figure 4.10 below). On the other hand, the adhesive loads in case of bare CNTs increase with respect to the maximum applied load. The onset of plastic deformation coincides at the transition between the rapidly increasing adhesion values to a linear relationship fashion with respect to the maximum applied load. Another distinction had to be made knowing that the tip shape can be assumed to initially be a blunt sphere with a radius R of 1078 nm, and then transitioned to a conical shape, which would highly affect the adhesive loads. A line across the load corresponding to a contact of 79 nm is marked in figure 4.9. The elastic spherical region was thus the only region for which a model was developed to predict its adhesive properties. The JKR model[28] which predicts adhesive forces between two elastic spheres was used as a model to predict the adhesive forces in spherical elastic contact zone. The adhesive forces were

$$P_{Adh} = -\frac{3}{2}\gamma\pi R \qquad (6)$$

Where R was calculated knowing the radii of the tip R_1 and the turf R_2 (taken to be infinity):

$$R = \frac{R_1 R_2}{R_1 + R_2} = R_1 \qquad (7),$$

And γ is the surface energy between the diamond tip and the turf.

The surface energy was calculated by integrating the Leonard-Jones interplanar model while assuming the properties of a graphitic contact since both CNT and diamond are carbon based

$$\mathrm{P}(\alpha)=\frac{\psi}{6}\left[\left(\frac{d_0}{\alpha}\right)^{10}-\left(\frac{d_0}{\alpha}\right)^{4}\right] \qquad (8).$$

Where d_0 is the equilibrium distance for carbon measured to be 0.34 nm, ψ is the compressional elastic constant measured to be 36.5 GPa, and α is the interlayer distance[29]. The surface energy was then calculated to be :

$$\gamma=\int_{0.34}^{\infty}P(\alpha)d\alpha=-0.46\frac{J}{m^2} \qquad (9)$$

The adhesive forces in the spherical elastic region were therefore predicted to be 2.33 μN. Leaving the obvious outlier out, the data within the spherical elastic region matched the predicted results very well as was shown on figure 4.9. The adhesive forces were also plotted with respect to the maximum contact depth, and the corresponding contact depth at which the onset of permanent deformation occurred was determined to be roughly 1000 nm as shown in figure 4.10.

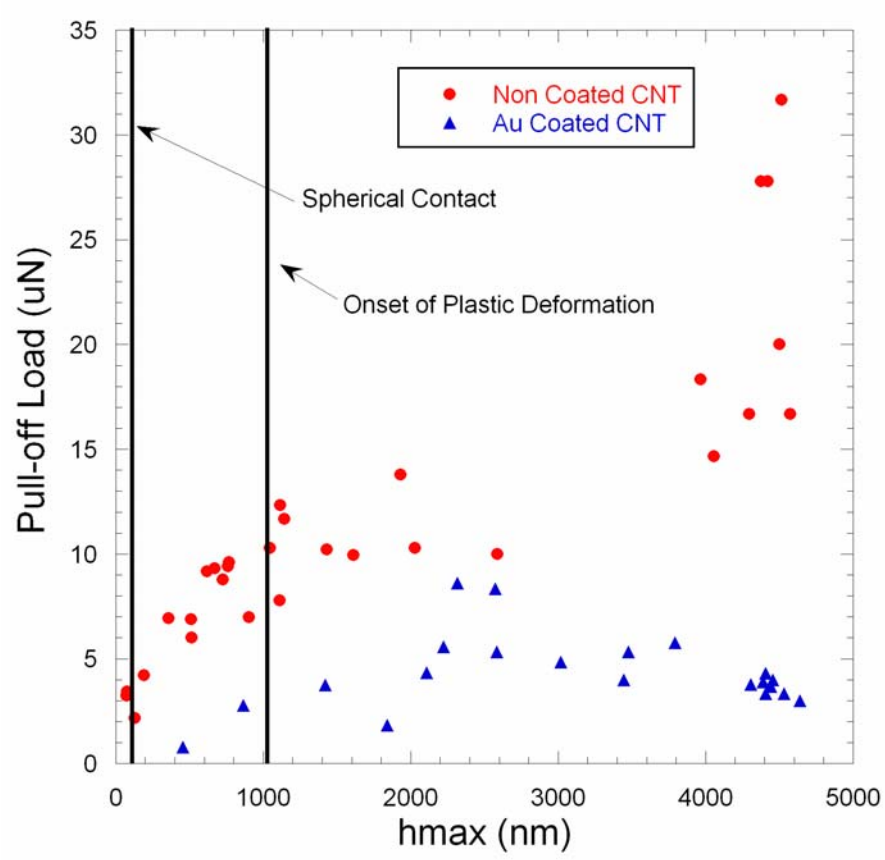

Figure 4.10 Pull-off load as a function of the maximum indentation depth.

A critical load and depth at which the onset of permanent deformation occurred were thus determined. A region within which deformation are purely elastic was therefore estimated as is shown on figure 4.11 which is a plot of the maximum applied load as a function of the maximum contact depth. A smaller region within which a spherical elastic contact occurred was defined as well on the plot.

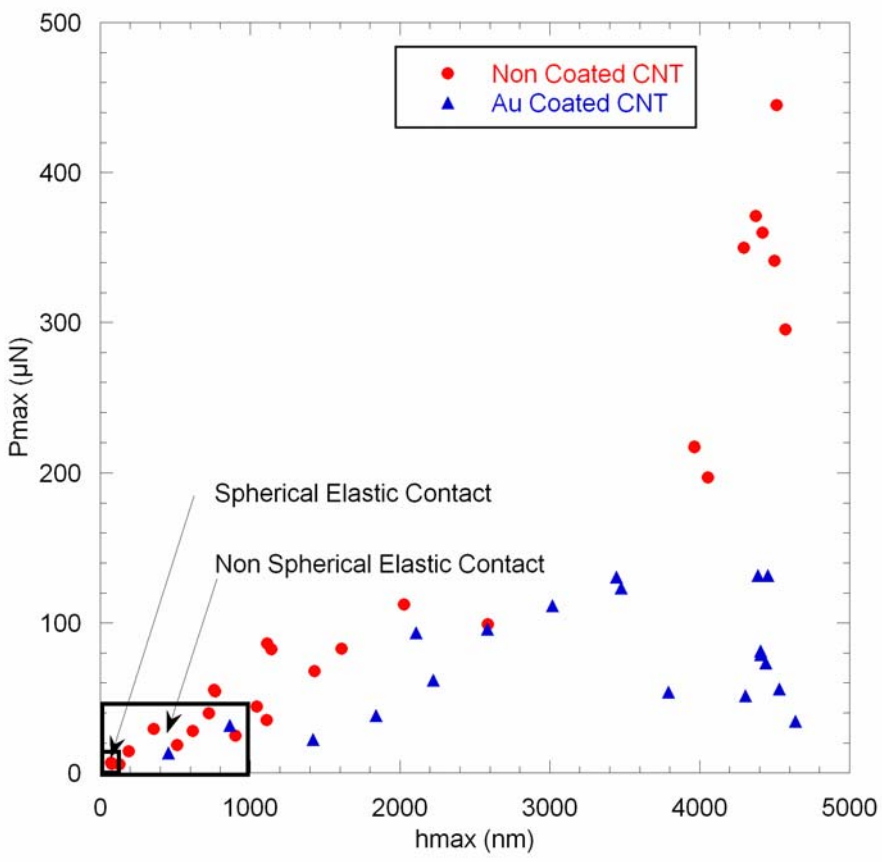

Figure 4.11 Elastic and plastic region estimation for non-coated and Au coated CNT. The maximum applied load of each performed indent plotted against the respective maximum indentation depth. Regions bordered by critical maximum indentation depth and maximum applied load defined the transition between a spherical elastic contact to a conical elastic contact, as well as the transition between the elastic deformation region and the plastic or permanent deformation region.

Based on the previous observations, it was noted that the adhesive forces between carbon nanotubes and the diamond pyramidal tip, highly affected the shape of the resulting load-depth, particularly the initial unloading slope. Prior to analyzing the consequences of the adhesive forces on the measured properties, an understanding of the

turf mechanical behavior under the presence of adhesive forces, followed by an extrapolation to understand their behavior in absence of these forces, is necessary. Figure 4.12 illustrates different possible morphologies of CNT turfs after load removal in presence and absence of adhesive forces for both elastic and permanent deformation.

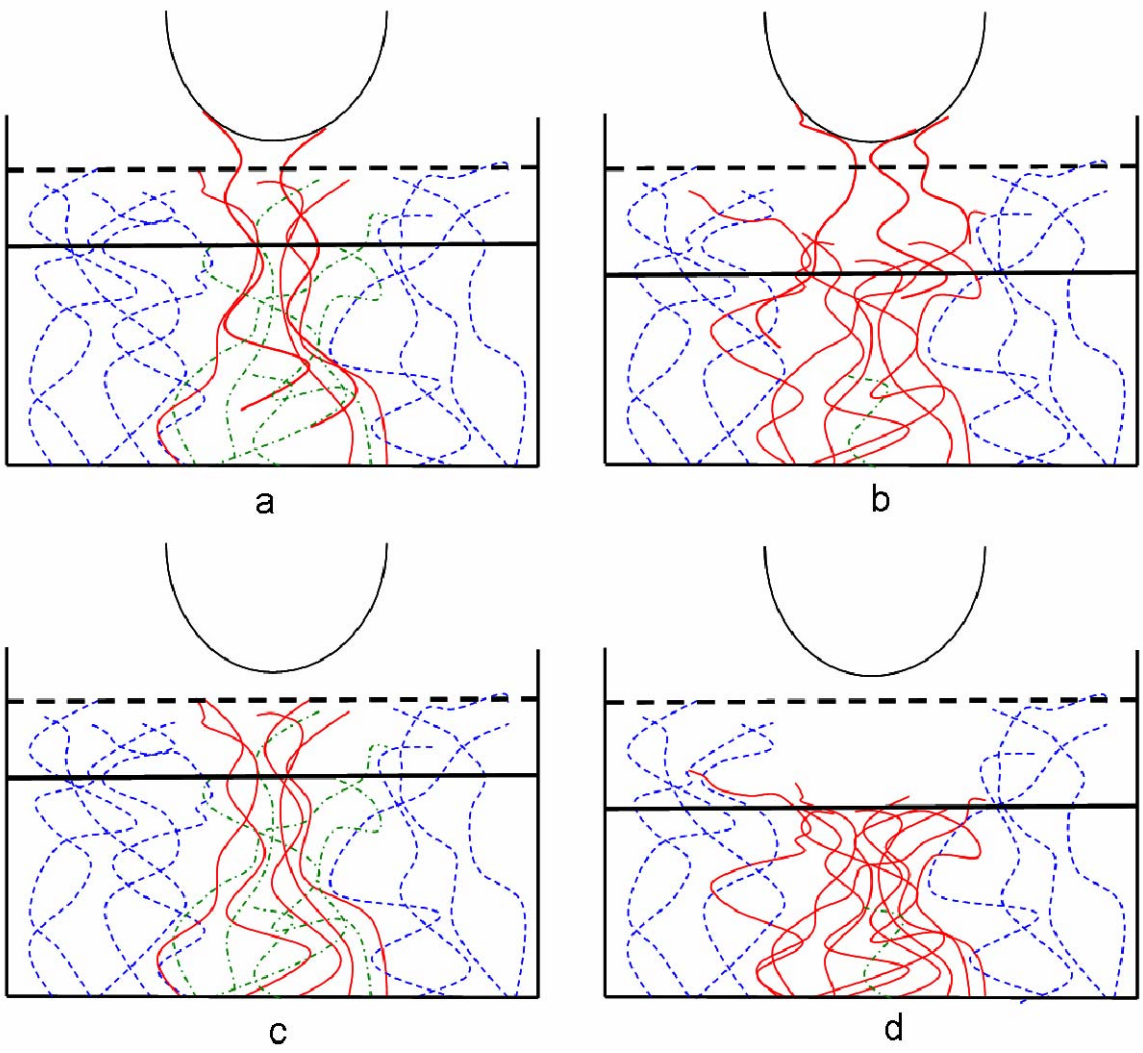

Figure 4.12 CNT turf morphology following load removal in presence and absence of adhesive forces for both elastic and permanent deformation. a. Illustration of the turf morphology after an elastic indent was conducted. The turf was restored to its initial height denoted by a dashed line, after reaching an elastic depth denoted by the full line. Some CNTs exerted enough adhesive force to permanently detach from the substrate and

the turf and stick onto the tip. **b.** Illustration an indentation that reached a plastic load-depth combination. Although it permanently deformed it was still pulled up to an intermediate depth denoted by the dash dotted line due to adhesive forces, with more tubes stuck on the tip. **c.** Illustration of an elastic indent as it would behave hadn't there been any adhesive loads: full recovery and no tubes stuck on the tip. **d.** When a plastic indent is performed with no adhesive forces, the turf permanently deforms and remains at the maximum indentation depth h_{max}.

Figure 4.12a illustrated the morphology of an elastic indent in presence of adhesive forces. The full horizontal line represented the maximum contact depth reached by the indent, while the dotted line represented the initial turf height. Under these elastic conditions, following load removal the turf may fully restore to its initial height, while some CNTs were pulled out from the sol-gel substrate in which they were embedded and permanently adhered to the tip. However when the indent reaches a load-depth combination that caused the locking mechanism or the onset of permanent deformation, more tubes adhered to the tip following load removal. Also although the turf was permanently deformed, the strong adhesive forces may possibly pull the deformed turf under the tip to an intermediate height denoted by a lateral dash-dotted line. The tubes' tortuoasities increases compared to their initial morphologies and more interconnection between the tubes in contact and the adjacent tube caused the locking mechanism to occur. Based on these results, an extrapolation can be made to look at the turf behavior in absence of adhesive forces, which could have been experimentally achieved by coating the tip instead of the turf, with a non adhesive coating chosen carefully so that it does not

affect the hardness of the tip. One possible model explaining the behavior of the turf in absence of adhesive forces is presented next. If an elastic indent were to be conducted under a no adhesion condition, the turf would fully restore back to its initial turf height upon load removal with no tubes stuck on the tip as illustrated in figure 4.12c. However if a plastic load-depth combination was reached, the highly tortuous tubes having mechanically locked with their adjacent tubes, and bonded along the length of the tube would remain at the deformed depth with tubes adhering to the tip as was illustrated in figure 4.12d.

Finally it has been observed that adhesive forces affect the shape of the load-depth curve, while particularly increasing the initial unloading slope. Figure 4.13 showed resulting load-depth curves from indents conducted using the conical shaped record needle prior and post gold coating. Gold coating the tip resulted in a decrease in the adhesive force for any given maximum applied load and it highly affected the general indent shape as well, particularly the unloading portion, which modified the calculated elastic properties. This proved that the presence of adhesive forces lead to apparent elastic properties measurements that were higher than the true properties. Curve fitting the unloading portion of the indents conducted prior and post gold coating using a power fit, and calculating the respective slopes S and S' at the peak loads, showed that the slope decreased by 30 % in absence of adhesive forces.

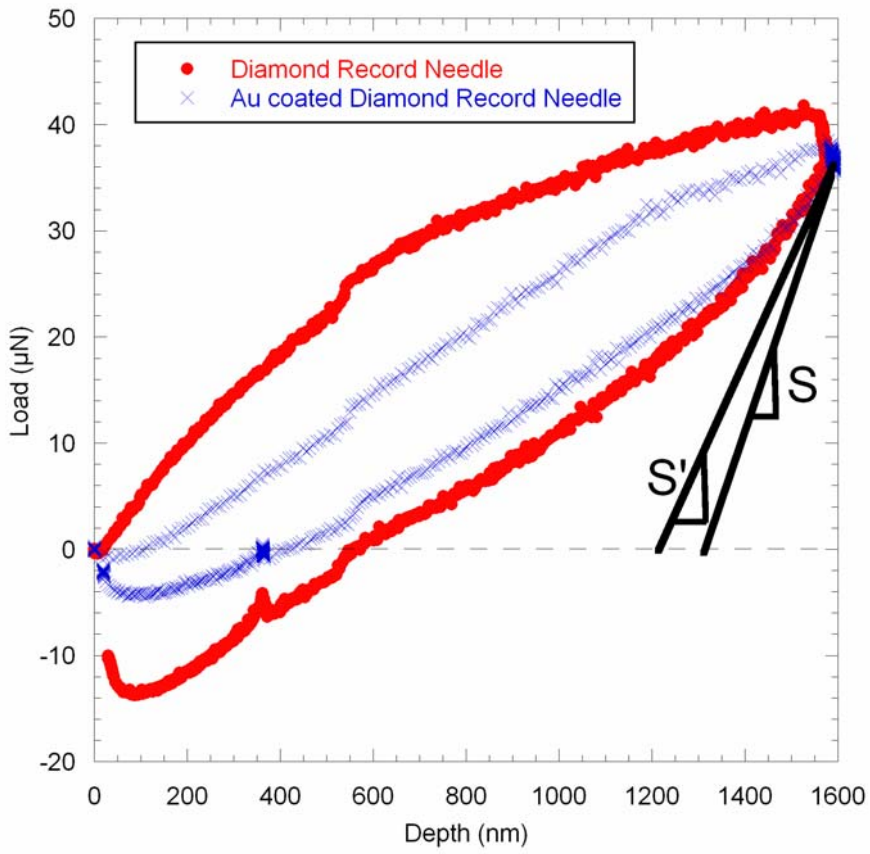

Figure 4.13 Adhesive effects on Indentation load-depth curves. Coating the needle tip with a uniform layer of 30 nm of gold, reduced the measured slope and thus the elastic properties of the turf by 30%.

Adhesive forces resulting from indents conducted using the record needle tip prior and following gold coating were measured from respective sets of load-depth curves. Figure 4.14 is a plot showing how these measurements compared with the bare and the Au coated CNT adhesion to Berkovich tip. A significant reduction in adhesive forces was shown in the presence of an intermediate gold layer, whether that layer was on the turf or on the tip.

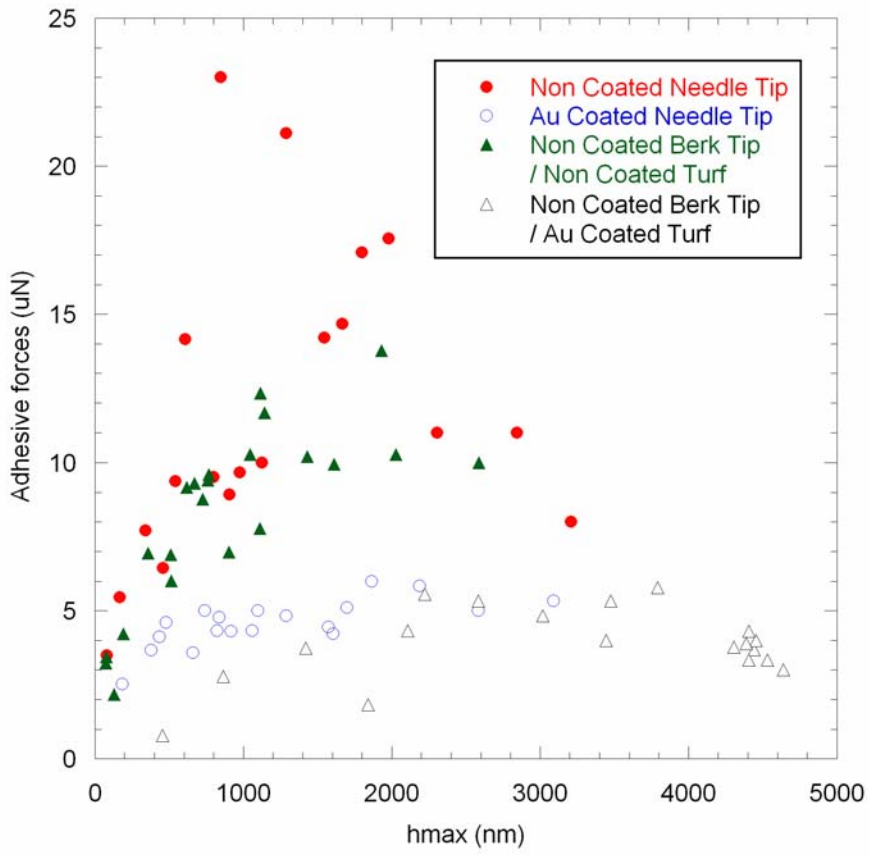

Figure 4.14 Adhesive forces vs. hmax, for all four cases. A 50 % decrease in adhesive forces was observed in the presence of an intermediate gold layer.

4.6 Conclusion

CNT turf properties were measured using nanoindentation and have proven to have different properties than those of a single tube, mainly due to the presence of weak, short range van der Waals bonding that highly affected the mechanical behavior of the turf. The mechanical behavior of the turf under applied loading has been explained, and the onset of permanent deformation has been explained in terms of a locking mechanism dependent on the tubes initial morphologies and growth parameters. Adhesive forces have proven to impact the shape of the load-depth curves, particularly the initial unloading slope, thus affecting the elastic properties measurement. A 30% decrease in the

measured initial unloading slope, and thus in the measured elastic properties, has been shown in absence of adhesive forces. A 50 % decrease in adhesive forces has been observed in the presence of an intermediate gold layer between the tip and the turf.

4.7 References

[1] Iijima, S. Helical microtubules of graphitic carbon. *Nature* **354,** 56-58 (1991).
[2] Iijima, S., & Ichihashi, T. Single-shell carbon nanotubes of 1nm diameter. *Nature* **363,** 603-605 (1993).
[3] Bethune, D. S., Klang, C. H., De Vries, M. S., Gorman, G., Savoy, R., Vasquez, J. & Beyers, R. Cobalt-catalysed growth of carbon nanotubes with single-atomic-layer walls. *Nature* **363,** 605-607 (1993).
[4] Berber, S., Kwon, Y. amd Tomanek D. Unuasually high thermal conductivity of carbon nanotubes. *Phys. Rev. Lett.* **84 (20),** 4613-4616 (2000).
[5] Baughman, R. H., Cui, Ch., Zakhidov, A., Iqbal, Z., Barisci, J., Spinks, G., Wallace, G., Mazzoldi, A., De Rossi, D., Rinzler, A., Jaschinski, O., Roth, S. & Kertesz, M. Carbon nanotube actuators. *Science* **284,** 1340-1344 (1999)
[6] Treacy, M. M. J., Ebbesen, T. W. & Gibson, J. M. Exceptionally high Young.s modulus observed for individual carbon nanotubes. *Nature* **381,** 678-680 (1996).
[7] Baughman, R. H., Zakhidov, A. A. & de Heer, W. A. Carbon nanotubes-the route toward applications. *Science* **297,** 787-792 (2002).
[8] Ball, P. Roll up for the revolution. *Nature* **414,** 142-144 (2001).
[9] Dresselhaus M. S., Dresselhaus G. & Avouris Ph. Carbon nanotubes synthesis, structure, properties and applications. *Springer.* 30-53 (2001)
[10] McCarter, C. M., Bahr, D.F., Richards, R.F., Ricahrds, C.D., McClain, D. & Jiao, J. Integration of Carbon Nanotubes with MEMS through standard photolithographic techniques. *Mater. Sci. Technol.* **3**, 45-52 (2005)
[11] Suhr, J., Koratkar, N., Keblinski, P. & Ajayan, P. Viscoelasticity in carbon nanotube composites. *Nature Materials* **4,** 134-137 (2005).
[12] Dong, L., Jiao, J., Pan C. and Tuggle, D. W. Effects of catalysts on the internal structures of carbon nanotubes and corresponding electron field-emission properties. *Appl. Phys. A* **78,** 9-14 (2004)
[13] Mesarovic, S. Dj., McCarter, C. M., Bahr, D. F., Radhakrishnan, H., Richards, R. F., Richards, C. D., McClain, D. & Jiao, J. Mechanical behavior of a carbon nanotube turf *Scripta Materialia* **56,** 157-160 (2007).
[14] Qi, H. J., Teo, K.B.K., Lau, K.K.S., Boyce, M.C., Milne, W.I., Robertson, J. & Gleason, K.K. Determination of mechanical properties of carbon nanotubes and vertically aligned carbon nanotube forests using nanoindentation. *J. of Mech. & Phys. of Sol.* **51,** 2213-2237 (2003).

[15] Liew, K. M., Wong. C. H. and Tan, M. J. Buckling Properties of carbon nanotube bundles. *App. Phys. Lett.* **87,** 041901-1-3 (2005)
[16] Hu, X, Padilla, A. A., Xu, J.; Fisher, T. S. & Goodson, K. E. Thermal characterization of vertically-oriented carbon nanotubes on silicon. *21st Annual IEEE Semiconductor Thermal Measurement and Management Symposium*, 292-297 (2005)
[17] McCarter, C. M., Richards, R. F., Mesarovic, S. Dj., Richards, C. D., Bahr, D. F., McClain, D. & Jiao, J. Mechanical compliance of photolithographically defined vertically aligned carbon nanotube turf. *J. Mater. Sc.* **21 (23),** 7872-7878 (2006).
[18] Zbib, A. A. & Bahr, D. F. Dislocation nucleation and source activation during nanoindentation yield points. *Met. Trans. A* **38A,** 2249-2255 (2007).
[19] Bahr, D. F., Kramer, D. E. & Gerberich, W. W. Non-linear deformation mechanisms during nanoindentation. *Acta Mater.* **46 (10),** 3605-3617 (1998).
[20] Schuh, C. A., Mason J. K. & Lund A. C. Quantitave insight into dislocation nucleation from high-temperature nanoindetation experiments. *Nature Mater.* **4,** 617-621 (2005).
[21] Minor, A. M., Lilleodden, E. T., Jin, M., Stach, E. A., Chrzan, D. C. & Morris, J. W. Room temperature dislocation plasticity in silicon. *Phil. Mag.* **85,** 323-330 (2005).
[22] Syed Asif, S. A. & Pethica, J. B. Nanoindentation creep of single-crystal tungsten and gallium arsenide. *Phil. Mag. A* **76 (6),** 1105-1118 (1997).
[23] Swadener, J. G., George, E. P. & Pharr, G. M. The correlation of the indentation size effect measured with indenters of various shapes. *J. Mech Phys. Sol.* **50 (4),** 681-694 (2002).
[24] Oliver, W. C. & Pharr G. M. An Improved technique for determining hardness and elastic modulus using load and displacement sensing indentation experiments. *J. Mater. Res.* **7 (6),** 1564-1583 (1992).
[25] Page, T.F. & Hainsworth, S.V. Using nanoindentation techniques for the characterization of coated systems: a critique. *Surf. Coatings Tech* **61,** 201-208 (1993)
[26] Vanlandingham, M. R., Juliano, T. F. & Hagon, M. J. Measuring tip shape for instrumented indentation using atomic force microscopy. *Meas. Sci. Technol.* **16,** 2173-2185 (2005)
[27] Cao, A. Dickrell, P. L., Sawyer, W. G., Ghasemi-Nejhad, M. N. & Ajayan, P. M. Super-compressible foamlike carbon nanotube films. *Science* **310,** 1307-1310 (2005).
[28] Johnson, K. L., Kendall, K. & Roberts, A. D. Surface energy and the contact of elastic solids. *Proc. R. Soc. Lond. A.* **324,** 301-313 (1971)
[29] Zhao, Y. X. & Spain I. L. X-Ray diffraction data for graphite to 20 GPa. *Phys. Rev. B.* **40,** 993-997 (1989).

CHAPTER FIVE

5 BUCKLING AND DEFORMATION OF CARBON NANOTUBE TURFS UNDER APPLIED COMPRESSIVE LOADING

5.1 Abstract

Since the discovery of carbon nanotubes (CNT), many researchers have attempted to measure the mechanical behavior of single carbon nanotubes. However, with the exception of a few special geometries little has been done to understand the mechanical behavior of an assemblage of CNTs. Their properties arise from their complex nano-geometry and van der Waals driven interactions between individual CNT segments. This chapter will report on the coordinated and oriented buckling of CNT turfs under applied compressive loading. We present a micromechanical model describing the coordinated buckling phenomena of CNT turfs. Buckling stresses were found to be highly dependent upon the turf's shear modulus and height and surprisingly independent of its aspect ratio. To verify the results predicted by the model several turfs with heights varying between 25 and 204 μm were buckled under applied compressive loading, and critical compressive values ranging between 4.3 and 0.2 MPa were measured respectively. These intriguing results are expected to affect the design of CNT turfs used in thermal switches applications.

5.2 Introduction

Carbon nanotubes[1-3] (CNT) and their potential applications[4,5] have inspired numerous studies of the mechanical response of individual nanotubes. The mechanical

properties of individual single-walled and multi-walled CNTs have been documented in a wide range of conditions; both experimentally by testing a tube in tension[6], bending[7,8] or compression[9], and theoretically using molecular dynamics[10] and finite element[11] simulations. With the exception of a few special geometries[12], little has been done to understand the collective behavior of CNT structures under contact loading. Of particular interest are CNT turfs – complex structures of intertwined, nominally vertical tubes[13,14] – and their application as contact thermal switches. Their properties arise from their complex nano-geometry and van der Waals driven interactions between individual CNT segments. Additional complexity arises when coordinated alignment and buckling takes place under uniform compressive loads[15]. In earlier communications[16,17], it has been shown that CNT turfs in localized compression exhibit non-linear elastic behavior, with a high initial and a low final tangent elastic modulus. In chapter 4 the mechanical properties and mechanism of deformation of CNT turfs under localized nanoindentation loads (where a small lateral diameter is probed relative to the overall turf structure), with fully reversible deformation were analyzed. In the stress-free state, CNT segments in the turf are pre-buckled/pre-bent, and the resulting bending strain energy is balanced by the contact energy between the tubes[9]. Localized high stresses produce further localized, *uncoordinated* buckling, resulting in reversible deformation. This chapter will focus on the case of a uniform compressive load over a large area of the turf (such as would be required for a contact switch or heat transfer media[18]). Under these loading conditions, *coordinated reorientation* and *coordinated buckling* of the segments in a particular layer of the turf structure takes place. To that end, we (1) present results of experiments designed to measure the relevant mechanical properties and elucidate the coordinated

buckling behavior, and, (2) develop a micromechanical model for coordinated buckling and compare it to the experimental results. The intriguing mechanical response of turf structures provides some surprising results regarding parameters that control permanent deformation and buckling in assemblages of nanostructures.

5.3 Experimental Procedure

Patterns of vertically aligned CNTs were selectively grown upon photolithographically prepared silicon wafers as previously described. The catalyst was formed using a sol-gel solution with a base of 10 ml of ethanol and 10 ml of TEOS. 4.36 g of $Fe(NO_3)_3$ diluted in 15 ml of H_2O was then added to the ethanol-TEOS solution and stirred for 20 minutes, followed by the addition of 2 drops of HNO_3, and the resulting solution was stirred for 15 minutes, and then aged for 24 hours. The native oxide was removed from a polished silicon wafers, and the sol-gel was deposited on the Si wafer, which was then spun at 3000 rpm for 30 seconds and then dried for 24 hours at 80ºC. The film was patterned using standard photolithography techniques. Carbon nanotube turfs were then grown using a previously described chemical vapor deposition technique[19].

Measurement of the tangent elastic modulus of the CNT turfs was performed using a Hysitron Triboscope in conjunction with a Park Scientific Autoprobe CP scanning probe microscope. A Berkovich tip with a tip radius of approximately 1078 nm was used to conduct the experiments. After four indentations in the CNT turf, the diamond tip was cleaned to remove any residual CNTs stuck to the diamond tip due to strong adhesive bonding. The indentation loading sequence included a loading segment, a hold segment, then an 80% unloading loading segment, a small holding segment from

which drift is calculated, and a final unloading segment. The elastic modulus of the turf was determined using Oliver and Pharr's technique.

Two different techniques were used to buckle the CVD grown CNT turfs. Several turfs with a 300 μm diameter and heights varying between 25 and 204 μm were tested using a displacement controlled compression tool that simultaneously recorded displacement with a LVDT and the load from a load cell attached to a spherical steel tip with a diameter of 1.6 mm. The spherical shape accommodates any alignment mismatch between itself and the 300 μm diameter turf being tested. Other turfs were tested in compression using a load controlled MTS Nanoindenter XP, with a flat diamond punch to contact the turf.

5.4 Experimental Observations

CNT Turfs have shown similar deformation patterns under applied compressive loading. However due to the method used to buckle these turfs, and the strain value reached under experiments, most of the turfs were smashed by the tip in contact, and only a few showed the buckled shape of the turfs.

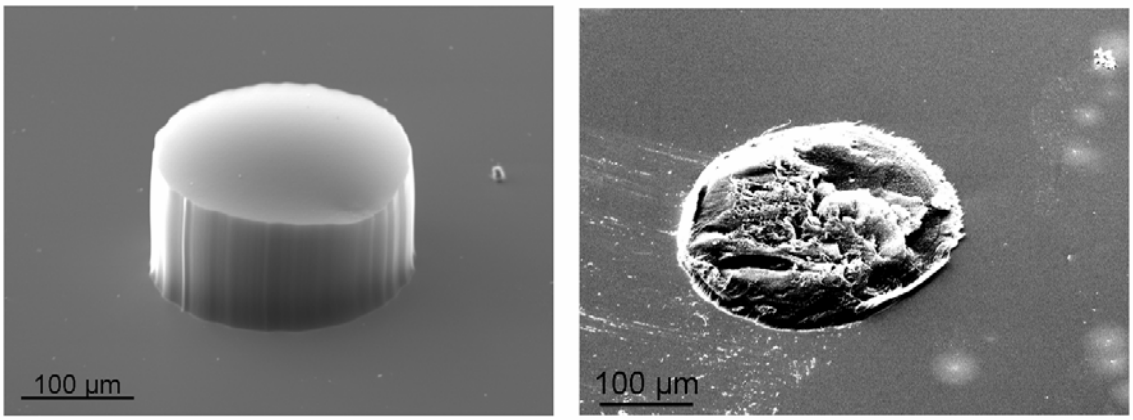

Figure 5.1 SEM image of CNT turf pre and post testing using a standard compression tool.

Figure 5.1 shows two SEM images of a standard CNT turf prior to buckling, and post buckling showing the turf completely smashed due to large applied strain.

However, CNT turfs buckled using an MTS Nanoindenter XP with a flat punch or those buckled under small applied compressive loads under the heat transfer tests have shown similar buckling behavior. Different turfs having different geometrical shapes (circular and square cross-sectional areas), and different aspect ratios (height/diameter) have buckled in a similar fashion. Figure 5.2 shows three different turfs that buckled under different mechanisms and having different aspect ratios and cross-sectional areas, but sharing similar buckling behavior.

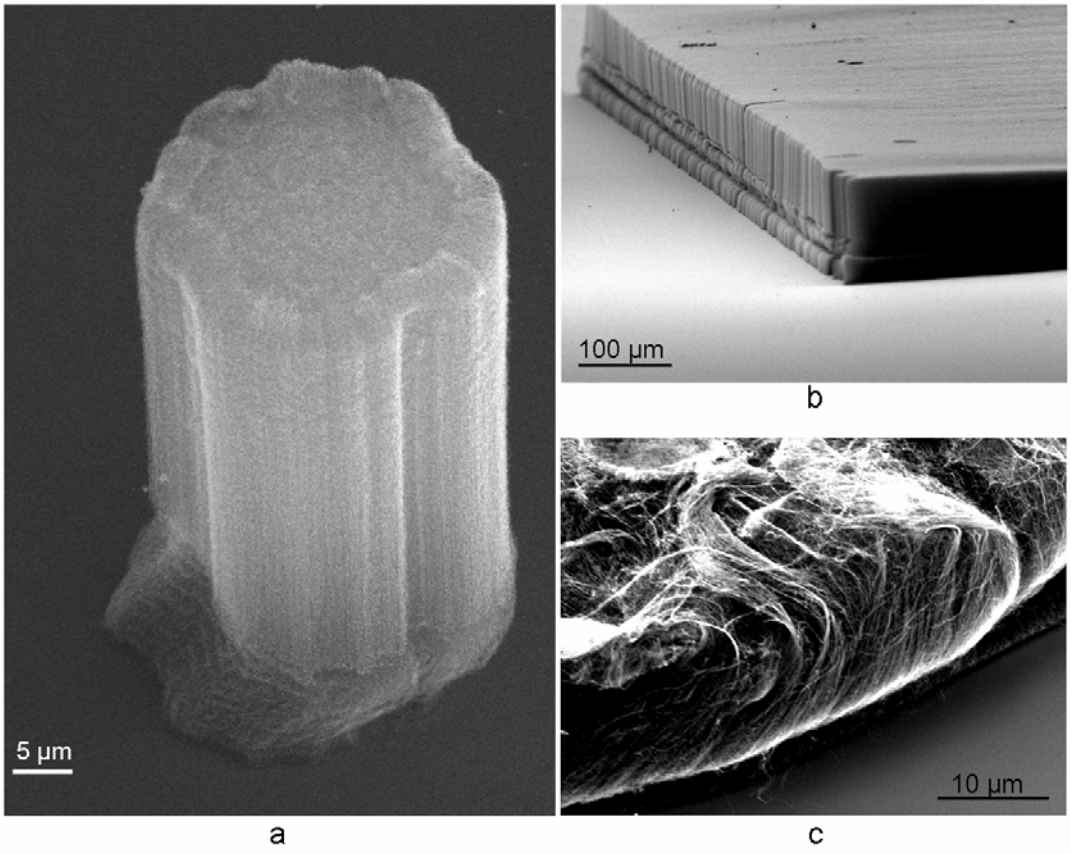

Figure 5.2 SEM images of Buckled turfs. a. A 60 µm high and 30 µm diameter turf buckled using an MTS nanoindenter XPS. **b.** A 4X4 mm turf buckled under applied compressive load during Heat transfer testing. **c.** A 300 µm diameter by 25 µm diameter turf buckled using a standard compression tool.

The buckled turfs shown above all buckled under applied compressive loading by wrinkling in a small segment near the fully constrained bottom. Figure 5.2a and 5.2b illustrated the formation of several buckling wrinkles, while figure 5.3c had only one buckling wrinkle formed as is shown. To further emphasize on the similarities the buckling height, defined as the height between the bottom of the turf and the midpoint of the first buckling wrinkle was measured on four different turfs, and the average was 11.5 µm, with a standard deviation of 3.8 µm.

5.5 Results and Discussion

Although the elastic modulus of a single carbon nanotube can be as high as 1 TPa[20], the collective behavior of CNTs in a turf is instead dominated by buckling/bending of CNT segments, aided by van der Waals bonding between neighboring tubes[21]. The relevant microstructural parameters are: the turf density, the morphology of the individual CNTs and their connectivity within a turf. In order to accurately determine the tangent elastic modulus of CNT turfs, a set of nanoindentation experiments were conducted using a pyramidal diamond tip. Typical load-depth curves generated from these experiments are shown in Figure 5.3. The stiffness of the turf was determined from the initial unloading sequence of each load-depth curve using the conventional method described by Oliver and Pharr. The reduced elastic tangent modulus can be determined from the slope, S and the contact area of the indents[22].

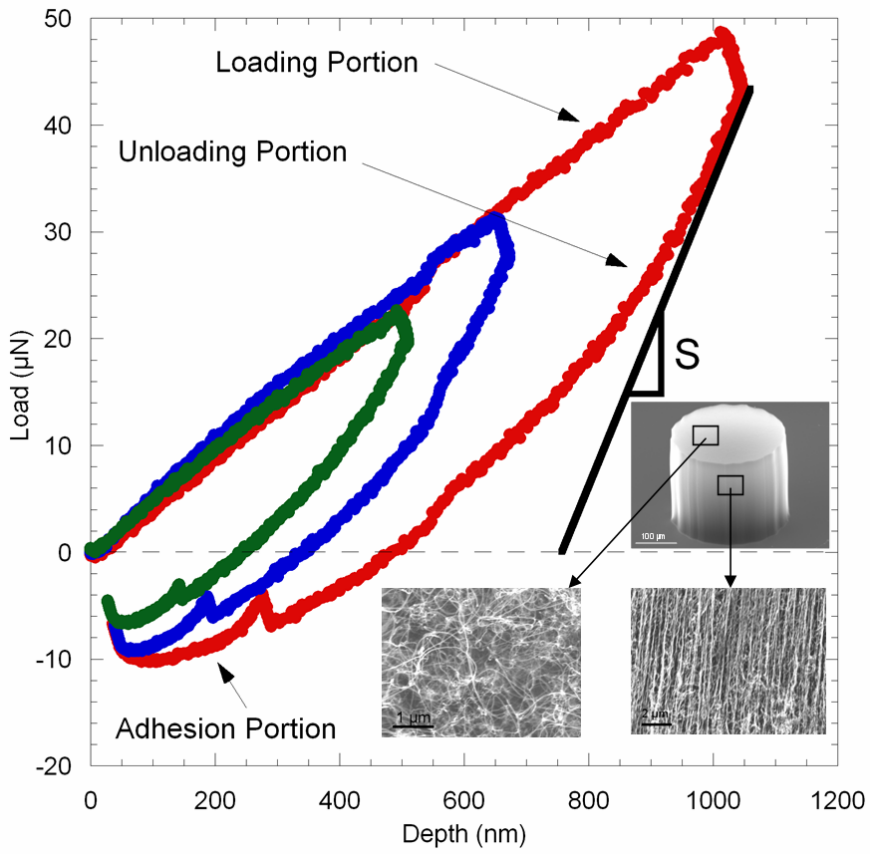

Figure 5.3 Instrumented indentation load-depth curves of CNT turfs. The reduced modulus E_r is calculated using the initial unloading slope of each indent, *S*. These three indents conducted at increasing maximum applied load at different locations in a turf show the typical consistency in the loading portions, and an increasing maximum adhesive load. The SEM pictures show a patterned CNT turf grown by CVD, and a magnified picture of the top surface upon which indentations were performed and its side showing the vertically aligned CNT structure.

As the elastic response of a turf in compression depends on the extent of deformation, an indentation measures a tangent modulus for a given applied strain in the solid; at indentation depths of approximately 1 μm the tangent modulus is effectively

constant in these materials. While Poisson's ratio of a single nanotube is similar to that of graphite, ν=0.19, CNT turfs and due to the collective behavior of carbon nanotubes, have been shown to respond similarly to a foam material23, and therefore a logical choice for Poisson's ratio of the turf is $\nu = 0$[23]. For the series of turfs studied, the average tangent modulus of the CNT turfs, *E*, is 14.9 ±5.7 MPa. It is important to note that there is a measurable adhesive load at the end of the experiment, suggesting significant adhesion occurs between the CNTs and the indenter tip.

In earlier studies and models of continuum approximations of the elastic properties of CNT turfs, it was suggested that the effective elastic tangent modulus of these structures will be dependent on the total applied strain (i.e. they are elastica structures rather than continuum solids). For the purposes of the following experiments the samples will undergo significant strains, and so using the large strain values of the tangent modulus (15 MPa) is appropriate for these materials.

A flat punch indentation was carried out using a MTS Nanoindenter XP on CNT turf bundles with a radius of approximately 30 μm and a height of approximately 60 μm. The load-displacement data collection resulted in the generation of stress-strain curves for each buckled turf (Figure 5.4).

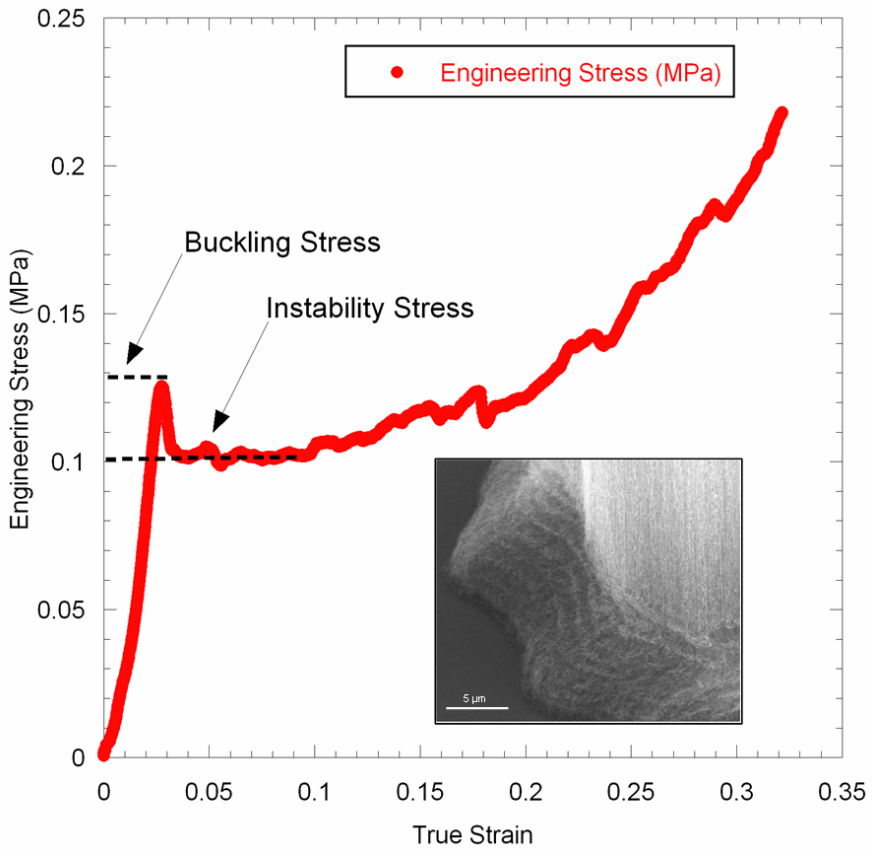

Figure 5.4 Stress-strain curve of a 60 µm high by 30 µm diameter turf under applied compressive loading. The curve reaches a peak followed by a plateau characterizing the formation of the first buckling wrinkle. As the stress on the buckled turf increases several additional wrinkles are formed. The SEM image inset shows wrinkles formed at the bottom of the buckled turf.

Initially the stress increased linearly with respect to strain until a critical buckling stress, at which point the turf deformed as a buckled structure. The plateau following the stress peak of the stress-strain curve is the instability stress of the turf – the smallest stress at which multiple solutions are possible. The difference between the peak stress and the instability stress is the extra stress required to produce coordinated reorientation of segments in a layer of the turf. The small localized stress drops after the initial instability

stress plateau may be result of the formation of other buckling wrinkles, as is shown in the SEM image of the residual turf structure after compression from this specific stress – strain experiment (Figure 5.4).

Observations of the carbon nanotube turfs after an applied compressive load suggested a complicated collective buckling behavior, illustrated schematically in Figure 5.5.

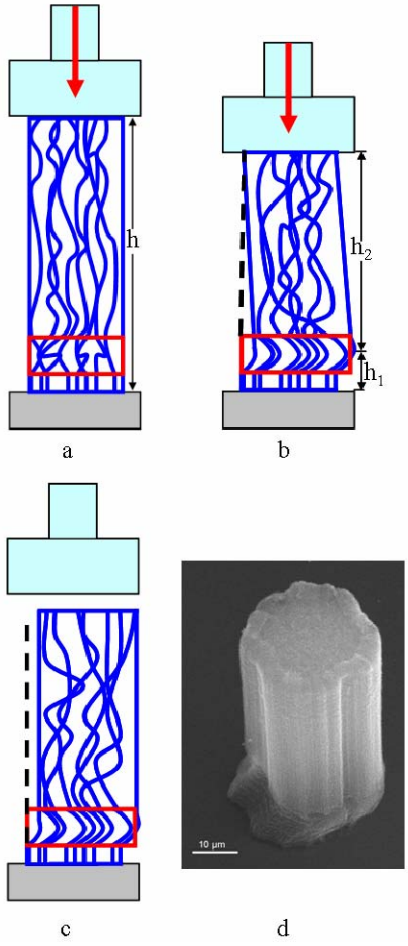

Figure 5.5 Buckling model of a CNT Turf under applied loading with adhesive loads. a. a tip contacts the initially straight turf. **b.** Under applied loading the CNT segments closer to the bottom of the turf reorient laterally. Once the buckling load is reached, the upper portion of the turf shears, while the bottom portion of the turf h_1

buckles in the direction of the initial lateral reorientation. **c.** Once the lateral constraint enforced by the applied load and the tip in contact is removed, the sheared portion will reorient to a vertical alignment. The dotted line illustrates the resulting misalignment due to buckling. **d.** An SEM image of a buckled turf after load removal showing buckling wrinkles and the turf misalignment.

Initially the cylindrical shaped turf consisted of relatively vertically aligned carbon nanotubes. As the applied load is increased, the CNT segments near the fully constrained bottom of the turf uniformly reorient in one lateral direction as shown in Figure 5.5b. Once the critical buckling stress of the turf was reached, the turf buckled in the region of lateral reorientation forming an initial wrinkle and defining the buckling height h_1, while the rest of the turf sheared in the buckling direction to accommodate the lateral constraint at the top of the turf, imposed by the tip in contact as shown in Figure 5.5c, thus forming the shear height h_2. Since the turf is short, the mode of deformation within h_2 is pure shear. As the applied load increased, subsequent buckling wrinkles can be formed. Finally, as the load is removed, adhesive forces between CNT and the tip of a compression fixture pulled the turf and reoriented it straight up with a permanently buckled region showing several wrinkles. This would result in a residual buckled turf with a slight lateral mismatch between the buckling height and the shear height as shown in Figure 5.5d. Electron microscopy of the turf after load removal in Figure 3e reveals the presence of buckling wrinkles and the lateral offset between the top and base of the turf column.

Figure 5.6a shows a schematic model of buckling in the turf. It is reasonable to assume that the turf is fully constrained at the bottom (as the CNTs grow from a sol-gel

glass with embedded iron nanoparticles) The turf is also laterally constrained at the top as a result of the tip-turf contact during a compression test, as the fixtures are significantly stiffer than the turfs. Since *w/h* is not small, the turf segment above the buckling height h_1 of the turf deforms by pure shear. Figure 5.6b is a magnified schematic of the buckling height h_1 emphasizing the buckling shape.

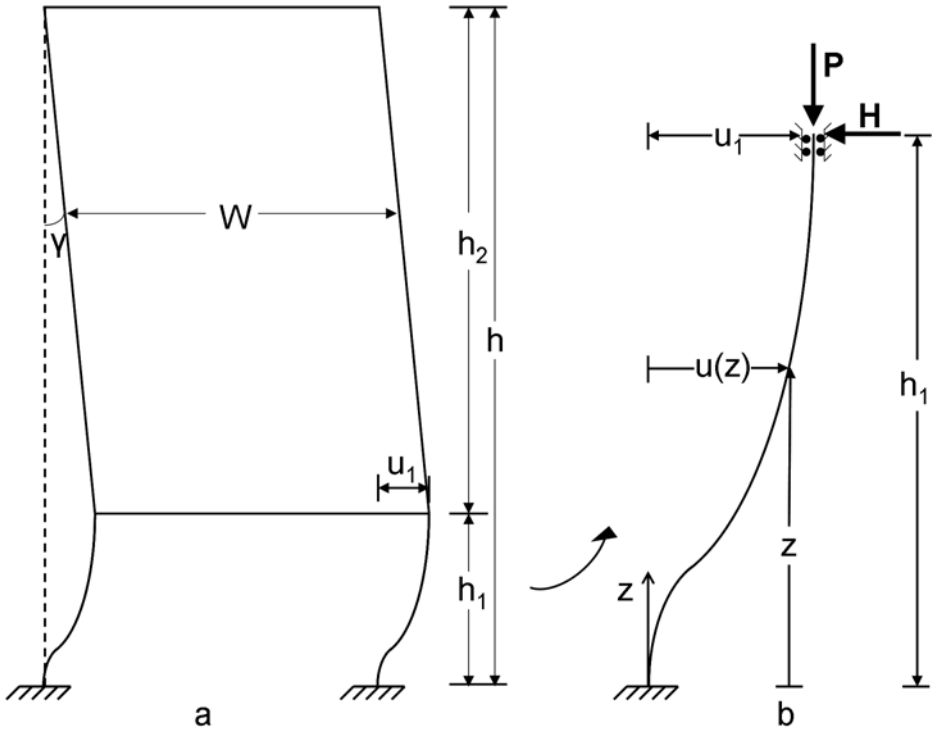

Figure 5.6 A schematic of the buckling model used to predict CNT Turf Buckling. a. The total height of the turf at the instant of buckling *h* is the sum of the buckling height h_1 and the shear height h_2. **b.** A magnified schematic of h_1, showing the applied load *P* as well as the shear load *H* at the buckling state or the maximum lateral displacement u_1.

The instability stress shown in Figure 5.4 is the lowest compressive stress at which multiple solutions are possible. The coordinated buckling depicted in Figures 5.4 and 5.6 requires – in addition to multiple solutions – a coordinated reorientation of

segments in the buckling region. Therefore, the actual buckling takes place at a somewhat higher stress – the peak in Figure 5.4.

The shape of a buckled CNT segment is given by the Euler differential equation:

$$\mathrm{P}(u_1 - u) - H(h_1 - z) = E_t I \frac{d^2 u}{dz^2} \qquad (1)$$

where the load carried by the tubes,

$$\mathrm{P} = \frac{\sigma}{N} \qquad (2)$$

is determined from the nominal normal applied stress σ, and the number of CNTs per unit area of the horizontal section, N. Here N will account for both carbon nanotube density per unit area and morphology of the CNTs (i.e. they are not aligned vertically). The lateral force, H,

$$H = \frac{\mu u_1}{h_2 N}, \qquad (3)$$

depends on the effective shear modulus of the upper part of the turf, μ, the maximum lateral displacement u_1, and N. E_t is the elastic modulus of a single tube, and I is the area moment of inertia of the turf's cross-sectional area. For ν=0, μ=E/2.

Rearranging equation 1, while substituting the equivalents of P and H from equations 2 and 3, results in the following differential equation:

$$u'' + \omega^2 u = \mathrm{A}z + \mathrm{B} \qquad (4)$$

Where:

$$\omega^2 = \frac{\sigma}{\mathrm{NE}_t\mathrm{I}}, \ \mathrm{A} = \frac{\mu u_1}{h_2 \mathrm{NE}_t \mathrm{I}} \text{ and } \mathrm{B} = \omega^2 u_1 - \mathrm{A}h_1$$

Solving the differential equation by employing the rigid boundary conditions at the bottom of the turf u(0)=0 and u'(0)=0 results in the following solution:

$$u = -\frac{\mathrm{B}}{\omega^2}\cos(\omega z) - \frac{\mathrm{A}}{\omega^3}\sin(\omega z) + \frac{\mathrm{A}z + \mathrm{B}}{\omega^2} \qquad (5)$$

This yields to a solution of σ as a function of u_1. Then, the minimum value of σ which corresponds to a non-trivial solution ($u_1(h_1)\neq 0$) is given by

$$\beta = \frac{1-\alpha}{\alpha} \qquad (6)$$

Where:

$$\beta = \frac{\mu}{\sigma} \text{ and } \alpha = \frac{h_1}{h} \qquad (7)$$

Thus:

$$\frac{\mu}{\sigma} = \frac{1 - h_1/h}{h_1/h}. \qquad (8)$$

This is the instability stress shown in Figure 5.4. Therefore, the result is directly dependant on the shear modulus of the turf as well as the initial turf height *h,* and the final buckling height h_1. Assuming that the tangent modulus measured during indentation is sufficient to estimate the parameter *N* that relates the properties of a single tube to the assemblage properties, (i.e. an increased density or increased vertical alignment would result in a different tangent elastic modulus), the critical stress would also be indirectly dependent upon the shear strain $\gamma = u_1/h_2$. The buckling height h_1, was measured on four different buckled turfs with varying heights and diameters between 30 and 300 μm, and found to be relatively constant; approximately 11.5 ± 3.8μm.

To examine the validity of equation 9, CNT turfs were tested in compression with a spherical steel tip with a radius of approximately 1.6 mm using a basic compression test

rig as described in Chapter 2. Several turfs with a diameter of 300 μm and various heights were tested under compression and the respective stress-strain curves were used to determine the critical buckling stress for each turf. Since buckling stresses would be dependent on the turf elastic modulus, the results were generalized by dividing the critical buckling stresses by the average modulus of elasticity determined using nanoindentation. The experimentally determined σ/E are shown as a function of initial turf height, h, in Figure 5.7. It is important to note that the aspect ratio is not the controlling factor in these experiments, as h_1 is similar between turfs with a height to diameter ratio ranging from 2 to 0.1.

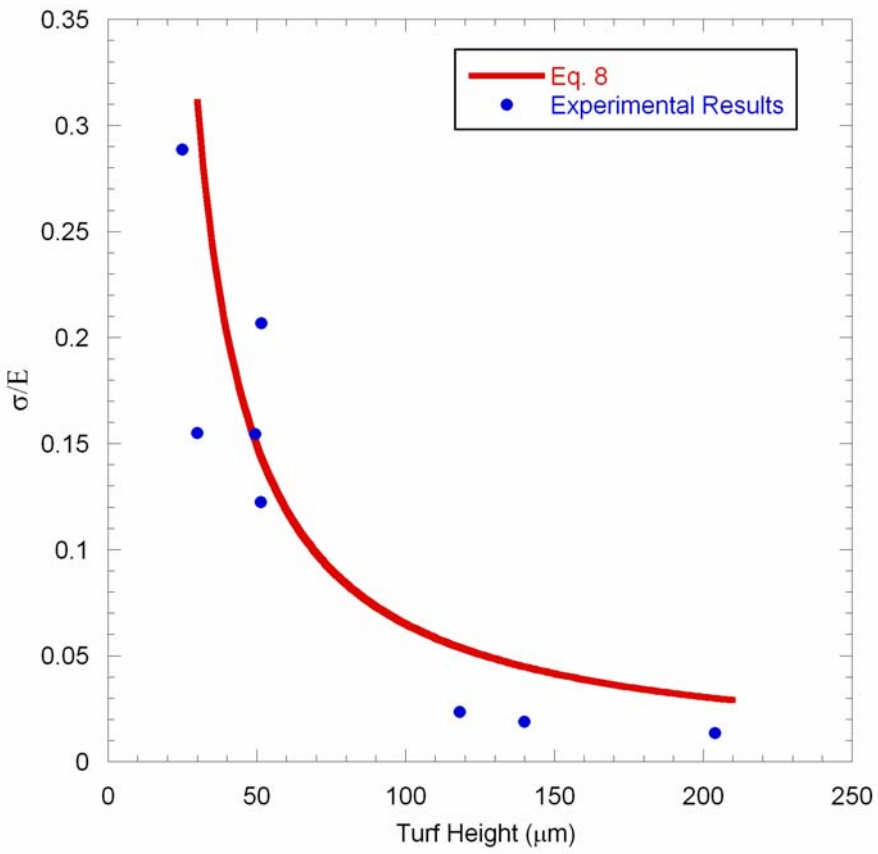

Figure 5.7 Variation of *σ/E* as a function of Turf Height. Experimentally measured buckling stresses normalized by the effective elastic modulus of the buckled turfs for a variety of turf heights and aspect ratios, with the model prediction of equation 9 shown.

Finally it is necessary to note that although the model presented is a first order model, it seems to predict the results in a rather high accuracy. This interesting correlation between the model and the experimental results that were used to validate it is astonishing although several factors could have affected the results and are worth mentioning: the engineering assumptions that were used in the model, and the possible experimental errors. Experimental errors include possible misalignment between the compression tip and the turf while testing, although a spherical tip was used to attenuate

the effect of this error, and also impurities and variation in the densities of the turfs due to growth variations.

5.6 Conclusion

CNT turfs exhibit local, coordinated buckling under a monotonic compressive load. CNT turfs with heights varying between 25 and 200 μm were tested in compression. These turfs buckle under applied monotonic loading at nominal stresses ranging between 4.3 and 0.2 MPa. The buckling stress depends on the tangent modulus and the height (but surprisingly not on the aspect ratio) of the CNT turf. The buckling stresses ranged between 0.3 and 0.01 of the shear modulus of the turf. A simple mathematical model was used to predict the critical buckling stress was developed and its results reasonably predict the critical buckling stresses. These observations and results are expected to impact designs where the collective mechanical behavior of CNT turfs is as important as the mechanical behavior of a single tube.

5.7 References

[1] Iijima, S. Helical microtubules of graphitic carbon. *Nature* **354,** 56-58 (1991).
[2] Iijima, S., & Ichihashi, T. Single-shell carbon nanotubes of 1nm diameter. *Nature* **363,** 603-605 (1993).
[3] Bethune, D. S., Klang, C. H., De Vries, M. S., Gorman, G., Savoy, R., Vasquez, J. & Beyers, R. Cobalt-catalysed growth of carbon nanotubes with single-atomic-layer walls. *Nature* **363,** 605-607 (1993).
[4] Baughman, R. H., Zakhidov, A. A. & de Heer, W. A. Carbon nanotubes-the route toward applications. *Science* **297,** 787-792 (2002).
[5] Ball, P. Roll up for the revolution. *Nature* **414,** 142-144 (2001).
[6] Yu, M. F., Lourie, Dyer, M. J., Moloni, K., Kelly, T. F. & Ruoff, R. S. Strength and breaking mechanism of multiwalled carbon nanotubes under tensile loads. *Science* **287,** 637-640 (2000).

[7] Park, B. C., Jung, K. Y., Song, W. Y., O, B. & Ahn, S. J. Bending of a carbon nanotube in vacuum using a focused ion beam. *Advanced Materials* **18,** 95-98 (2006)
[8] Tombler T. W., Binh, V. T., Guillot, D., Teo, K.B.K., Chhowalla, M., Amaratunga, G.A.J., Milne, W.I., Legagneux, P. & Pribat, D. Reversible electromechanical characteristics of carbon nanotubes under local-probe manipulation. *Nature* **405,** 769-772 (2000)
[9] Waters, J. F., Riester, L., Jouzi, M., Guduru, P. R. & Xu, J. M. Buckling instabilities in multiwalled carbon nanotubes under uniaxial compression. *Appl. Phys. Letters* **85,** 1787-1789 (2004)
[10] Liew, K. M., Wong, C. H. and Tan, M. J. Buckling properties of carbon nanotube bundles *Appl. Phys. Lett.* **87,** 041901-1-3 (2005).
[11] Pantano, A., Boyce, M. C. & Parks, D. M. Nonlinear structural mechanics based modeling of carbon nanotube deformation. *Phys. Rev. Lett.* **91,** 145504-1-4 (2003).
[12] Qi, H. J., Teo, K.B.K., Lau, K.K.S., Boyce, M.C., Milne, W.I., Robertson, J. & Gleason, K.K. Determination of mechanical properties of carbon nanotubes and vertically aligned carbon nanotube forests using nanoindentation. *J. of Mech. & Phys. of Sol.* **51,** 2213-2237 (2003).
[13] Terrones, M., Grobert, N., Olivares, J., Zhang J. P., Terrones, H., Kordatos, K., Hsu, W. K., Hare, J. P., Townsend, P. D., Prassides, K., Cheetham, A. K., Kroto, H. W. & Walton, D. R. M. Controlled production of aligned-nanotube bundles. *Nature* **388,** 52-55 (1997).
[14] Fan, Sh., Chapline, M. G., Franklin, N. R., Tombler, T. W., Cassell, A. M. & Dai, H. Self-oriented regular arrays of carbon nanotubes and their field emission properties *Science* **283**, 512-514 (1999);
[15] Cao, A. Dickrell, P. L., Sawyer, W. G., Ghasemi-Nejhad, M. N. & Ajayan, P. M. Super-compressible foamlike carbon nanotube films. *Science* **310,** 1307-1310 (2005).
[16] McCarter C. M. Bahr, D.F., Richards, R.F., Ricahrds, C.D., McClain, D. & Jiao, J. Mechanical compliance of photolithographically defined vertically aligned carbon nanotube turf. *J. Mater. Sci.* **41,** 7872-7878 (2006)
[17] Mesarovic, S. Dj., McCarter, C. M., Bahr, D. F., Radhakrishnan, H., Richards, R. F., Richards, C. D., McClain, D. & Jiao, J. Mechanical behavior of a carbon nanotube turf *Scripta Materialia* **56,** 157-160 (2007).
[18] Xu, J. & Fisher, T.S., Enhancement of thermal interface materials with carbon nanotube arrays, *Int. J. Heat Mass Transfer*, **49**, 1658-1666 (2006).
[19] Dong, L., Jiao, J., Pan C. and Tuggle, D. W. Effects of catalysts on the internal structures of carbon nanotubes and corresponding electron field-emission properties. *Appl. Phys. A* **78,** 9-14 (2004)
[20] Treacy, M. M. J., Ebbesen, T. W. & Gibson, J. M. Exceptionally high Young's modulus observed for individual carbon nanotubes. *Nature* **381,** 678-680 (1996)
[21] Kis, A., Csanyi, G., Salvetat, J.-P., Lee, T-N., Couteau, E., Kulik, A.J., Benoit, W., Brugger, J. & Forro, L. Reinforcement of single-walled carbon nanotube bundles by intertube bridging. *Nature* **3,** 153-157 (2004).
[22] Oliver, W. C. & Pharr G. M. An Improved technique for determining hardness and elastic modulus using load and displacement sensing indentation experiments. *J. Mater. Res.* **7,** 1564-1583 (1992).

[23] Deshpande V. S. and Fleck, N. A., Isotropic Constitutive Models for Metallic Foams, J. Mech. Phys. Solids. 48, 1253 (2000).

CHAPTER SIX

6 CONCLUSION AND RECOMMENDATIONS FOR FUTURE WORK

This thesis has enhanced the existing experimental apparatus for extracting the mechanical properties of carbon nanotube turfs. Frequent tip cleaning was shown to be necessary, as CNTs stuck on the diamond tip have interacted with the turf during subsequent indents, which dramatically reduced the unloading slope of the load-depth curves, thus the measurements of the turf's elastic properties, nominally elastic modulus and hardness. Indents had to be conducted at unloading rates higher than 180 μN/sec as the instantaneous adhesive forces tend to drag the tip downward and thus increase the unloading slope at low unloading rates, which resulted in higher elastic properties measurements. The turf elastic modulus was estimated to be 14.9 MPa with a standard deviation of 5.8 MPa. The hardness of the turf was on the order of 5.5 MPa.

The thesis also studied the mechanical behavior of a turf under nanoindentation, in which case only a fraction of the surface of the turf was in contact with the indentation tip. The effect of intertube van der Waals bonding and their effect on mechanical behavior were studied. A model explaining the onset of plastic deformation in turf like materials, in terms of a locking mechanism has been suggested. The experimental results seemed to support the idea that the locking mechanism which occurred at a critical stress was a combination of a mechanical locking resulting from an increase in the entanglement of CNT segments under applied compressive loading, but also a chemical locking as a result of van der Waals bonding. Adhesion between CNT tubes and carbon based tips has been quantified using nanoindentation, and has been shown to be dependent upon the tip's geometry and the applied stress. Adhesion forces resulting from

elastic spherical indents agreed with the JKR pull-off load predictions. Hardness of the turf was reduced upon coating it with gold, and calculated to be on the order of 2 MPa. A possible model suggesting that gold coating the turf minimizes the effect of van der Waals, which although easily breakable seemed to highly affect the turf's hardness, was proposed. This explanation was reinforced by SEM observations of the coated turf.

Localized buckling near the rigid boundary of the turf has been experimentally observed under applied compressive loading. A phenomenological model was proposed and developed which allowed the prediction of the critical buckling stress given the turf's height and elastic properties. A set of turfs with heights ranging from 25 to 200 μm were tested in compression, and the results were in agreement with the developed model. A model explaining the unidirectional, self coordinating and reorientation of a set of CNT segments at a localized region once the critical buckling was reached has been proposed.

Finally it is recommended that any future work involving further study of the mechanical behavior of CNT turfs performs the following tasks. Once an in situ compressive loading apparatus that would fit in an SEM becomes available, it would be necessary to observe a turf buckling under applied compressive loading to better understand the self orientation mechanism of CNT segments closer to the fully constrained turf prior to buckling, and validate the model developed within the scope of this thesis. Also developing a way to measure CNT density in any given turf as well as the segments' tortuoasities prior to mechanical testing would be beneficial as it will help understand the effect these two parameters have on the turf's mechanical behavior and buckling.

APPENDICES

Appendix 1: Description of the mechanical / mathematical model developed to predict CNT turfs buckling

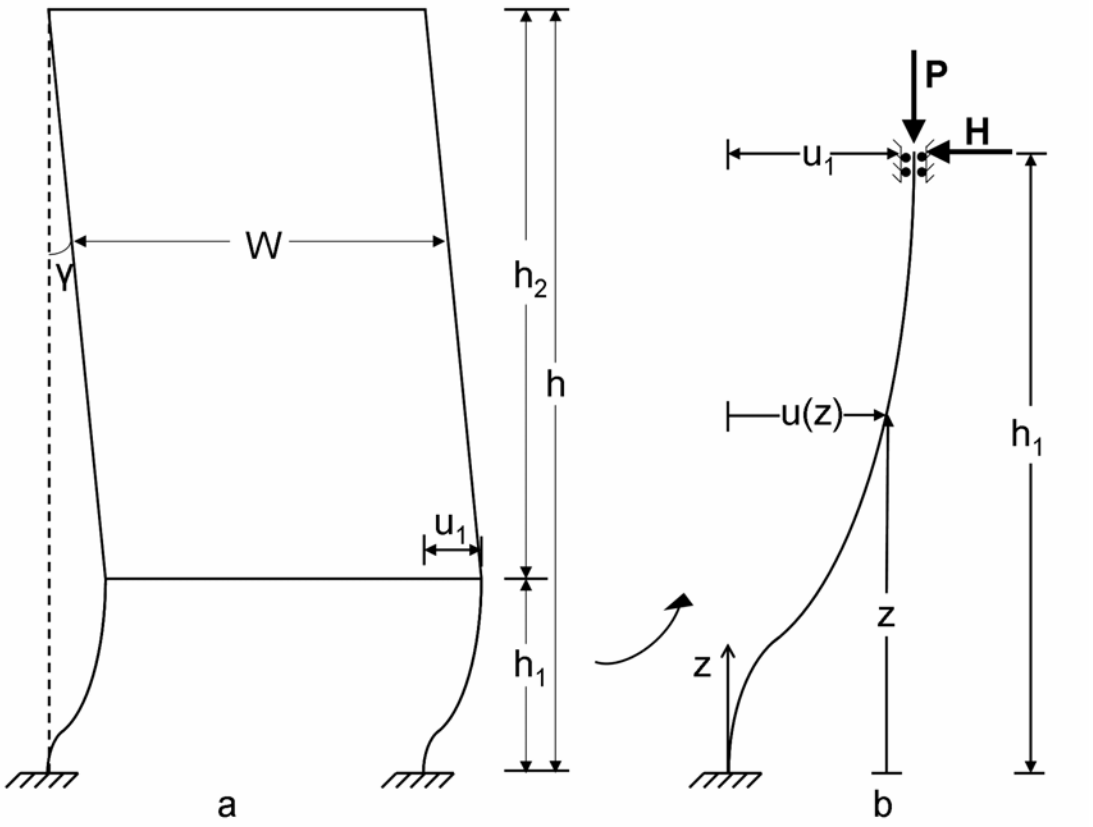

Define the following variables:
N= CNT per unit area [$1/m^2$]
u= lateral turf displacement [m]
u_1= lateral turf displacement
h= turf height [m]
h_1= buckling height of the turf defined from the fixed boundary to the center of the buckled zone [m]
h_2= sheared portion of the turf, defined as $h-h_1$ [m]
σ= Applied compressive stress [Pa]
P= Applied compressive loading [N]
u= u(z) = lateral displacement of the turf along the z axis shown above [m]
u_1= $u(h_1)$= Maximum lateral displacement of the turf, occurring at h_1 upon buckling [m]
γ= Shear strain of the sheared portion of the turf
H= shear resultant [N]
μ=effective shear modulus of the turf [N/m^2]

E_t= Elastic modulus of a single tube [Pa]
I= Area moment of inertia for the turf's cross-sectional area [m^4]

The shape of a buckled CNT segment may be given by developing the Euler differential equation as follows:

$$\sum \mathrm{M} = \mathrm{E}_t \mathrm{I} u''$$

Where M is a moment about any given point on the segment, and u" is the curvature at this point.

$$\Rightarrow \mathrm{P}(u_1 - u) - \mathrm{H}(h_1 - z) = \mathrm{E}_t \mathrm{I} u''$$

$$\Rightarrow u'' = \frac{\mathrm{P}}{\mathrm{E}_t \mathrm{I}} u_1 - \frac{\mathrm{P}}{\mathrm{E}_t \mathrm{I}} u - \frac{\mathrm{H}}{\mathrm{E}_t \mathrm{I}} h_1 + \frac{\mathrm{H}}{\mathrm{E}_t \mathrm{I}} z$$

However the applied load P can be expressed as the applied stress divided by the tube density:

$$\mathrm{P} = \frac{\sigma}{N}$$

And the shear effect can be determined as follows:

$$\gamma = \frac{\mathrm{NH}}{\mu}$$

and

$$\gamma = \frac{u_1}{h_2}$$

$$\Rightarrow \mathrm{H} = \frac{\mu u_1}{h_2 N}$$

And the differential equation becomes:

$$u'' = \frac{\sigma u_1}{\mathrm{NE}_t \mathrm{I}} - \frac{\sigma}{\mathrm{NE}_t \mathrm{I}} u - \frac{\mu u_1}{h_2 \mathrm{NE}_t \mathrm{I}} h_1 + \frac{\mu u_1}{h_2 \mathrm{NE}_t \mathrm{I}} h_1 + \frac{\mu u_1}{h_2 \mathrm{NE}_t \mathrm{I}} z$$

$$\Rightarrow u'' + \frac{\sigma}{\mathrm{NE}_t \mathrm{I}} u = \frac{\mu u_1}{h_2 \mathrm{NE}_t \mathrm{I}} z + \left(\frac{\sigma}{\mathrm{NE}_t \mathrm{I}} u_1 - \frac{\mu u_1}{h_2 \mathrm{NE}_t \mathrm{I}} h_1 \right)$$

Defining the following terms:

$$\omega^2 = \frac{\sigma}{\mathrm{NE}_t \mathrm{I}}$$

$$\mathrm{A} = \frac{\mu u_1}{h_2 \mathrm{NE}_t \mathrm{I}}$$

$$\mathrm{B} = \omega^2 u_1 - \mathrm{A} h_1$$

Results in the following simplified differential equation:

$$u'' + \omega^2 u = \mathrm{A}z + \mathrm{B}$$

This is a second order differential equation which is solved by finding a homogeneous and particular solution for it and taking their linear combination:

Homogeneous solution:

$$u'' + \omega^2 u = 0$$

$$u = e^{rz} \Rightarrow u' = re^{rz} \Rightarrow u'' = r^2 e^{rz}$$

This leads to the following characteristic equation:

$$r^2 + \omega^2 = 0 \Rightarrow r = \pm i\omega$$

$$\Rightarrow u^h = c_1 \cos \omega z + c_2 \sin \omega z$$

Where u^h is the homogeneous solution and c_1 and c_2 are constants to be determined.

Particular solution:

Assume the following particular solution

$$u^p = c_3 z^2 + c_4 z + c_5$$

$$\Rightarrow u^{p'} = 2c_3 z + c_4$$

$$\Rightarrow u^{p''} = 2c_3$$

Which implies

$$2c_3 + \omega^2 c_3 z^2 + \omega^2 c_4 z + \omega^2 c_5 = \mathrm{A}z + \mathrm{B}$$

$$\Rightarrow c_3 = 0$$

$$\Rightarrow c_4 = \frac{\mathrm{A}}{\omega^2} = \frac{\mu u_1}{h_2 \sigma}$$

$$\Rightarrow c_5 = \frac{\mathrm{B}}{\omega^2} = u_1 - \frac{\mu u_1}{h_2 \sigma} h_1$$

Therefore the solution u would be:

$$u = c_1 \cos \omega z + c_2 \sin \omega z + \frac{\mu u_1}{h_2 \sigma} z + u_1 - \frac{\mu u_1}{h_2 \sigma} h_1$$

To calculate c_1 and c_2, we employ the following boundary conditions:

$$u(0) = 0$$

$$u'(0) = 0$$

$$\Rightarrow u(0) = c_1 + u_1 - \frac{\mu u_1}{h_2 \sigma} h_1 = 0$$

$$\Rightarrow c_1 = \frac{\mu u_1}{h_2 \sigma} h_1 - u_1$$

On the other hand we derive u to get

$$u' = -c_1\omega\sin\omega z + c_2\omega\cos\omega z + \frac{\mu u_1}{h_2\sigma}$$

$$\Rightarrow u'(0) = c_2\omega + \frac{\mu u_1}{h_2\sigma} = 0$$

$$\Rightarrow c_2 = -\frac{\mu u_1}{h_2\sigma\omega}$$

The lateral displacement u can therefore be described as follows:

$$u(z) = \left[\frac{\mu u_1}{h_2\sigma}h_1 - u_1\right]\cos\omega z - \frac{\mu u_1}{h_2\sigma\omega}\sin\omega z + \frac{\mu u_1}{h_2\sigma}z + u_1 - \frac{\mu u_1}{h_2\sigma}h_1$$

where

$$\omega = \sqrt{\frac{\sigma}{\mathrm{NE}_t\mathrm{I}}}$$

Deriving u with respect to z results in

$$u'(z) = -\left[\frac{\mu u_1}{h_2\sigma}h_1 - u_1\right]\omega\sin\omega z - \frac{\mu u_1}{h_2\sigma\omega}\omega\cos\omega z + \frac{\mu u_1}{h_2\sigma}$$

Using the boundary conditions at the buckling height h_1:

$$\begin{cases} u(h_1) = u_1 \\ u'(h_1) = 0 \end{cases}$$

Results in the following set of equation:

$$\begin{cases} \left[\frac{\mu u_1}{h_2\sigma}h_1 - u_1\right]\cos\omega h_1 - \frac{\mu u_1}{h_2\sigma\omega}\sin\omega h_1 + u_1 = u_1 \\ -\left[\frac{\mu u_1}{h_2\sigma}h_1 - u_1\right]\omega\sin\omega h_1 - \frac{\mu u_1}{h_2\sigma}\cos\omega h_1 + \frac{\mu u_1}{h_2\sigma} = 0 \end{cases}$$

Define α as

$$\alpha = \frac{h_1}{h} \Rightarrow h_1 = \alpha h$$

$$\Rightarrow h_2 = h - h_1 = (1-\alpha)h$$

Thus the set becomes:

$$\begin{cases} \left[\frac{\mu u_1}{(1-\alpha)h\sigma}\alpha h - u_1\right]\cos(\omega\alpha h) - \frac{\mu u_1}{(1-\alpha)h\sigma\omega}\sin(\omega\alpha h) = 0 \\ -\left[\frac{\mu u_1}{(1-\alpha)h\sigma}\alpha h - u_1\right]\omega\sin(\omega\alpha h) - \frac{\mu u_1}{(1-\alpha)h\sigma}\cos(\omega\alpha h) + \frac{\mu u_1}{(1-\alpha)h\sigma} = 0 \end{cases}$$

Define $\overline{\omega}$ and β as

$$\overline{\omega} = \omega h$$

and

$$\beta = \frac{\mu}{\sigma}$$

The set of equation becomes:

$$\begin{cases} \left(\frac{\beta}{(1-\alpha)}\alpha - 1\right)\cos\overline{\omega}\alpha - \frac{\beta}{(1-\alpha)\overline{\omega}}\sin\overline{\omega}\alpha = 0 \\ -\left(\frac{\beta}{(1-\alpha)}\alpha - 1\right)\omega\sin\overline{\omega}\alpha - \frac{\beta}{(1-\alpha)h}\cos\overline{\omega}\alpha + \frac{\beta}{(1-\alpha)h} = 0 \end{cases}$$

$$\Rightarrow$$

$$\begin{cases} \left(\frac{\beta}{(1-\alpha)}\alpha - 1\right)\cos\overline{\omega}\alpha - \frac{\beta}{(1-\alpha)\overline{\omega}}\sin\overline{\omega}\alpha = 0 \\ \left(\frac{\beta}{(1-\alpha)}\alpha - 1\right)\sin\overline{\omega}\alpha + \frac{\beta}{(1-\alpha)\overline{\omega}}\cos\overline{\omega}\alpha = \frac{\beta}{(1-\alpha)\overline{\omega}} \end{cases}$$

Define l as and ϕ as follows

$$l = \sqrt{\left(\frac{\beta}{(1-\alpha)}\alpha - 1\right)^2 + \left(\frac{\beta}{(1-\alpha)\overline{\omega}}\right)^2} = \frac{1}{1-\alpha}\sqrt{(\alpha\beta + \alpha - 1)^2 + \left(\frac{\beta}{\overline{\omega}}\right)^2}$$

Such that

$$\frac{\left(\frac{\beta}{(1-\alpha)}\alpha - 1\right)}{l} = \cos\overline{\omega}\phi$$

and

$$\frac{\frac{\beta}{(1-\alpha)\overline{\omega}}}{l} = \sin\overline{\omega}\phi$$

The set becomes:

$$\begin{cases} \cos(\overline{\omega}\varphi)\cos(\overline{\omega}\alpha) - \sin(\overline{\omega}\varphi)\sin(\overline{\omega}\alpha) = 0 \\ \cos(\overline{\omega}\varphi)\sin(\overline{\omega}\alpha) + \sin(\overline{\omega}\varphi)\cos(\overline{\omega}\alpha) = \frac{\frac{\beta}{(1-\alpha)\overline{\omega}}}{l} \end{cases}$$

Using trigonometric relations:

$$\begin{cases} \cos\ \overline{\omega}(\phi + \alpha) = 0 \\ \sin\ \overline{\omega}(\phi + \alpha) = \frac{\frac{\beta}{(1-\alpha)\overline{\omega}}}{l} = \sin\ \overline{\omega}\alpha \end{cases}$$

Square and add the equations:

$$1 = \frac{\frac{\beta^2}{(1-\alpha)^2 \overline{\omega}^2}}{l^2}$$

$$\Rightarrow \frac{\beta^2}{(1-\alpha)^2 \overline{\omega}^2} = \frac{1}{(1-\alpha)^2}\left[(\alpha\beta + \alpha - 1)^2 + \left(\frac{\beta}{\overline{\omega}}\right)^2\right]$$

$$\Rightarrow (\alpha\beta + \alpha - 1)^2 = 0$$

$$\Rightarrow \alpha^2\beta^2 + \alpha^2 + 1 + 2\alpha^2\beta - 2\alpha\beta - 2\alpha = 0$$

$$\Rightarrow \alpha^2\beta^2 + (2\alpha^2 - 2\alpha)\beta + (\alpha^2 - 2\alpha + 1) = 0$$

$$\Delta = [(2\alpha^2 - 2\alpha)]^2 - 4\alpha^2(\alpha^2 - 2\alpha + 1)$$

$$\Rightarrow \Delta = 0$$

thus

$$\beta = \frac{-2\alpha(\alpha - 1)}{2\alpha^2} = \frac{-(\alpha - 1)}{\alpha}$$

Replacing β and α by their values results in:

$$\frac{\mu}{\sigma} = \frac{\left(1 - \frac{h_1}{h}\right)}{\frac{h_1}{h}}$$

Which simplifies to

$$\sigma = \frac{\mu h_1}{h - h_1}$$